

REVIEW

Materials, photophysics and device engineering of perovskite light-emitting diodes

To cite this article: Ziming Chen *et al* 2021 *Rep. Prog. Phys.* **84** 046401

View the [article online](#) for updates and enhancements.

You may also like

- [Multifractal analysis of financial markets: a review](#)

Zhi-Qiang Jiang, Wen-Jie Xie, Wei-Xing Zhou et al.

- [The spin structure of the nucleon](#)

Alexandre Deur, Stanley J Brodsky and Guy F de Téramond

- [The matrix environmental and cell mechanical properties regulate cell migration and contribute to the invasive phenotype of cancer cells](#)

Claudia Tanja Mierke



IOP | ebooks™

Bringing together innovative digital publishing with leading authors from the global scientific community.

Start exploring the collection—download the first chapter of every title for free.

Review

Materials, photophysics and device engineering of perovskite light-emitting diodes

Ziming Chen^{1,2,7} , Zhenchao Li^{1,7}, Thomas R Hopper^{3,7} , Artem A Bakulin^{3,*}  and Hin-Lap Yip^{1,4,5,6,*} 

¹ State Key Laboratory of Luminescent Materials and Devices, Institute of Polymer Optoelectronic Materials and Devices, School of Materials Science and Engineering, South China University of Technology, 381 Wushan Road, Guangzhou 510640, People's Republic of China

² School of Environment and Energy, South China University of Technology, Guangzhou University City, Panyu District, Guangzhou 510006, People's Republic of China

³ Department of Chemistry and Centre for Processable Electronics, Imperial College London, London W12 0BZ, United Kingdom

⁴ Innovation Center of Printed Photovoltaics, South China Institute of Collaborative Innovation, Dongguan 523808, People's Republic of China

⁵ Department of Materials Science and Engineering, City University of Hong Kong, Tat Chee Avenue, Kowloon, Hong Kong Special Administrative Region of China

⁶ School of Energy and Environment, City University of Hong Kong, Tat Chee Avenue, Kowloon, Hong Kong Special Administrative Region of China

E-mail: a.bakulin@imperial.ac.uk and msangusyip@scut.edu.cn

Received 31 October 2020, revised 15 February 2021

Accepted for publication 17 March 2021

Published 12 April 2021



Abstract

Here we provide a comprehensive review of a newly developed lighting technology based on metal halide perovskites (i.e. perovskite light-emitting diodes) encompassing the research endeavours into materials, photophysics and device engineering. At the outset we survey the basic perovskite structures and their various dimensions (namely three-, two- and zero-dimensional perovskites), and demonstrate how the compositional engineering of these structures affects the perovskite light-emitting properties. Next, we turn to the physics underpinning photo- and electroluminescence in these materials through their connection to the fundamental excited states, energy/charge transport processes and radiative and non-radiative decay mechanisms. In the remainder of the review, we focus on the engineering of perovskite light-emitting diodes, including the history of their development as well as an extensive analysis of contemporary strategies for boosting device performance. Key concepts include balancing the electron/hole injection, suppression of parasitic carrier losses, improvement of the photoluminescence quantum yield and enhancement of the light extraction. Overall, this review reflects the current paradigm for perovskite lighting, and is intended to serve as a foundation to materials and device scientists newly working in this field.

* Authors to whom any correspondence should be addressed.

⁷ These authors contributed equally to this work.

Corresponding editor: Professor Dr Tao Wang.

Keywords: perovskites, light-emitting diodes, photophysics, device engineering, materials

(Some figures may appear in colour only in the online journal)

Introduction

Based on the excellent optoelectronic and lighting properties of metal halide perovskite (MHP) materials, perovskite light-emitting diodes (PeLEDs) have great potential to be the foremost next-generation light-emitting diode (LED). Since 2014, substantial progress has been made in the PeLED field, and it is important to summarise these works from a fundamental angle in order to reach a better understanding of perovskite emitters. In this review, we will discuss the basic physics of perovskite lighting from three main aspects of ‘materials’, ‘photophysics’ and ‘device engineering’ to consolidate a conceptual framework for the further development of PeLEDs.

In the ‘materials’ section, we will focus on the dimensional and compositional engineering of the MHP family. Regarding dimensional engineering, we will discuss the crystallography of three-dimensional (3D) bulk perovskites, two-dimensional (2D)/quasi-2D perovskites and zero-dimensional (0D) perovskite quantum dots (QDs)/nanocrystals (NCs), which have all been widely studied in terms of their lighting applications. The formation of these three types of perovskite structure will also be presented. Regarding compositional engineering, we will discuss how the modulation of the A-site cation, B-site cation, and X-site anion that make up the aforementioned structures affect the energy levels and bandgaps of perovskites, which in turn control the charge injection and emission colour in PeLEDs. The combination of dimensional and compositional engineering has already yielded a myriad of perovskite emitters for LED applications.

In the ‘photophysics’ section, we elucidate the fundamental physics of the excited states relevant to perovskite lighting. Beginning with a rudimentary description of the electronic structure, we discuss the apparent direct–indirect nature of the perovskite bandgap, the electronic excitations that occur therein, and the interaction of these excitations with the perovskite lattice via carrier–phonon coupling. Secondly, we describe how these excitations move within and between grains (of various dimensions) through energy and carrier transport mechanisms. Thirdly, we distinguish between the carrier and exciton recombination processes in the bulk (3D) perovskites and their low-dimensional (2D and 0D) counterparts that give rise to radiative and non-radiative decay. Lastly, we point towards some special cases where more exotic photoluminescence (PL) behaviours have been exploited to enable high-performance perovskite emitters.

In the ‘device engineering’ section, we will provide a comprehensive introduction to PeLED devices, including their

architectures (conventional and inverted), working mechanisms, and the history of their development since the 1990s. We will then focus on four factors that govern the external quantum efficiencies (EQEs) of PeLEDs: i.e., the balance of electron/hole injection, the parasitic loss of injected carriers, the electroluminescence (EL) quantum yields (ELQYs) of perovskite emitters, and the light extraction properties of the entire device. We finally analyse strategies for the improvement of these four factors in an effort to help guide the next-generation design of PeLEDs.

1. Materials

1.1. Dimensional engineering

The term ‘perovskite’ originates from the mineral calcium titanate (CaTiO_3), which was discovered by the German mineralogist Gustav Rose in 1839 and named in honour of the Russian mineralogist Count Lev Aleksevich von Perovski [1]. Now the term perovskite generally refers to a broad category of materials that share a related crystal structure to CaTiO_3 , but is perhaps most synonymous with the MHPs which demonstrate a unique set of optoelectronic properties. Chief among these special properties is their amenability towards modification through material composition and dimensionality, which has enabled enormous strides in their performance as light-emitting media, as we discuss below.

1.1.1. Three-dimensional perovskites. The basic structure of 3D ‘bulk’ MHPs materials is ABX_3 , which consists of corner-sharing BX_6 octahedra in all three dimensions, where X is typically a halide anion (i.e. Cl^- , Br^- or I^-); B is generally a divalent metal that can adopt octahedral coordination (e.g. Ge^{2+} , Sn^{2+} or Pb^{2+}); and A is a monovalent cation that fits in the space enclosed by eight adjacent corner-sharing BX_6 octahedra (as shown in figure 1(a)). Geometrically, the B-site cations have a six-fold octahedral coordination to the surrounding X-site anions, and the A-site cations have a 12-fold coordination between the corner-sharing BX_6 octahedra. When the A-site is occupied by organic cations like methylammonium (MA^+) or formamidinium (FA^+), the related compounds are commonly called hybrid organic–inorganic perovskites. On the other hand, when the A-site is solely occupied by inorganic cations like Cs^+ or Rb^+ , the related compounds are often referred to as all-inorganic perovskites.

The formation of the ABX_3 perovskite structure needs to fulfil three requirements: maintaining the stoichiometry of ABX_3 , retaining the (distorted) octahedral coordination of the

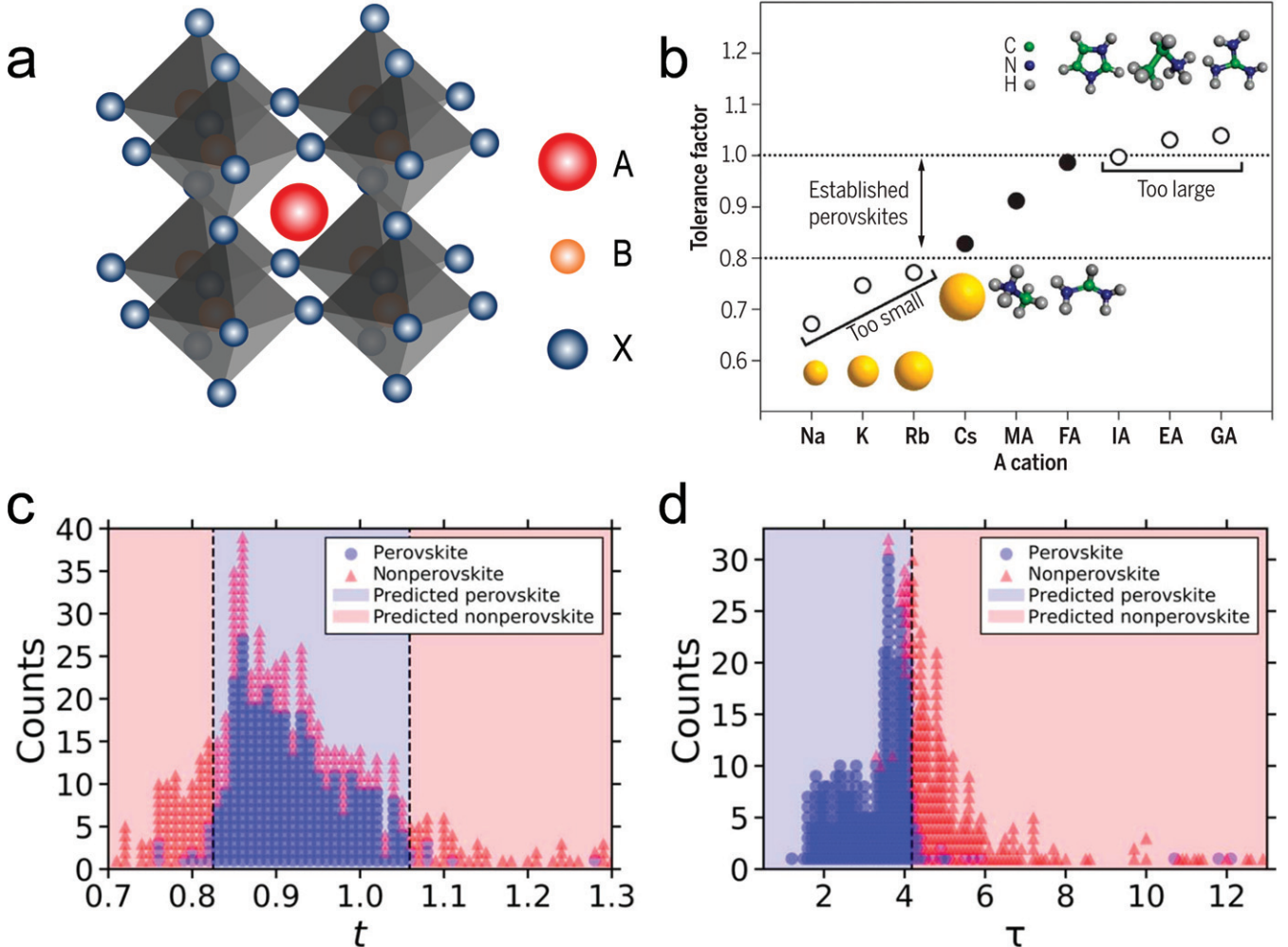


Figure 1. (a) The local atomic structure of a cubic perovskite. (b) Tolerance factor of an APbI_3 perovskite with different A-site cations, where MA, FA, IA, EA, and GA refer to methylammonium, formamidinium, imidazolium, ethylamine and guanidinium, respectively. (c) A decision tree classifier determines that the optimal bounds for perovskite formability using t are $0.825 < t < 1.059$, which yields a classification accuracy of 74% for 576 experimentally characterized ABX_3 solids. (d) τ achieves a classification accuracy of 92% on the set of 576 ABX_3 solids based on perovskite classification for $\tau < 4.18$. (b) From [8]. Reprinted with permission from AAAS. (c), (d) Reproduced from [15]. CC BY 4.0.

B-site cation and organizing all the BX_6 octahedra in a corner-sharing 3D network [2, 3]. $\text{A}_2\text{BB}'\text{X}_6$ double perovskites and A_3XY antiperovskite subclasses also belong to the perovskite family, but they have not yet shown promise for optoelectronic applications and are beyond the scope of this review (we refer the reader to reference [3] discussing these types of perovskites). To quantitatively, or at least qualitatively, predict the possible formation of a stable ABX_3 perovskite structure, several descriptors have been developed:

(i) Goldschmidt tolerance factor (t). This is the most widely used descriptor and is defined as $t = \frac{r_A + r_X}{\sqrt{2(r_B + r_X)}}$, where r_A , r_B , and r_X are the corresponding ionic radii of the A, B, and X ions [4]. In general, a stable perovskite structure can be formed when $0.8 \leq t \leq 1$, as shown in figure 1(b). For a perfectly symmetric cubic perovskite structure, $t = 1$, which adopts the cubic space group of $Pm\bar{3}m$ (typified by KMgF_3) [5]. For other t values ($0.8 \leq t < 1$), less-symmetric perovskite structures with lattice distortions (e.g. tetragonal, hexagonal, and

octahedral phases) can be formed [6]. Taking the APbI_3 system ($\text{B} = \text{Pb}$ and $\text{X} = \text{I}$) as an example, where $r_{\text{Pb}} = 1.2 \text{ \AA}$ and $r_{\text{I}} = 2.2 \text{ \AA}$, it can be estimated that r_A cannot exceed $\sim 2.6 \text{ \AA}$ (assuming that $t = 1$) [7]. Considering that C–C or C–N bond lengths are $\sim 1.4 \text{ \AA}$, only very small organic molecules that consist of two or three atoms (excluding hydrogens) can occupy the void in the lattice (as shown in figure 1(b)) [8]. We summarise the effective radii of some cations and anions generally used in perovskite formation in table 1 [9–11].

(ii) Octahedral factor (μ). This relates to the stability of the BX_6 octahedron, and is defined as the ratio of r_B and r_X ($\mu = \frac{r_B}{r_X}$). Li and co-workers developed the (t , μ) map and concluded that the stable region for halide perovskite resides within the $0.813 < t < 1.107$ and $0.377 < \mu < 0.895$ parameter space, which has since become an empirical ruleset for the perovskite family [12, 13]. However, both t and μ values cannot quantitatively provide a straightforward relationship to the lattice stability of perovskite, and more reliable descriptors that establish this relationship are being developed.

Table 1. Effective radii of selective cations and anions, adapted from references [9–11].

Cations	Effective radius (Å)	Cations	Effective radius (Å)
Ammonium $[\text{NH}_4]^+$	1.46	Na^+	1.02
Hydroxylammonium $[\text{H}_3\text{NOH}]^+$	2.16	K^+	1.38
Methylammonium $[\text{CH}_3\text{NH}_3]^+$	2.17	Rb^+	1.52
Hydrazinium $[\text{H}_3\text{N}-\text{NH}_2]^+$	2.17	Cs^+	1.69
Azetidinium $[(\text{CH}_2)_3\text{NH}_2]^+$	2.50	Ge^{2+}	0.73
Formamidinium $[\text{NH}_2(\text{CH})\text{NH}_2]^+$	2.53	Sn^{2+}	1.18
Imidazolium $[\text{C}_3\text{N}_2\text{H}_5]^+$	2.58	Pb^{2+}	1.20
Dimethylammonium $[(\text{CH}_3)_2\text{NH}_2]^+$	2.72	Anions	
Ethylammonium $[(\text{C}_2\text{H}_5)\text{NH}_3]^+$	2.74	Cl^-	1.81
Guanidinium $[\text{C}(\text{NH}_2)_3]^+$	2.78	Br^-	1.96
Tetramethylammonium $[(\text{CH}_3)_4\text{N}]^+$	2.92	I^-	2.20

(iii) Other descriptors (η and τ). In 2017, Yin *et al* introduced the η value as an additional descriptor, which can describe the fraction of volume in a crystal structure that is occupied by constituent atoms [14]. The η value is defined by the equation $\eta = \frac{V_A + V_B + 3V_X}{a^3}$, where V_A , V_B , and V_X are atomic volumes of A, B, and X ions in the rigid sphere model, respectively, and a is the lattice constant of the cubic cell. According to the linear relationship between decomposition energies (ΔH_D), which are calculated by first-principles density functional theory (DFT), and the value of $(t + \mu)^\eta$, a reliable prediction (with $\sim 90\%$ accuracy) of the relative stability for halide and chalcogenide perovskite compounds can be made, which suggests that the descriptor of $(t + \mu)^\eta$ performs better than that of t , μ or $t + \mu$. In addition, in 2019, Bartel and co-workers developed a new tolerance factor (τ) to predict the stability of oxide and halide perovskites, which is defined as $\tau = \frac{r_X}{r_B} - n_A(n_A - \frac{r_A/r_B}{\ln(r_A/r_B)})$, where n_A is the oxidation state of the A cation and r_A should be larger than r_B . Compared with t (74% accuracy), τ correctly predicted 92% of compounds as perovskite or non-perovskite structures for an experimental dataset of 576 ABX_3 materials ($X = \text{O}^{2-}$, F^- , Cl^- , Br^- , I^-), as shown in figures 1(c) and (d). Another crucial advantage of τ is the monotonic dependence of perovskite stability on τ , which indicates that the probability of perovskite formation increases when τ decreases [15].

1.1.2. Perovskite derivatives: two dimensional and quasi-two-dimensional perovskites. Besides the 3D bulk perovskites, the ‘2D’ systems confined in one direction by ligands are the most investigated of the perovskite structures as they offer many additional opportunities for controlling the material properties and designing their applications. When an A-site cation is too large to fit into the cage provided by the 12 nearest-neighboring X-site anions, it causes a severe distortion of the cubic structure. In this situation ($t \gg 1$), the large A-site cation separates the corner-sharing inorganic BX_6 sheets by forming a spacing layer between them, leading to the growth of 2D structures. These novel 2D structures can be conceptually regarded as slices of the 3D perovskite structure, as shown in figure 2. It should be noted that the reduced dimensionality from 3D to 2D refers to the connectivity of the corner-sharing BX_6 octahedra in the periodic crystal structure. Besides the moniker of 2D perovskites [16], a

variety of other terms are used in the literature to describe this kind of structure, such as layered perovskites [17], multiple-quantum-well (MQW) perovskites [18], Ruddlesden–Popper (RP) perovskites [19], and Dion–Jacobson (DJ) perovskites [20]. From our perspective, since the crystal periodicity of the original 3D perovskite is destroyed, the physical properties of these reduced-dimensional materials, including their electronic states and space groups, are quite different from the 3D counterparts; hence we propose that ‘perovskite’ has its clear definition and is not an entirely appropriate term for referring to these other structures [3]. Therefore, we would ideally categorize the structures generally named as ‘2D/quasi-2D perovskites’ in the literature as ‘perovskite derivatives’, however, we will still use the term ‘2D/quasi-2D perovskites’ to simplify our discussion below.

In the field of 2D perovskites, Mitzi and co-workers laid the foundation and contributed many pioneering works concerning structural studies, deposition techniques, and optoelectronic devices [7, 21]. Similarly, the Kanatzidis group have also brought a deep understanding of the chemical and physical properties, more recently at the molecular level [22]. Early examples of 2D perovskites are based on RP perovskites. RP perovskites are named after Ruddlesden and Popper, who reported a new compound Sr_2TiO_4 with a K_2NiF_4 type structure [23]. Subsequently, by sintering SrCO_3 and TiO_2 in a molar ratio of 3:2, they synthesized $\text{Sr}_3\text{Ti}_2\text{O}_7$ which exhibited a crystal structure between that of Sr_2TiO_4 (K_2NiF_4 type) and SrTiO_3 (perovskite type) [24]. This oxide-based structure can be thought of as having alternating SrTiO_3 and SrO layers, and can be described by the formula of $\text{A}'_2\text{A}_{n-1}\text{B}_n\text{X}_{3n+1}$, where $\text{A}'\text{X}$ serves as the spacer (i.e. SrO) that separates the perovskite layers (i.e. SrTiO_3), and n is the number of octahedral layers in the perovskite-like stack (figure 2(a)) [25]. When $n = \infty$, it can be regarded as a 3D bulk perovskite without the $\text{A}'\text{X}$ spacing layer; if $n = 1$, there are only alternating BX_6 octahedra and $\text{A}'\text{X}$ spacing layers. Through dimensional engineering (modulating the n value), many optoelectronic properties can be tuned, which will be discussed later.

Besides inorganic molecules, the $\text{A}'\text{X}$ spacers have been extended to organic molecules, contributing to the booming development of hybrid organic–inorganic perovskites. Due to the chemical diversity and molecular dynamic properties of organic molecules, the crystallographic orientations of the

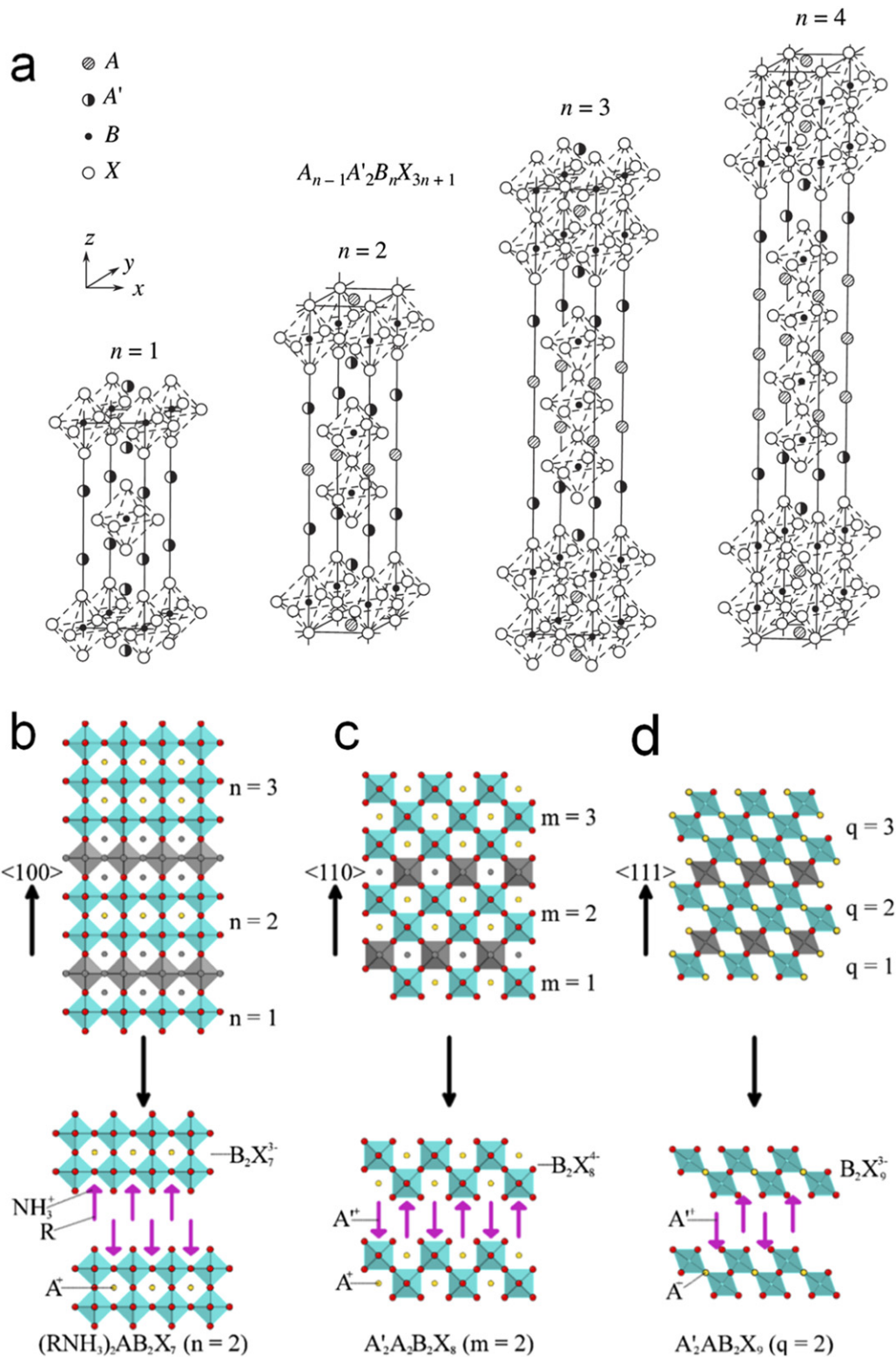


Figure 2. (a) Crystal structures of RP phases with n values of 1, 2, 3, and 4, respectively. (b)–(d) Schematic diagrams of the 2D organic–inorganic hybrid perovskites from different cuts of the 3D perovskite structure. (b) The $\langle 100 \rangle$ -oriented layered perovskites with a general formula of $A'_2A_{n-1}B_nX_{3n+1}$; (c) the $\langle 110 \rangle$ -oriented layered perovskites with a general formula of $A'_2A_mB_mX_{3m+2}$; (d) the $\langle 111 \rangle$ -oriented layered perovskites with a general formula of $A'_2A_{q-1}B_qX_{3q+3}$. (a) Reprinted by permission from Springer Nature Customer Service Centre GmbH: Crystallography Reports [25] © 2000. (b)–(d) Reprinted with permission from [21]. Copyright (2016) American Chemical Society.

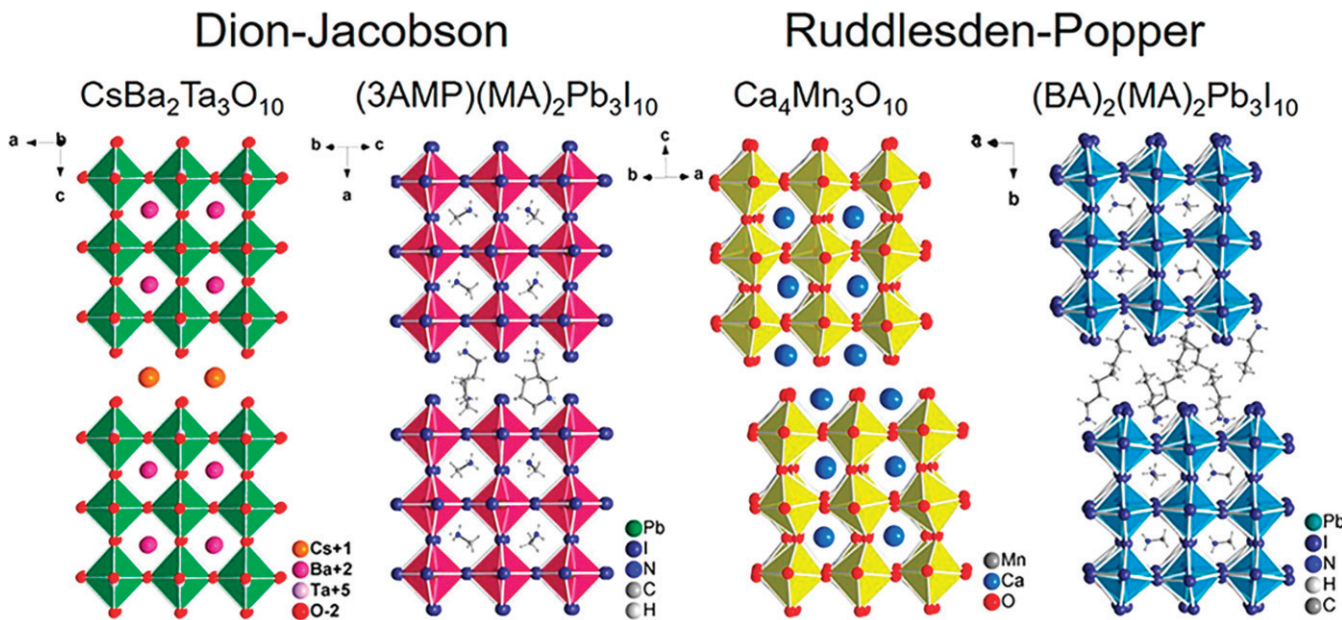


Figure 3. Comparison between the DJ and RP phases for both oxide and halide perovskite structures, where 3AMP is 3-(aminomethyl)piperidinium, and BA is butylammonium. Reprinted with permission from [26]. Copyright (2018) American Chemical Society.

resultant frameworks exhibit more complicated behaviours than their 3D counterparts. In terms of the BX_6 connectivity, corner-sharing, edge-sharing, and face-sharing of the octahedra are available when using different organic spacers [26–28]. Figures 2(b)–(d) show three types of 2D perovskite that consists of corner-sharing BX_6 octahedra based on the $\langle 100 \rangle$ -, $\langle 110 \rangle$ - and $\langle 111 \rangle$ -oriented structures, which have the general formulas $\text{A}'_2\text{A}_{n-1}\text{B}_n\text{X}_{3n+1}$, $\text{A}'_2\text{A}_m\text{B}_m\text{X}_{3m+2}$, and $\text{A}'_2\text{A}_{q-1}\text{B}_q\text{X}_{3q+3}$, respectively [21]. For a $\langle 100 \rangle$ -oriented 2D perovskite, the terminating surface comprises single halide atoms protruding from each octahedral corner. In the $\langle 110 \rangle$ -oriented case, two halide atoms from each octahedral edge constitute the terminating surface. For $\langle 111 \rangle$ -oriented 2D systems, each BX_6 octahedra on the surface contributes three halide atoms to the terminating surface within the octahedral face. A layer of larger organic cations separates the perovskite framework accordingly.

To date, the literature on the 2D perovskite family is dominated by $\langle 100 \rangle$ -oriented type systems. The $\langle 100 \rangle$ -oriented oxide 2D perovskites can be further categorized as RP, DJ and Aurivillius phases, which possess the general formulae $\text{A}'_2\text{A}_{n-1}\text{B}_n\text{O}_{3n+1}$, $\text{A}'\text{A}_{n-1}\text{B}_n\text{O}_{3n+1}$ and $(\text{Bi}_2\text{O}_2)(\text{A}_{n-1}\text{B}_n\text{O}_{3n+1})$, respectively [22]. Besides this, halide 2D perovskites maintain a similar nomenclature to oxide 2D perovskites. Here, the different characteristics for these 2D perovskites with the RP, DJ or Aurivillius phases are distinguished by two factors: one is the choice of cation spacers that separate the layers, and the other is the offsetting of the layers from each other. Figure 3 shows select crystal structures of the RP and DJ phases for both oxide and halide perovskites [26]. For the RP phases, such as $\text{Ca}_4\text{Mn}_3\text{O}_{10}$ and $(\text{BA})_2(\text{MA})_2\text{Pb}_3\text{I}_{10}$ (BA = butylammonium), the separating cation spacers are two Ca atoms and two butylammonium molecules, respectively, and the perovskite slabs have an offset

equal to a $(\frac{1}{2}, \frac{1}{2})$ in-plane displacement. For the DJ phases, such as $\text{CsBa}_2\text{Ta}_3\text{O}_{10}$ and $(3\text{AMP})(\text{MA})_2\text{Pb}_3\text{I}_{10}$ (3AMP = 3-(aminomethyl)piperidinium), the separating cation spacers are one Cs atom and one 3AMP molecule, respectively, and the perovskite slabs show zero in-plane displacement. It is noteworthy that the displacement of the perovskite slabs in the DJ phases can be either $(\frac{1}{2}, 0)$ or zero depending upon the separating cation spacers (e.g. $(\frac{1}{2}, 0)$ for KLaNb_2O_7 and zero for $\text{CsLaNb}_2\text{O}_7$) [29]. The Aurivillius phase can be treated as a specific type of RP phase, which has not been realized in halide perovskites. The separating motif for the Aurivillius phase is a rock-salt Bi_2O_2 layer and the displacement of the perovskite slabs is a $(\frac{1}{2}, \frac{1}{2})$ translation [30]. More recently, alternating cations in the interlayer space (ACI), where different cations order along the interlayer space, have been leveraged [31, 32]. To date, GA^+ is the only reported cation that can form a stable ACI-type structure, and the perovskite slabs show a $(\frac{1}{2}, 0)$ displacement.

The term ‘quasi-2D perovskite’ refers to the combination of 2D perovskites (with small n values and excitonic nature) and 3D perovskites (or large- n 2D perovskites with a non-excitonic nature that closely resemble the 3D perovskites). Despite the precise control of precursor stoichiometry, solution-processed quasi-2D perovskite films generally contain domains with various n values that are associated with the different reaction rates between PbX_2 and AX or $\text{A}'\text{X}$ salts [33].

The orientation of 2D and 3D components in quasi-2D thin films has a significant impact on the device performance, and is affected by many factors including additives, substrates, anti-solvent dripping, processing temperature, and the precursor preparation method [34–37]. For example, Chen *et al* reported that organic additives like N-(3-aminopropyl)-2-pyrrolidinone (NAP) could aid the vertical growth of 2D perovskites with

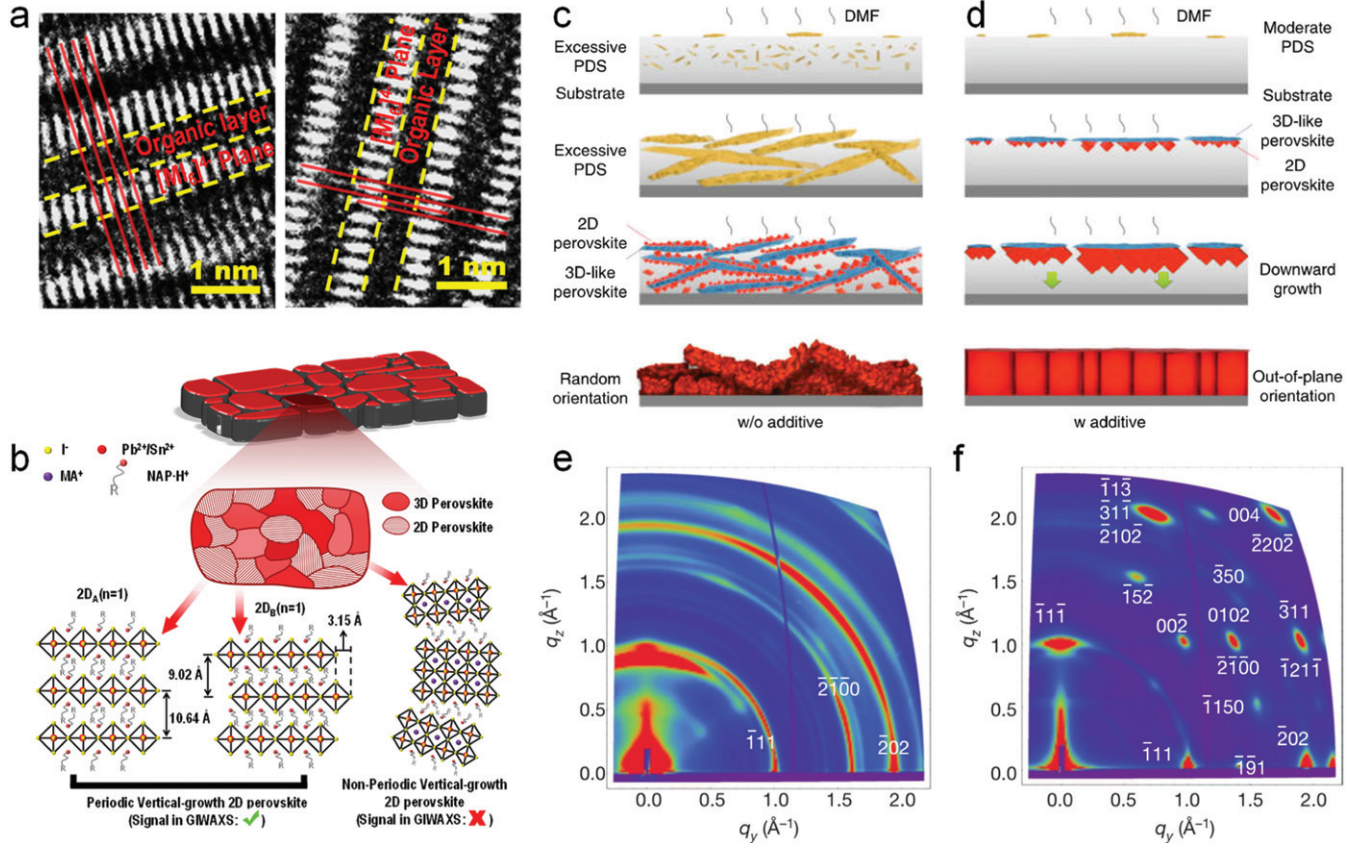


Figure 4. (a) High-resolution transmission electron micrographs of two types of perovskite lattice in $n = 1$ 2D perovskites. (b) Schematic diagram of the nanostructure of quasi-2D hybrid perovskite grains. Illustration of the induced nucleation of 3D-like perovskites and growth of RP crystals without (c) or with (d) excess AX additives modification. The GIWAXS patterns of the $(\text{BA})_2(\text{MA})_3\text{Pb}_4\text{I}_{13}$ perovskite films prepared by the room-temperature (e) and hot-casting (f) methods. (a), (b) Reprinted from [38], Copyright (2018), with permission from Elsevier. (c), (d) Reprinted by permission from Springer Nature Customer Service Centre GmbH: Nature Communications [39] © 2020. (e), (f) Reprinted by permission from Springer Nature Customer Service Centre GmbH: Nature [44] © 2016.

a coherent 2D/3D interface, and two types of $n = 1$ 2D perovskites were found in their case (one with perfect lattice matching and another with a half lattice shift), as shown in figures 4(a) and (b) [38]. The effects of other additives including NH_4Cl , NH_4I , MACl , MABr , and MAI have also been systematically studied, and it was shown that they can suppress the nucleation of one-dimensional PbI_2 -DMF-contained solvate phases (PDS) by increasing the solubility of $[\text{PbI}_6]$ octahedral colloids, thus facilitating control of the crystal orientation [39]. For example, as shown in figure 4(c), the abundance of PDS microcrystals formed at the liquid-air interface and inside the solution can lead to the rapid growth of randomly-oriented perovskite crystals during the annealing process. In contrast, as shown in figure 4(d), when PDS precipitation is suppressed inside the solution by the addition of NH_4Cl , the PDS at the top of the liquid phase directs the downward growth of RP-phase perovskites.

A promising alternative tool for controlling the quasi-2D perovskite structures is the NC pinning process, which introduces a nonvolatile solvent (e.g. toluene, chlorobenzene, or chloroform) to induce immediate crystallization during the spin-coating. It can also be used to influence the crystal growth and orientation of quasi-2D perovskites [40–42]. For example,

after introducing ethyl acetate as an anti-solvent during perovskite film formation, because of the interacting sequence, the 2D component tends to form on the film surface while the 3D component tends to accumulate at the bottom side [43]. This distribution gradient between the 2D-rich (lower- n) and 3D-rich (higher- n) phases drives electron transfer along the perovskite structure. Therefore, it is possible to tune the direction of charge transfer according to the anti-solvent process for distinct conventional (n-i-p) or inverted (p-i-n) device architectures (the detailed architectures will be discussed in section 3.1). In addition, the hot-casting process was also developed to modulate the crystal orientation of the 2D perovskite film [44]. According to the grazing incidence wide-angle x-ray scattering (GIWAXS) results shown in figures 4(e) and (f), a polycrystalline film with random crystal orientation is formed in the room-temperature-cast process. Meanwhile, the hot-cast film is highly oriented with 2D perovskites grown perpendicular to the substrate. This vertical growth facilitates charge transport along the vertical direction. Other reports show that the hot-casting process limits the formation of intermediate phases (e.g. PbI_2 crystals and solvate complexes) at higher temperatures, and therefore promotes intercalation of ions and decreases the nucleation barrier. Consequently, a high

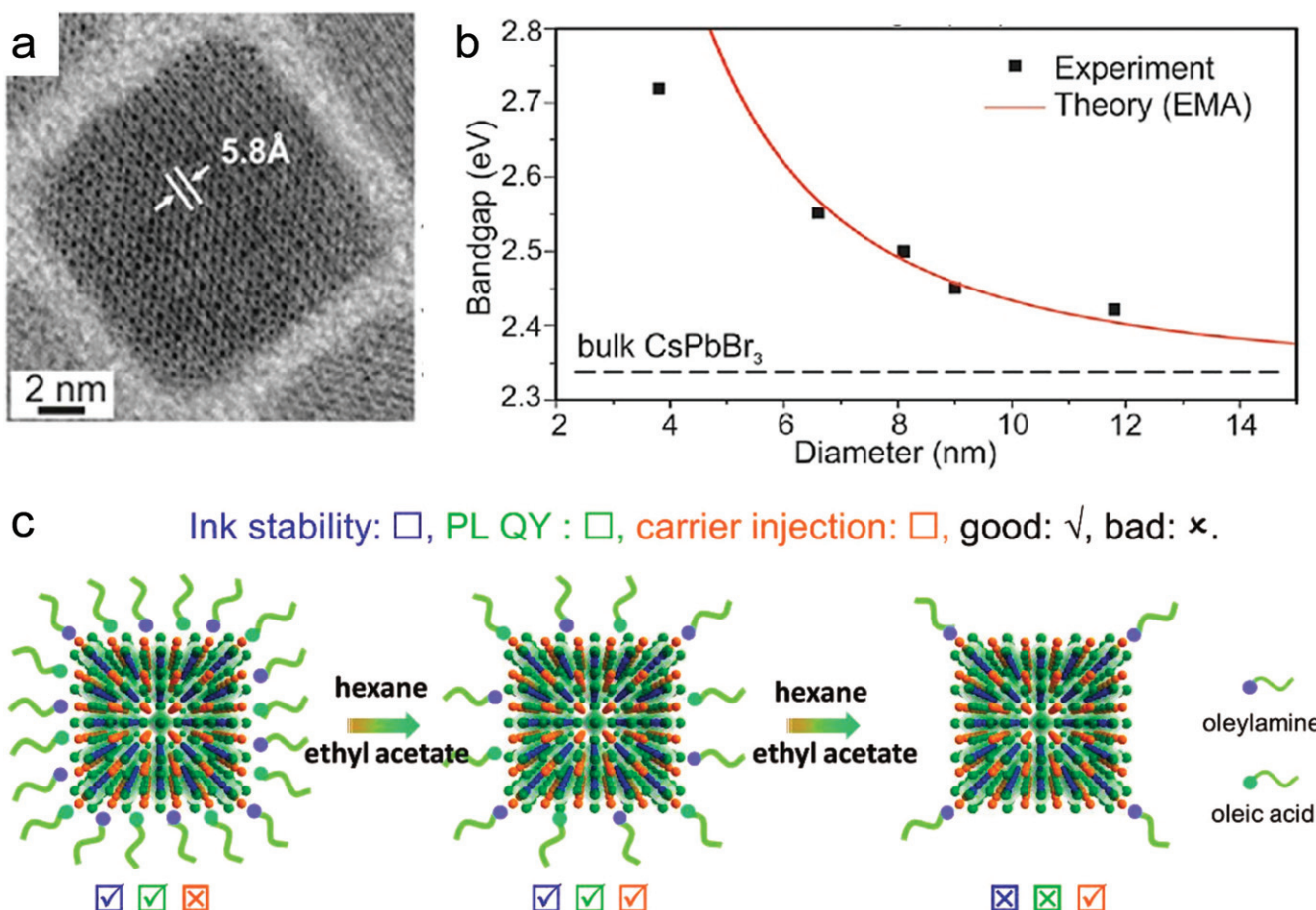


Figure 5. (a) Transmission electron micrograph of a CsPbBr_3 NC. (b) Experimental and theoretical (effective mass approximation) bandgap values for different sizes of CsPbBr_3 NC. (c) Illustration of the effect of surface ligand density on the ink stability, PLQY and carrier injection for CsPbBr_3 QDs. (a), (b) Reprinted with permission from [67]. Copyright (2015) American Chemical Society. (c) [77] John Wiley & Sons. © 2017 WILEY-VCH Verlag GmbH & Co. KGaA, Weinheim.

spinning temperature is beneficial for the growth of small- n perovskite at the bottom of the film [45, 46].

Besides the formation of 2D and quasi-2D perovskite thin films from precursor solutions, the synthesis of 2D perovskite nanoplatelets (NPLs), which possess similar characteristics as 2D perovskite thin films (e.g. structural crystallography and optoelectronic properties), offers an alternative pathway towards obtaining high-purity and high-quality 2D perovskites. For example, Ling *et al* introduced octylammonium bromide ($\text{C}_8\text{H}_{17}\text{NH}_3\text{Br}$) as a long-chain ligand to form layered perovskites along the $\langle 100 \rangle$ and $\langle 110 \rangle$ facets of the 3D MAPbBr_3 perovskite, which selectively inhibited the crystal-growth direction and led to the successful formation of 2D perovskite NPLs [47]. The n value of 2D perovskite NPLs can also be facilely modulated by adjusting the ratio between organic ligands and A-site cations [48]. When reducing the n value of 2D perovskite NPLs, obvious blue shifts of the PL transpire due to strong quantum confinement, especially when $n < 4$ and excitons dominate, as in 2D and quasi-2D perovskites [49, 50]. Zeng *et al* reported blue-emitting CsPbBr_3 NPLs with PLQY up to 96% and full-width at half-maximum

(FWHM) of 12 nm via *in-situ* passivation of Br vacancies [51]. Along the same vein, through careful surface ligand treatment by di-dodecyl dimethyl ammonium bromide or trioctylphosphine oxide, highly-emissive CsPbBr_3 and FAPbBr_3 NPLs with deep-blue emission were successfully synthesized [52, 53]. These well-controlled 2D perovskite NPLs show promising potential in light-emitting applications due to their high PLQY and narrow emission line width originating from the phase purity compared to quasi-2D perovskites. The development of reliable NPL devices still entails a number of obstacles however, especially concerning poor charge-transport due to the insulating ligands and strong exciton-phonon interactions [54].

1.1.3. Perovskite quantum dots and nanocrystals. When the size of a semiconductor crystal is restricted in multiple directions and comprises merely hundreds of atoms, it is usually referred to as an NC. If the size of an NC is smaller than the delocalization volume of the electronic states (in other words, the electron de Broglie wavelength exceeds the semiconductor size), the charge carriers or excitons will be tightly ‘quantum confined’, and the NC is referred to as a

QD. This quantum confinement effect enlarges the separation between energy bands with decreasing particle size [55, 56]. The bandgaps [$E_{g(QD)}$] of QD systems can be quantitatively estimated using the Brus equation: $E_{g(QD)} - E_g \approx \frac{\hbar^2 \pi^2}{2R^2} \left(\frac{1}{m_e} + \frac{1}{m_h} \right) - \frac{1.8e^2}{\epsilon R} + S$, where E_g is the bandgap of the bulk material with infinite size, m_e and m_h are the effective mass of the electron and hole, respectively, R is the radius of the nanoparticle, ϵ is the dielectric coefficient at optical frequencies and S is a smaller term that can be neglected [57, 58]. The first term on the right-hand side of the formula describes the confinement effect and the second term is the Coulomb term. When R is much smaller than the Bohr radii (e–h separation) of a certain material (e.g. 4.3 nm for Si, 11.5 nm for Ge and 12.4 nm for GaAs), the confinement term dominates and $E_{g(QD)} \gg E_g$. However, when R is much larger than the Bohr radii, the Coulomb term dominates, and $E_{g(QD)} \approx E_g$ [59].

MHPs can also be synthesized in the form of colloidal QDs or NCs with a general size range between 3 and 30 nm. Taking that exciton and carrier delocalization in MHPs is on the order of 10 nm (discussed in detail below), the effects of quantum confinement are present but relatively minor for most studied NCs. Nevertheless, the terms ‘QD’ and ‘NC’ are both broadly applied to 0D MHP nanomaterials. The hot-injection and ligand-assisted re-precipitation (LARP) methods are two common strategies for the synthesis of MHP QDs and NCs, and can also be tailored to form nanomaterials with different shapes (i.e. nanocubes, nanoplatelets, nanosheets, nanorods, and nanowires) [60–66]. In 2015, Protesescu *et al* reported the first successful preparation of CsPbX_3 ($X = \text{Cl}, \text{Br}$, and I) NCs using the hot-injection method [67]. The resultant monodisperse colloidal NCs (figure 5(a)) cover the entire visible spectrum ranging from 410 to 700 nm with respectable PL quantum yields (PLQY, 50%–90%) and narrow FWHM, covering 140% of the NTSC colour standard. By carefully controlling the reaction conditions, the diameters of CsPbBr_3 NCs have been precisely modulated in the size range of 4–15 nm, with a bandgap that blueshifts with decreasing NC size (figure 5(b)), allowing yet further control of the emission colour. Other novel synthetic methods for perovskite QDs and NCs have been developed, including microwave-assisted approaches [68], ultrasonication [69], mechanically milling/grinding [70], chemical vapour deposition [71], and solvothermal synthesis [72].

Organic ligands, which serve as stabilizers and play important roles in the synthesis and dispersion of perovskite QDs and NCs, are attached to the surface of QDs and NCs through covalent, coordinate or ionic bonding. This directly affects the PL intensity and lifetime of the material films, as well as the performance and stability of PeLEDs through the passivation of surface states [73]. By controlling the type, proportion and concentration of organic ligands, perovskite QDs and NCs with uniform size distribution and high PLQY approaching 100% can be synthesized [74]. Generally, organic ligands containing carboxyl and amino functional groups coordinate

strongly with metal cations and halogen anions [75, 76]. Zeng and co-workers have systematically investigated the ink stability, PLQY, and charge injection of perovskite QDs with different ligand densities [77]. Figure 5(c) illustrates the trade-off between better stability and PLQY but also poorer charge injection for perovskite QDs with high ligand density. Due to the poor conductivity of commonly used ligands (e.g. oleylamine and oleic acid), excessive surface coverage of perovskite QDs usually results in the assembled films having poor carrier injection and transport properties, but sparse ligand capping is incapable of providing the surface passivation needed for both high PLQY and stability. By accounting for the solvent polarity and perovskite ionicity that affect ionic and dynamic interactions, Li and coworkers judiciously selected hexane and ethyl acetate as a mixed solvent during the washing process, which assisted in finely controlling the ligand density [77]. The synergy between these parameters needs to be more widely considered for fabricating better PeLEDs. Strategies such as employing zwitterionic ligands, inorganic protective shells, and cross-linking matrices are also being developed to balance the relationship between the PLQY, stability and electrical properties of perovskite QDs and NCs [78–80].

1.1.4. One-dimensional (1D) perovskite nanowires (NWs).

The high surface area-to-volume ratio and structural anisotropy of 1D perovskite nanowires (NWs) have already been exploited in sensors and photodetectors [81, 82]. However, there are only a few reports of working LEDs based on perovskite NWs, which reflects the difficulty of integrating NWs into thin film devices. The solution-synthesis of MAPbBr_3 NW arrays for LED applications, with PL and EL emission at 533 nm, was pioneered by Yang and co-workers [65]. The same group have also systematically synthesised all-inorganic CsPbBr_3 and CsPbI_3 NWs [83]. More recently, CsPbI_3 NWs grown along the $\langle 011 \rangle$ crystal direction have been showcased for promising LED performance in the pure-red region [84]. The anisotropic nature of perovskite NWs has also opened a new research avenue for strong light out-coupling in PeLEDs. Along a similar vein, the formation of a Fabry–Perot cavity in 1D perovskite NWs, constructed from the waveguide along the axial direction and the two end facets, is ideal for optical amplification in lasing [64].

1.2. Compositional engineering

One of the most attractive properties of MHPs is the facile bandgap tunability, which is especially convenient for fabricating multi-colour PeLEDs. Many correlated factors affect the bandgaps of perovskites, including the size of ions, crystallinity, lattice distortion and deposition methods [85, 86]. Recent research has affirmed that the bandgaps of perovskites are primarily determined by the atomic energy levels of metal cations and halide anions, and secondarily affected by the cation–anion interaction strength, making compositional engineering the premier method to modulate the emission properties of perovskites [87]. For example, as shown in

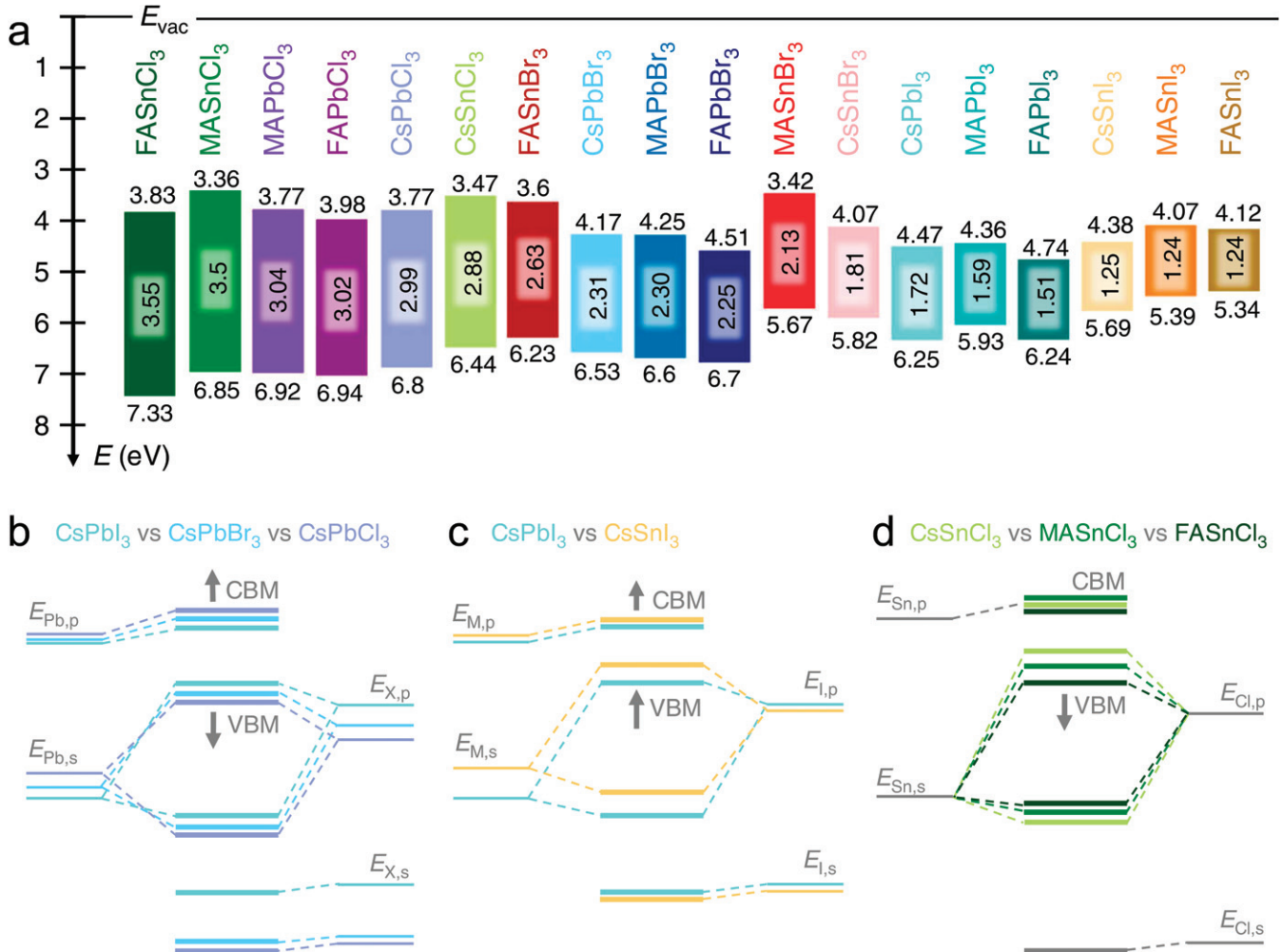


Figure 6. (a) Schematic diagram indicating the energy levels and bandgaps of 18 representative MHPs. (b)–(d) are schematic energy levels in ABX_3 perovskites identified by the tight-binding analysis, which represent trends in changing the halide anions, metal cations and A-site cations, respectively. Arrows indicate the shift of energy levels. (a)–(d) Reprinted by permission from Springer Nature Customer Service Centre GmbH: Nature Communications [87] © 2019.

figure 6(a), when the A-site cation is Cs^+ , MA^+ , or FA^+ , B-site cation is Pb^{2+} or Sn^{2+} , X-site anion is Cl^- , Br^- or I^- , 18 distinct perovskite systems can be classified, even before the components and their stoichiometry are mixed. The positions of the valence band maxima (VBM) and conduction band minima (CBM) for these 18 perovskites have been determined by ultraviolet photoelectron spectroscopy and inverse photoelectron spectroscopy, and corroborated through DFT calculations based on a nearest-neighbour tight-binding model. In general, the VB can be identified as the anti-bonding state formed from the combination of the outermost s orbit of the metal and outermost p orbit of the halide. Meanwhile, the CB is composed of anti-bonding states which primarily arise from the outermost p orbit of the metal [87]. Consequently, the type of ions has a profound impact on the energy levels of perovskites.

1.2.1. Bandgap tuning through A, B and X ions. (i) Influence of X-site anions. For the Pb-based perovskites shown in figure 6(b), solely varying the X anion from I^- to Br^- to Cl^- reduces the Pb-X distances, which pushes more electron density onto the higher-energy Pb atoms, thereby shifting the

CBM upward. The concomitant shift of the VBM is influenced by three competing effects: first, a dramatic downshift of the VBM because of the increasing electronegativity of the X anions; second, the upshift of the $6s$ orbit of the metal; and third, the increased Pb, s/X , p hybridization strength, which partially offsets the downshift of the VBM. Overall however, the VBM downshifts when changing the X anion from I^- to Br^- to Cl^- , which taken with the upshifted CBM results in an increased bandgap.

(ii) Influence of B-site cations. The B-site cation strongly impacts the overall atomic levels in the perovskite. For example, as illustrated in figure 6(c), when solely replacing Pb with Sn in perovskite lattice, the atomic levels shift upwards due to the smaller electronegativity of Sn, which consequently leads to an upshift of both VBM and CBM. Moreover, for the Sn atom, the upshift of the s level is larger than that of the p level, so the bandgap of the Sn-based perovskite is lower than that of its Pb-based equivalent.

(iii) Influence of A-site cations. In typical MHPs, the bandgaps are only weakly dependent on the A-site organic

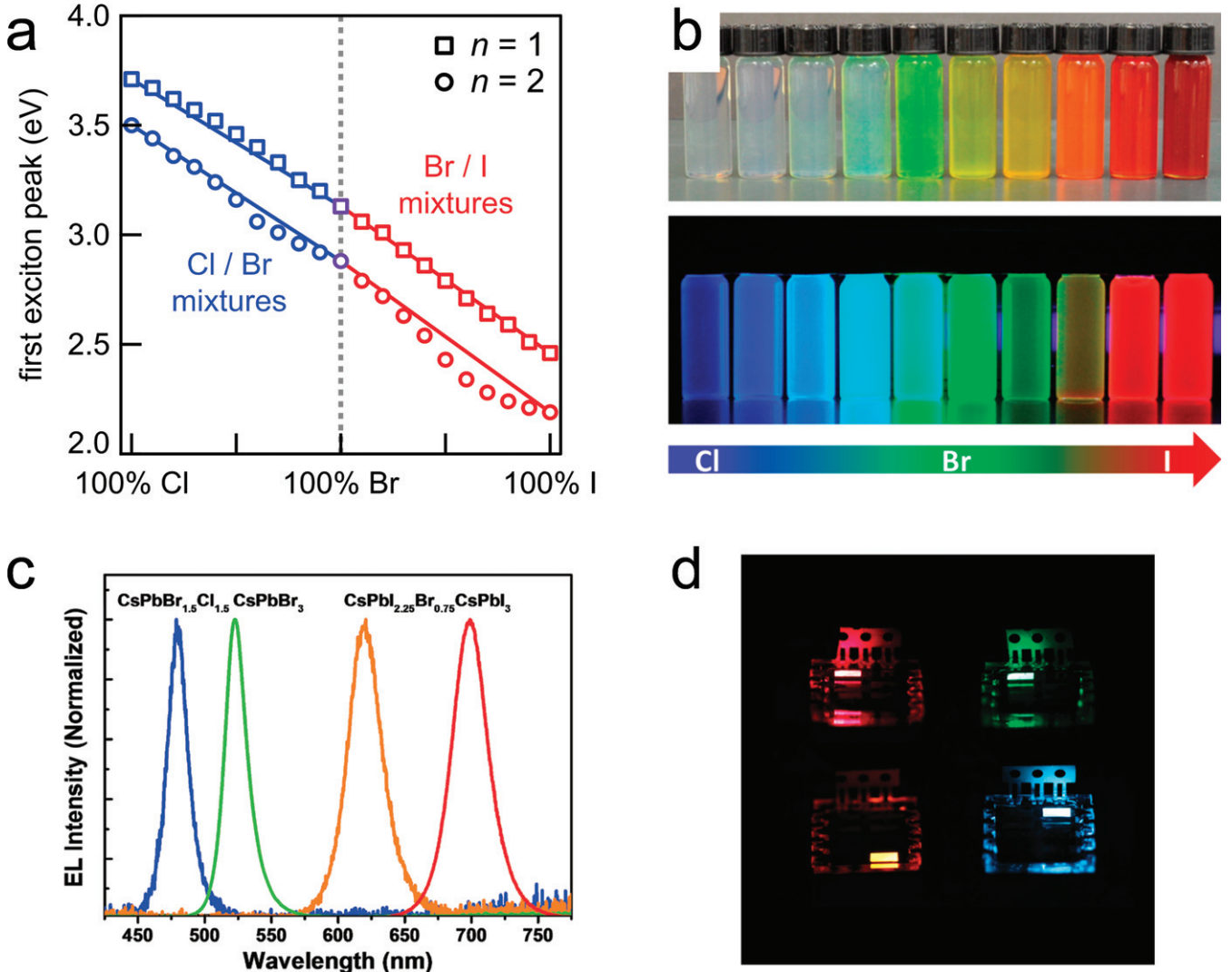


Figure 7. (a) The first excitonic absorption peak as a function of halide composition in $n = 1$ and $n = 2$ $L_2(FAPbX_3)_{n-1}PbX_4$ perovskites. (b) Image of $MAPbX_3$ perovskite colloidal solutions in toluene under UV lamp exhibiting PL emission from 438 to 660 nm. (c), (d) EL spectra and respective images of red, orange, green and blue Cs-based PeLEDs. (a) Reprinted with permission from [93]. Copyright (2016) American Chemical Society. (b) Reprinted with permission from [96]. Copyright (2016) American Chemical Society. (c), (d) Reproduced from [95]. CC BY 4.0.

cations since the $2p$ orbitals of carbon and nitrogen and the $1s$ orbital of hydrogen do not contribute significantly to the density of states near the Fermi level [88]. Instead, the A-site cation only indirectly affects the electronic structure by changing the volume of the ABX_3 lattice or introducing a distortion (of, for example, the anionic framework through hydrogen bonding and van der Waals interactions upon thermal and pressure perturbations) in the ideal perovskite structure. Structural deformations, such as octahedral tilting and distortion of the octahedra in the perovskite framework, will reduce the hybridization between the B and X states throughout the crystal, causing a downshift of both the VBM and CBM [87]. The A-site cation also affects the symmetry of the perovskite lattice, and a more symmetric lattice can result in a reduced bandgap of the perovskite [89]. For example, $MAPbI_3$ perovskites at $Pm\bar{3}m$ (cubic), $I4/mcm$ (tetragonal) and Pmn (orthorhombic) phases (with gradual loss of symmetry) exhibit

bandgaps of 1.54, 1.57 and 2.31 eV, respectively [90]. In addition, as shown in figure 6(d), increasing the size of the A-site cation from Cs^+ to MA^+ to FA^+ generally increases the lattice volume, which lowers the energy levels of the B-site cation because of the reduced confinement effect.

Early attempts to achieve multi-colour PeLEDs were based on simple halide substitutions in 3D $MAPbCl_xBr_yI_{3-x-y}$ films [91, 92]. This simple strategy can also be applied to 2D perovskite derivatives and NCs, allowing access to a wide colour gamut through composition control. For example, for a fixed n value in 2D perovskite derivatives, the excitonic absorption peak (i.e. emission wavelength) can be almost linearly modulated with the halide stoichiometry (figure 7(a)) [93]. The demonstrations of multi-colour $CsPbX_3$ [74, 94, 95], $MAPbX_3$ [96, 97], and $FAPbX_3$ ($X = Cl, Br, I$) [98] colloidal NCs also show high PLQY exceeding 80% and facile tunable emission in the visible range from red to blue (figures 7(b)–(d)).

However, light or electric field-induced halide redistribution in mixed halide films usually results in an inevitable shift of the emission spectra during continuous operation, which is undesirable in PeLEDs [99, 100]. Fortunately, quantum confinement effects in low-dimensional pure-halide perovskites (e.g. 2D perovskite derivatives and perovskite QDs) can also be utilised to modulate the emission colour without any spectral shift.

Besides the halide (X-site) composition, engineering of the A-site and B-site cations is also an effective approach to control and stabilize the perovskite lattice, allowing further improvements to the optoelectronic properties. Small-size alkali metal cations such as Na^+ , K^+ , and Rb^+ can be used as dopants to modulate the tolerance factor [101], increase PLQY [102, 103], passivate defect states [104], and suppress halide segregation in perovskite films [105]. In terms of the B-site substitution, divalent (e.g. Ni [106], Cd [107], Cu [108], Ba [109], Zn [110]) and trivalent metals (e.g. Al [111], Bi [112], Sb [113], lanthanide [114]) have been intensively studied, which can offer diverse chemical solutions to fabricating perovskite materials with a desirable bandgap, high PLQY, good environmental stability and lower toxicity. Overall, the precise doping mechanisms should be investigated for the further design of perovskite materials with superb lighting properties and stability.

1.2.2. Effects of organic spacers and ligands in low-dimensional perovskites. The structure of $n = 1$ 2D perovskites generally consists of alternating organic and BX_6 inorganic layers with thicknesses of around 1 and 0.6 nm, respectively [93]. This distinctive quantum-well-like structure offers interesting and potentially useful chemical and physical properties. Taking the $n = 1$ case as an example, $(R\text{-NH}_3)_2\text{BX}_4$ and $(\text{NH}_3\text{-}R\text{-NH}_3)\text{BX}_4$ can be obtained when using monoamine and diamine molecules as the organic spacers, respectively, where R is an aliphatic or aromatic chain/group [7]. In the $(R\text{-NH}_3)_2\text{BX}_4$ series, single layers of inorganic (i.e. BX_6) sheets are separated by bilayers of organic cations, where the organic amine cation can form hydrogen bonds with the inorganic sheets on one side and the organic R group can self-assemble through van der Waals forces (e.g. aliphatic amine molecules like propylammonium [115], butylammonium [44, 116, 117] and 5-ammonium valeric acid [118]) and ‘ π - π ’ interactions (e.g. aromatic amine molecules like benzylamine [119], phenylethylammonium [120, 121], phenylbutylammonium [122], and naphthylmethylamine [123, 124]). The latter interactions tend to give the strongest packing, thus a more robust perovskite structure can be expected when using aromatic ammoniums. In the $(\text{NH}_3\text{-}R\text{-NH}_3)\text{BX}_4$ series, single layers of inorganic sheets are separated by single layers of organic diamine cations (e.g. 1, 3-propanediamine [20], 1, 4-bis(aminomethyl)benzene [125], and *meta*-(aminomethyl) piperidinium [126]), where the organic amine cations can form a hydrogen bond with inorganic sheets at both ends. The interactions between the ammonium functional groups (e.g. $R\text{-NH}_3^+$ or $^+\text{NH}_3\text{-}R\text{-NH}_3^+$ cations) and halogens in inorganic sheets build up the connective bridge between the ‘soft’ organic layers and ‘rigid’

inorganic layers. Consequently, their optical properties can be fine-tuned by the compositional engineering of the organic or inorganic parts at the molecular level. Besides the inorganic part mentioned previously, the organic cations can also be systematically modified by changing the chemical structure of the R group, which is a crucial factor that greatly influences the PLQY, bandgap and film morphology [21].

In 2D perovskite derivatives, the organic and inorganic (i.e. BX_6) components are very dissimilar in nature. Generally, the energy gap between the highest occupied molecular orbital (HOMO) and the lowest unoccupied molecular orbital (LUMO) of the organic layers is larger than the bandgap of the inorganic layer, establishing a quantum well structure [127]. The emission from 2D and quasi-2D systems typically originates from the inorganic part due to its smaller bandgap. Exceptions to this have been found when using semiconducting conjugated molecules with small bandgaps as the spacers, which turn the organic molecules into the emissive ‘well’ instead [128, 129]. The actual connective structure of the inorganic sheets including the bonding angles and lengths in BX_6 can also be affected by the choice of organic molecules and produce different optical properties [21]. For instance, changing the alkyl chain length of the R group not only affects the distance between organic and inorganic sheets and associated electronic coupling strength, but also alters the orientation of the organic and inorganic counterparts that govern the structural stability [130]. If the projection of the cross-sectional area of the organic molecule can fit into the space provided by four adjacent corner-sharing octahedra, the structure will be able to accommodate the lattice discrepancy by tilting or interdigitating the organic molecules. However, if the space required for the organic molecule is not satisfied, the perovskite structure is not able to spontaneously adapt, leading to the deformation of the inorganic sheets. Therefore, the projection of the cross-sectional area of the organic molecules should be neither too small nor too large with respect to the inorganic sheet lattice [131].

As previously mentioned, organic molecules also play an important role in the synthesis and size-control of perovskite nanoparticles including QDs and NCs [132]. The amine functional groups can coordinate with the surface of the perovskite to prevent the direct crystallization of precursors into large crystals during the antisolvent mixing procedure. Oleic acid can also modulate the size of the synthesized particles, and moreover can suppress the reaggregation of the products. By controlling the number of ligands in the precursor solution, MAPbBr_3 NCs with sizes between 3 and 35 nm can be obtained, and those with crystal sizes smaller than 10 nm (on the order of the exciton Bohr radius) exhibit conspicuous blue-shifted PL spectra (emission peaks of 470 nm for 3 nm-NCs and 515 nm for 35 nm-NCs) [132]. The chain length of the ligands also plays a critical role in optimizing the optoelectronic properties of the perovskite QDs and NCs. For example, it has been shown that gradually increasing the ligand hydrophobicity through the number of carbon atoms in the main chain can result in blue shifts from 531 to 510 nm by reducing the lateral size and increasing the interparticle distance between hybrid

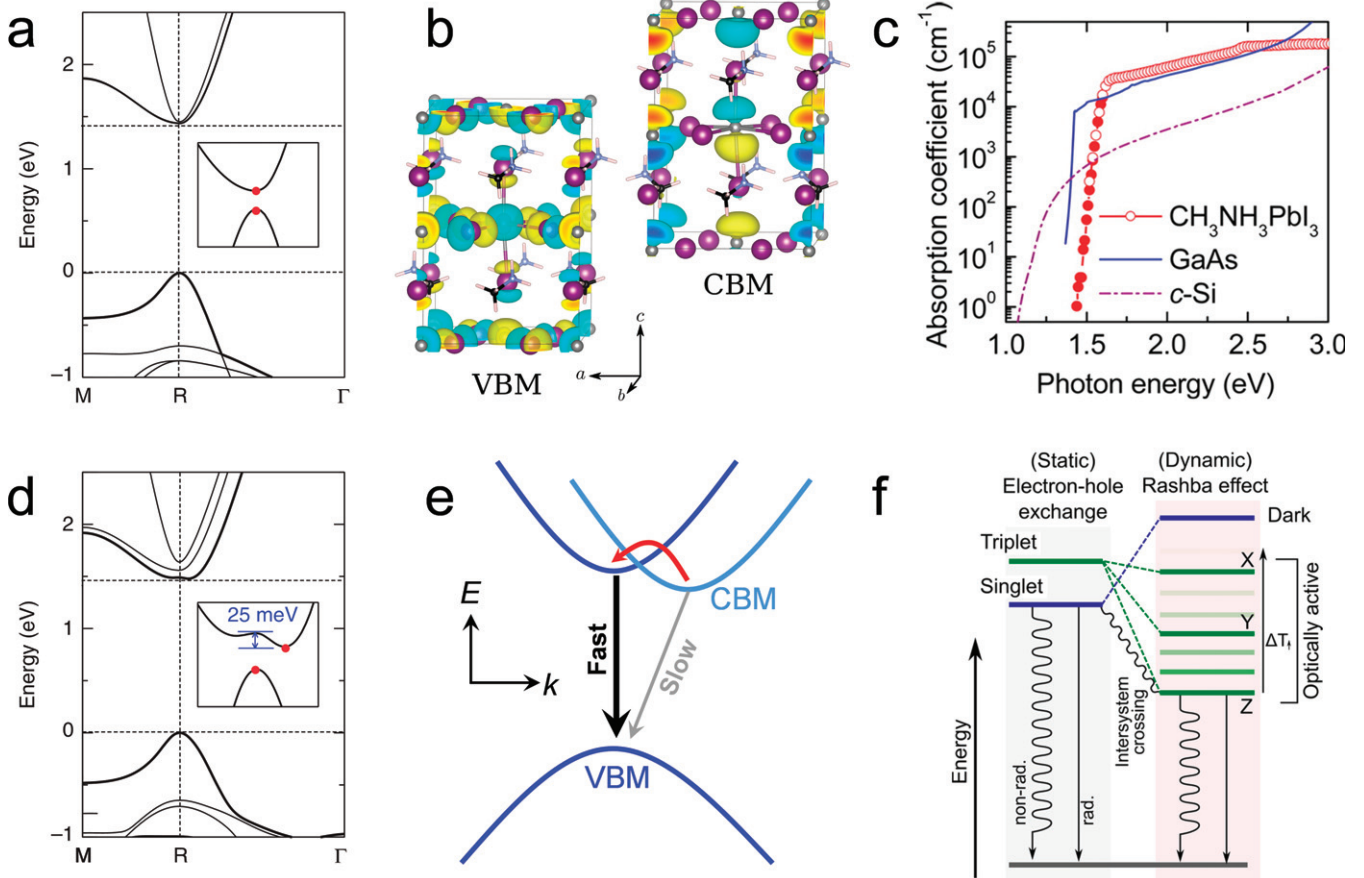


Figure 8. (a) Electronic band structure of MAPbI₃ obtained by DFT. Details of the calculation can be found in reference [137]. (b) Wave function plots for the VBM and CBM in MAPbI₃. (c) Absorption spectra for MAPbI₃, GaAs and crystalline silicon. (d) DFT-derived electronic band structure for MAPbI₃ with SOC and symmetry-breaking induced by the MA cation rotation. (e) Scheme for temperature-activated recombination in MHPs. (f) Proposed ordering of bright and dark excitonic states in MHP NCs. The Rashba effect results in triplet emission. (a), (d) Reprinted by permission from Springer Nature Customer Service Centre GmbH: Nature Communications [137] © 2015. (b) Reprinted with permission from [138]. Copyright (2015) American Chemical Society. (c) Reprinted with permission from [140]. Copyright (2014) American Chemical Society. (e) Reprinted by permission from Springer Nature Customer Service Centre GmbH: Nature Materials [146] © 2017. (f) Reprinted with permission from [155]. Copyright (2019) American Chemical Society.

perovskite NCs [133]. Similar trends have been reported for other material systems [134, 135] and the opposite result has also been observed [136].

2. Photophysics of metal halide perovskites

As illustrated in the ‘materials’ section of the review, the rich palette of available dimensions and compositions for MHPs means that their optoelectronic properties are widely tunable. Here we correlate the optoelectronic properties pertinent to PeLEDs with the characteristics of the electronically excited states that mediate light emission and then succinctly discuss the key materials factors which govern these fundamental photophysics.

2.1. Excited states in metal halide perovskites

2.1.1. Electronic band structure and optical transitions. Before ruminating on the details of light–matter interactions in different MHPs, it is instructive to consider the electronic band structure of these materials. Figure 8(a) shows

a representative electronic band structure calculated for the benchmark bulk MHP MAPbI₃ [137]. In spite of the organic cation, the bands wholly arise from the inorganic sublattice; as discussed previously, the conduction band is almost entirely composed of the outermost *p*-orbital on the metal (lead), while the valence band arises from an admixture of the frontier metal (lead) and halide (iodide) *s*- and *p*-orbitals, respectively [87]. Real space wave function plots for these molecular orbitals are shown in figure 8(b) [138]. Their strong antibonding character engenders small effective masses for the charge carriers in MHPs, which is reflected by the high curvature of the bands in figure 8(a) [139]. The effect of both the MHP composition and dimensionality on the band energetics are covered in prior section of this review. In the absence of structural distortions, the VBM and CBM coincide in momentum space at the high-symmetry R -point of the first Brillouin zone. This enables direct optical transitions between the bands, which largely explains the step-like onset of the absorption spectra for many MHPs, as depicted for MAPbI₃ in figure 8(c) [140]. For comparison, the absorption spectra

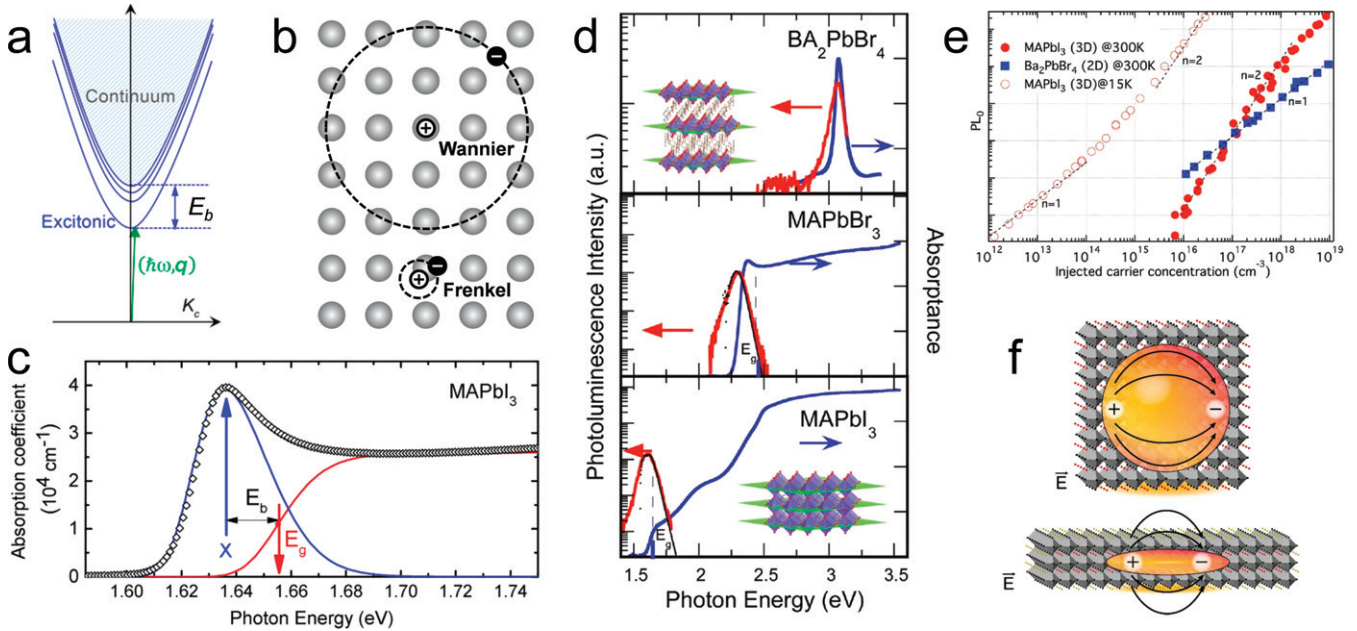


Figure 9. (a) $E-k$ diagram for excitons and the free carrier continuum in a semiconductor. E_b : binding energy for the lowest-energy exciton. (b) Wannier (top) and Frenkel (bottom) excitons. (c) Linear absorption data (black diamonds) for a MAPbI₃ thin film at 4 K. The fits from Elliot theory reveal the contributions of the lowest bound exciton (blue line) and the free carrier continuum (red line). (d) Room-temperature optical spectra for three prototypical MHPs, with sketches of the corresponding 2D and 3D structures. The red, purple and green shading depict the lead atoms, their coordination octahedra and planes formed by these octahedra, respectively. (e) PL intensity for the MHPs in (d) recorded 50 ps after pulsed laser excitation. (f) Dielectric screening in bulk (top) and 2D (bottom) MHP crystals. (a) Reprinted with permission from [161]. Copyright (2018) American Chemical Society. (c) Reprinted with permission from [167]. Copyright (2018) American Chemical Society. (d), (e) Reproduced from [169] with permission of The Royal Society of Chemistry. (f) Reprinted with permission from [60]. Copyright (2017) American Chemical Society.

of GaAs (direct bandgap) and crystalline silicon (indirect bandgap) are also presented.

Notwithstanding the prominence of the absorption transitions above, the direct nature of the MHP bandgap continues to be hotly debated in the literature. This stems from the fact that the heavy atoms which make up MHPs give rise to strong spin-orbit coupling (SOC). This, in concert with the breaking of the unit cell inversion symmetry (via distortions from the ideal corner-sharing octahedra, due to either static crystalline disorder or dynamic fluctuations of the soft lattice), leads to a phenomenon by the name of ‘Rashba splitting’, wherein otherwise spin-degenerate bands are split into bands with opposing spin polarisation (i.e. up and down). Indeed, this splitting (particularly for the conduction band) is frequently observed when SOC effects are incorporated into band structure calculations of MHPs, as seen in figure 8(d) [141, 142]. The net displacement of the VBM and CBM in momentum space creates an indirect gap. This new gap, up to hundreds of meV below the direct optical gap, has been experimentally observed in MHPs by circularly polarised magnetooptical and photogalvanic measurements, as well as angle-resolved photoelectron spectroscopy [143–145].

The apparent direct–indirect character of MHPs has been used to rationalise the long lifetimes of their thermalized carriers. Hutter *et al* reported a temperature-activated acceleration of the second-order recombination kinetics, pointing towards the phonon-assisted (i.e. indirect) recombination process in

figure 8(e) [146]. Along the same vein, Wang *et al* showed that the application of hydrostatic pressure to these materials could enhance bimolecular recombination by reducing the Rashba splitting and energy offset between the direct and indirect bands [147]. On the contrary, studies which more explicitly track the radiative recombination kinetics show that they are hastened by increased temperature [148, 149], and that the most intense emission is produced from carriers which have fully cooled [150]. These observations, and the fact that the bimolecular recombination kinetics of the materials (rate constants on the order of $10^{-10} \text{ cm}^3 \text{ s}^{-1}$) match predictions from the direct absorption coefficients can only sensibly be explained by emission from a direct bandgap [148], which seems to preclude the Rashba effect from the luminescence mechanism of bulk 3D MHPs. However, this situation is ostensibly different for low-dimensional MHPs, where symmetry-breaking is exacerbated by the presence of additional material interfaces and structural anisotropy [151]. For instance, there is a growing consensus that the room-temperature emission of MHP NCs originates from triplet excitons [152–154]. Without the Rashba effect, these states would be optically inactive, as portrayed in figure 8(f) [155]. Emissive triplets have also been observed in 2D MHPs [156–160]. These triplets ought to be significant for electroluminescent devices, because spin statistics dictate that electrical excitation must produce three triplets for each singlet. The behaviour of these triplets in some MHPs will be discussed further later on.

2.1.2. Excitons and free carriers. The operation of an LED begins with the electrical injection of free carriers into a semiconductor active layer. These charges can then coalesce into electrostatically bound electron–hole (e–h) pairs, known as excitons, as depicted by the energy–momentum diagram in figure 9(a) [161]. The equilibrium population of free carriers and excitons is principally controlled by the exciton binding energy (E_b), which describes the extent of the e–h interaction as follows: $E_b = \frac{m}{2\hbar^2} \left(\frac{e^2}{4\pi\epsilon_0\epsilon_r} \right)^2 = R_H \frac{m}{m_0\epsilon_r^2}$, where m is the reduced effective mass of the charge carriers [$m = (\frac{1}{m_e} + \frac{1}{m_h})^{-1}$], ϵ_r is the relative dielectric permittivity, R_H (=13.6 eV) is the Rydberg constant (essentially the binding energy of the electron in the ground-state 1s orbital of the hydrogen atom) and m_0 is the rest mass of a free electron [162]. Excitons can be classified into two limiting cases according to E_b ; Wannier ('weakly-bound' or 'free') excitons; and Frenkel ('tightly-bound') excitons. The former species, portrayed at the top of figure 9(b), are generally found in inorganic semiconductors where the value of ϵ_r and associated screening of the Coulomb interaction are high, resulting in e–h pairs that encompass multiple atoms and readily delocalize throughout the crystal. By contrast, the latter species, illustrated at the bottom of figure 9(b), are highly localized, have much smaller Bohr radii commensurate with the unit cell size, and can typically be found in molecular and/or organic semiconductors with low ϵ_r .

In most MHPs, the ionicity of the crystal and orientational motion of the cations tend to produce moderate-to-large ϵ_r values and screen the Coulombic interaction of excitons [163]. In bulk MHPs, the small effective mass of the charge carriers ($\sim 0.1m_e$) also contribute to small E_b values (for example, 2 to 50 meV in the archetypal MAPbI₃, depending on the method of measurement and material processing) [164–166]. Generally, E_b values comparable to room temperature allow for Wannier excitons and free carriers to co-exist in MHPs, which manifests itself in the optical and electronic properties of the materials. In the specific case of MAPbI₃, excitonic features are only clearly observable under specific conditions [167], and free carriers are widely thought to dominate the ambient photophysics [165, 168]. This can be seen in figure 9 as (i) the disappearance of the strong exciton absorption (figure 9(c)) at room temperature (figure 9(d)), and (ii) the quadratic dependence of the PL intensity on the carrier density around the LED operating regime (room temperature and $< 10^{16} \text{ cm}^{-3}$, figure 9(e)), consistent with the bimolecular recombination of free carriers, which will be outlined later in the review [169]. While free carriers are highly desirable for carrying current in photovoltaic applications, excitons are preferable for light emission to increase the probability for carriers to undergo radiative recombination, and to prevent the charges from engaging in otherwise deleterious processes in the active layer. To this end, seminal works on PeLEDs overcame the small E_b of bulk MHPs by employing thin active layers and nanostructured materials to spatially confine injected carriers and encourage e–h radiative recombination [91].

Contemporary high-performance PeLED materials are based upon low-dimensional MHPs, where E_b is dramatically

enhanced via reduced Coulombic e–h screening through quantum and/or dielectric confinement [170–173]. The latter effect is depicted for a 2D MHP in figure 9(f); in essence, the electric field lines must pass through the low dielectric permittivity surroundings, thereby increasing the e–h electrostatic interaction with respect to the bulk crystal. If one considers the following relationship, $E_b = (\frac{2}{\alpha-1})^2 E_e$, where α is the semiconductor dimensionality and E_e is the effective Rydberg constant [174–176], a four-fold increase in E_b (i.e. $4E_e$) can be expected when moving from a 3D MHP ($\alpha = 3$) to its 2D counterpart ($\alpha = 2$). E_b values in the 200–500 meV range have been reported for 2D layered MHPs [177], in line with other emerging 2D semiconductors such as single-layer transition metal dichalcogenides [178] and CdSe nanoplatelets [179]. For the 2D MHPs, E_b can be tailored through the composition of the inorganic sheets, their spacing, as well as the type of interposing organic cation, allowing for highly versatile material design [21]. As illustrated in the top inset of figure 9(d), the alternating stacks of high dielectric ($\epsilon_r \sim 6$) BX₆ planes and small dielectric ($\epsilon_r \sim 2$) organic layers in 2D MHPs form self-organized quantum wells in the out-of-plane direction [170]. The excitons in these materials (Bohr radii of ~ 0.1 to 2 nm) can be strongly quantum confined within the sub-nm wells [170, 180, 181]. Consequently, the excitonic properties are extremely pronounced for 2D MHPs comprising single BX₆ layers. This is demonstrated by (i) the sharp, narrow features in the optical spectra and (ii) linear carrier density-dependence of the PL intensity from the 2D MHP BA₂PbBr₄ ($n = 1$, BA = butylammonium) in figure 9(e). In 2D MHPs like BA₂PbBr₄, large differences between the optical spectra of $n = 1, 2, 3$, and 4 samples are frequently observed ($\sim 6 \text{ \AA}$ thickness for single BX₆ layer), but often converge with the bulk properties when $n > 5$. Much larger Bohr radii have been reported for cuboidal MHP NCs (e.g. 5 nm for CsPbCl₃, 7 nm for CsPbBr₃, 12 nm for CsPbI₃) [67]. However, it remains difficult to widely modulate their emission spectra ($> 100 \text{ nm}$ spectrum shift) based on quantum confinement alone, and especially when aiming for stable, monodisperse perovskite QDs with sizes of a few nanometers.

2.1.3. Carrier–phonon coupling. The photophysics of semiconductors are not only governed by the coupling between electronic states, but also their interactions with disorder, impurities and vibrations (phonons) in the crystal. The extent to which these entities scatter with the (emissive) excited states can be examined through the temperature-dependence of the emission linewidth: $\Gamma(T) = \Gamma_0 + \Gamma_{\text{imp}} + \Gamma_{\text{ac}} + \Gamma_{\text{LO}}$ [182]. The inhomogeneous linewidth, Γ_0 , is set by the crystalline disorder and corresponds to the linewidth at absolute zero. The remaining terms have a characteristic temperature-dependence. The inhomogeneous broadening due to impurities, Γ_{imp} , is proportional to the Boltzmann population of fully ionized defects, $e^{-E_b/k_B T}$ (k_B : Boltzmann constant; T : absolute temperature), with binding energy E_b . Γ_{ac} and Γ_{LO} are the homogenous broadening terms by acoustic and optical phonons, respectively, and thus depend on the phonon occupation, given by the Bose–Einstein distribution, $1/(e^{-E_{\text{ph}}/k_B T} - 1)$. Since acoustic phonons in inorganic

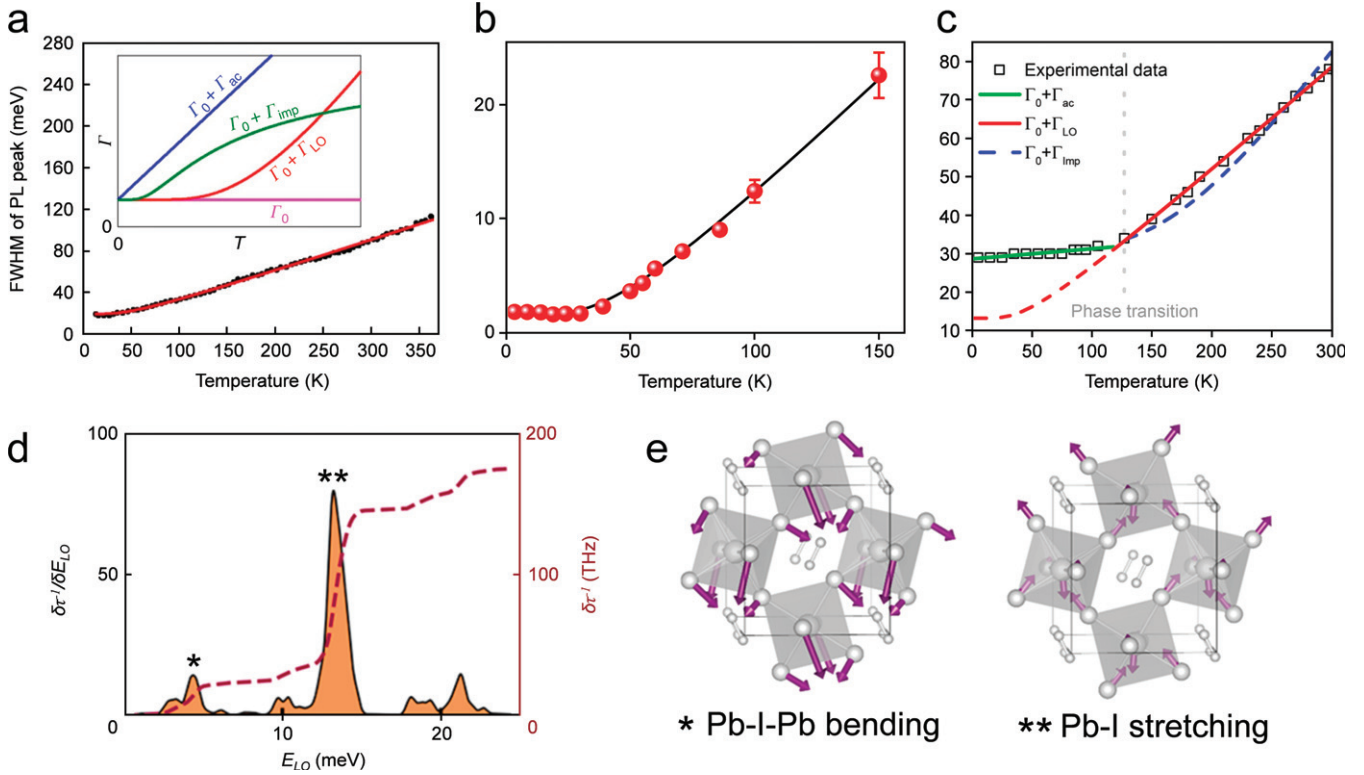


Figure 10. Temperature dependence of the PL linewidth from (a) bulk FAPbI₃ thin film, (b) single-NC FAPbI₃ and (c) thin film of the 2D layered MHP ($n = 1$) hexylammonium lead-iodide. The inset of (a) outlines the functional form of each term in the equation for $\Gamma(T)$ described in the text above. (d) Contribution of phonons (left axis) towards the total carrier scattering rate (right axis) in MAPbI₃. (e) Atomic displacements corresponding to the major carrier scattering modes in MAPbI₃. (a) Reprinted by permission from Springer Nature Customer Service Centre GmbH: Nature Communications [182] © 2016. (b) Reprinted by permission from Springer Nature Customer Service Centre GmbH: Nature Communications [185] © 2018. (c) Reprinted with permission from [186]. Copyright (2017) American Chemical Society. (d), (e) Reprinted with permission from [187]. Copyright (2019) American Chemical Society.

semiconductors (and for that matter MHPs) seldom have energies of more than a few meV ($E_{\text{ph}} \ll k_{\text{B}}T$) [183, 184], a linear relation between Γ_{ac} and temperature can be assumed.

The conformity of the data in figures 10(a)–(c) with the Γ_{LO} functional form highlights that the room-temperature emission linewidths of bulk and low-dimensional MHPs are dominated by carrier scattering with longitudinal optical (LO) phonons [182, 185, 186]. The results of separate theoretical works, including figure 10(d) [187], affirm that the scattering rate is dominated by low-energy LO phonons ($E_{\text{LO}} < k_{\text{B}}T$; contrary to many conventional optoelectronic semiconductors) [188] which correspond to atomic displacements in the metal halide cage, depicted in figure 10(e). These thermal structural fluctuations have large amplitudes according to Raman spectroscopy [189–191] as well as neutron [192] and electron diffraction [193], underscoring the soft and highly anharmonic nature of the MHP lattice. A large body of work suggests that this picture of ‘dynamic disorder’ is further enriched by the vibrational motions of the A-site cations [194, 195], but the extent to which this influences the optoelectronic properties of MHPs remains unsettled in the literature [196, 197], and goes well beyond the scope of this review.

According to Fröhlich theory, the strength of carrier–LO phonon interactions can be quantified by a dimensionless constant, $\alpha = \frac{e^2}{\hbar} \left(\frac{1}{\epsilon_{\infty}} - \frac{1}{\epsilon_s} \right) \sqrt{\frac{m_{\text{e,h}}^2}{2E_{\text{LO}}}}$, where $m_{\text{e,h}}$ is the bare-band effective mass of the carrier and ϵ_{∞} and ϵ_s are the optical and static (infrared) dielectric constants. Together with their moderate-to-high dielectric screening, the small E_{LO} and $m_{\text{e,h}}$ values of MHPs give rise to fairly high coupling strengths ($1 < \alpha < 3$) [198, 199]. In this regime, the carriers can be envisaged to self-trap inside a potential well formed by the aforementioned displacements of the lattice. These so-called ‘polaron’ states generally have slightly enhanced effective masses compared to bare carriers, and in this particular context have a large spatial extent (diameter on the order of 10 nm for MAPbI₃ [198–201], corresponding to ~ 20 [PbI₆]⁴⁻ octahedra) owing to the long-range nature of the carrier–phonon interactions. The existence of these large polarons has obvious implications for charge transport, discussed below, and is also thought to contribute to many other unusual photophysical properties in MHPs, including defect tolerance [202], slowed carrier cooling [203–205], and slowed recombination [201].

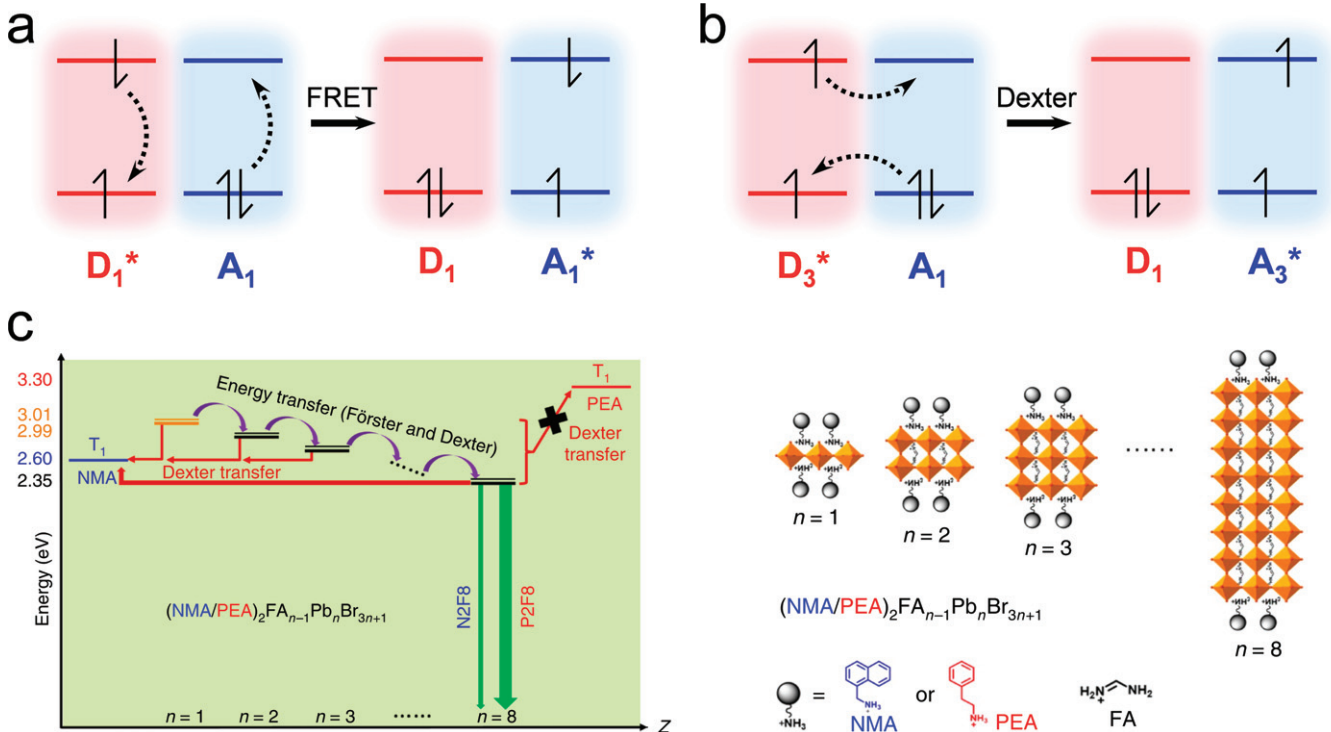


Figure 11. Sketches of (a) singlet exciton hopping via FRET and (b) triplet exciton hopping via Dexter energy transfer. (c) Proposed energy transfer mechanisms in PeLEDs based on the quasi-2D MHPs $(\text{NMA}/\text{PEA})_2\text{FA}_{n-1}\text{Pb}_n\text{Br}_{3n+1}$ (N2F8) and $(\text{PEA})_2\text{FA}_{n-1}\text{Pb}_n\text{Br}_{3n+1}$ (P2F8), where NMA is 1-naphthylmethylamine and PEA is phenylethylammonium; unit cell and molecular structures on the right-hand side. For both systems, excitons are funnelled to the higher-dimensional grains via FRET and Dexter processes. In the case of N2F8, the low-lying triplet on NMA quenches the PeLED emission via Dexter transfer. By contrast, the triplet state of PEA is too high in energy to engage in Dexter transfer, and therefore does not interfere with the strong emission from P2F8. (c) Reprinted by permission from Springer Nature Customer Service Centre GmbH: Nature Photonics [157] © 2020.

2.2. Energy/charge transport in metal halide perovskites

Now that we have familiarized the reader with the electronically excited states in MHPs, we can describe how these states propagate towards the emission sites in the active layer of a PeLED. At the most basic level, this involves the net transduction of *energy* in the form of electrically-insulating bound e–h pairs (excitons) or *charge* in the form of uncorrelated free carriers. As will become apparent below, these processes and their interplay depend on the energetic landscape of the MHP material in question.

2.2.1. Energy transport. Förster resonance energy transfer (FRET) is perhaps the most widely known type of electronic energy transport in photoactive materials. Here an excitation is transmitted from an energy-donating site to an energy-accepting site via a virtual photon. This process, sketched in figure 11(a), is mediated by the coupling between the transition dipoles of the two sites. Accordingly, FRET cannot occur if either of the D or A transitions are classically forbidden (no triplets) and also has a marked dependence on the D–A separation (R) as follows: $k_{\text{Förster}} = \frac{1}{\tau_D} \left(\frac{R_0}{R} \right)^6$, where τ_D is the fluorescence lifetime of the donor in the absence of the acceptor, and R_0 is the characteristic Förster distance at which FRET occurs with 50% efficiency. Although FRET is non-radiative, R_0 depends on the extent of spectral overlap between

the donor emission and acceptor absorption, as well as the mutual orientation of the transition dipoles [206].

The trivial Stokes shift shown by many MHPs makes them conducive to FRET. The strong distance dependence generally limits FRET to 1–10 nm, making it a viable route for singlet exciton transfer between MHP nanomaterials, especially where there is size dispersity to drive the excitations to the lowest energy site in the ensemble [207–209]. To this end, ultrafast FRET has been exploited in numerous PeLEDs based on mixed MHP colloidal quantum wells (CQWs, see section 3 for examples). FRET ought to be rapid in these systems because of the reduced distance dependence (R^{-4}) from the extended 2D dipole interaction, and the propensity of the wells (and thus their transition dipoles) to align parallel to each other [209].

If the D–A separation is sufficiently small (≤ 1 nm), their D and A electronic wave functions can overlap and engage in charge transfer. This opens the possibility for the excited state to migrate via the coordinated exchange of a conduction electron from the donor and valence electron from the acceptor, as shown in figure 11(b). This is known as Dexter energy transfer, and exhibits the following rate constant: $k_{\text{Dexter}} \sim J \sigma e^{-R}$, where J , σ and R represent the aforementioned orbital overlap, spectral overlap and separation between the donor and acceptor [210]. Unlike Förster theory, triplet transfer is not forbidden in the Dexter mechanism. Ergo, for LEDs based

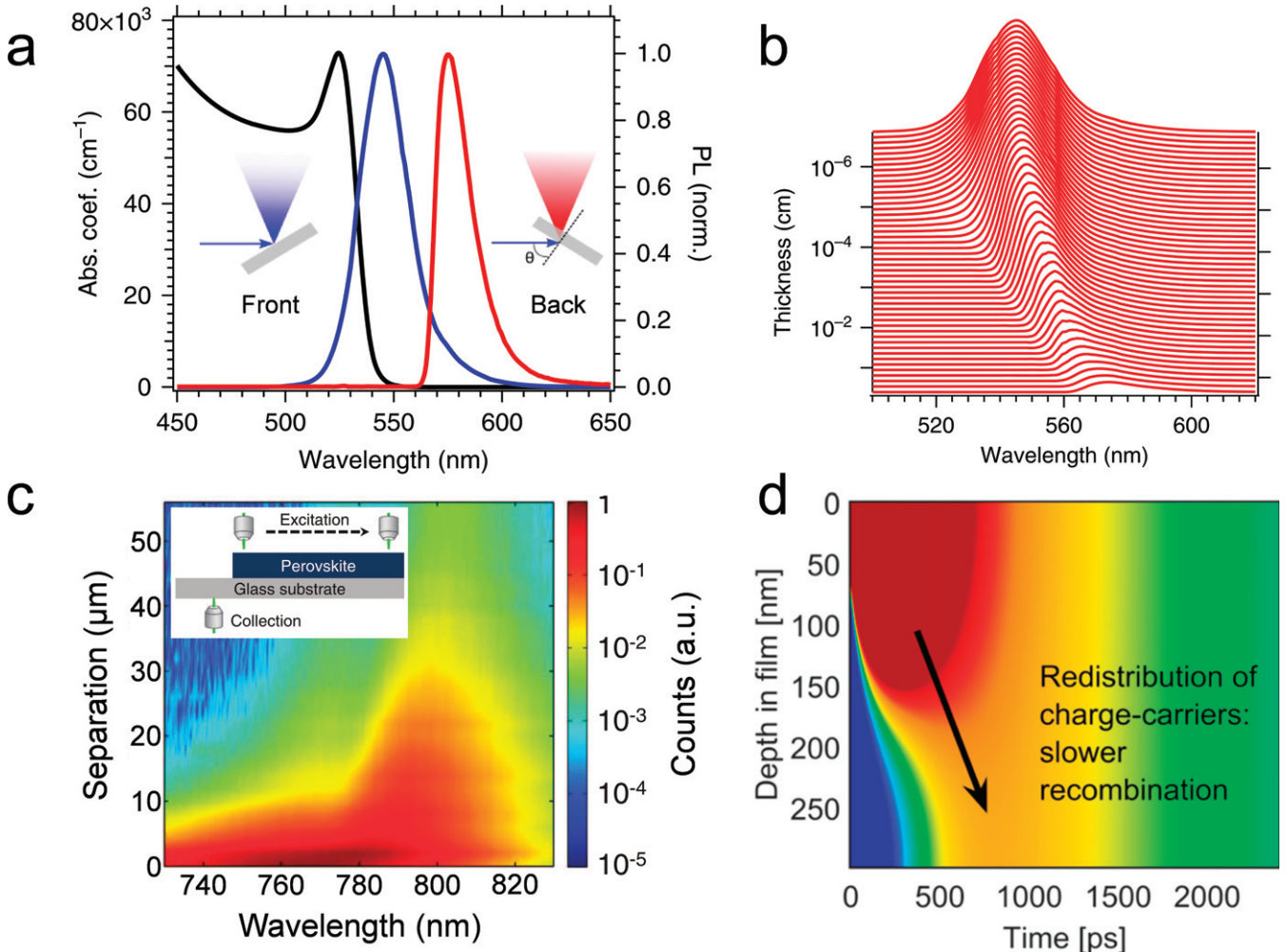


Figure 12. (a) Absorption (black) and PL spectra collected from the front (blue) and rear (red) of a 2.13 mm thick MAPbBr_3 single crystal. (b) Calculated shift of the PL emission through the MAPbBr_3 single crystal due to photon recycling. (c) Pseudocolour map comprising the PL spectra of a MAPbI_3 polycrystalline thin film recorded at different distances between excitation and collection (represented in the inset). (d) Modelled charge carrier dynamics within a 300 nm thick MAPbI_3 polycrystalline film following photoexcitation at 400 nm ($44 \mu\text{J cm}^{-2}$). (a), (b) Reprinted by permission from Springer Nature Customer Service Centre GmbH: Nature Communications [213] © 2017. (c) From [217]. Reprinted with permission from AAAS. (d) Reprinted with permission from [218]. Copyright (2017) American Chemical Society.

on excitonic semiconductors (organic LEDs (OLEDs) being the prime example) [211], the majority of the electrical excitations are transported on the short-range by Dexter transfer. Figure 11(c) highlights the importance of the Dexter mechanism in a quasi-2D MHP LED conceived by the Adachi group. Here, Dexter transfer is used to corral triplet (and singlet) excitons to high-dimensionality grains, but also mediates emission quenching by organic moieties with low triplet energies [157].

The Förster and Dexter mechanisms above are fundamentally non-radiative in nature. However, the high absorption coefficients, luminescence quantum yields and small Stokes shift of MHPs mean that energy can also be shuttled through a PeLED active layer via the iterative emission and reabsorption of (real, not just virtual) photons. This form of radiative energy transport is known as ‘photon recycling’, and is known to occur in other high-quality semiconductors with the aforementioned optical properties, such as GaAs [212]. Figure 12(a) encapsulates a hallmark of photon recycling in a (thick) single crystal

of MAPbBr_3 . The PL originating from the excited face of the sample substantially overlaps with the absorption spectrum, thus enabling efficient reabsorption of the PL. As the emitted light propagates through the sample, the band-tail emission (redder light) is reabsorbed and reemitted more effectively, which biases the rear-collected PL spectrum to lower energies. Figure 12(b) shows that this spectral filtering can be modelled from the Beer–Lambert law, and accordingly exhibits a dependence on the sample thickness [213].

Beside the front and back-illumination experiments, photon recycling has been observed in other MHPs by a variety of spectroscopic methods, including comparison of the reflected and transmitted PL spectra, differentiation of the emitted and reabsorbed photons by polarisation, comparison of surface and bulk emission by two-photon excitation, and spatially-resolved measurements where the PL is collected from the sample at a defined lateral distance from the excitation [214–217]. The results of the latter experiments, as represented by figure 12(c),

are particularly salient because they directly demonstrate that photon recycling occurs over considerable distances (exceeding microns). In these works, complementary charge extraction and EL measurements further support the notion of long-range e–h transport [216, 217]. This redistribution of the excited states within the sample has been shown to decelerate recombination kinetics by reducing the local carrier density, as shown in figure 12(d) [218]. Because photon recycling is interrelated with the propagation of light through the material, various photonic structures have been devised to exploit photon recycling in PeLEDs, and are deliberated in section 3.7.

2.2.2. Charge transport. The energy transport mechanisms above govern the migration of preformed e–h pairs through MHPs. In a working PeLED, these emissive e–h pairs originate from electrically-injected free electrons and holes, and thus charge transport must precede recombination and light emission. The motion of a carrier through a semiconductor can be described in terms of diffusion with a characteristic length scale, $L = \sqrt{\tau D}$ where τ is the carrier lifetime (time taken to recombine, or inverse of the recombination rate, see section 2.3), and D is the diffusion coefficient. In MHPs, carrier diffusion lengths on the order of microns have been elucidated (an order of magnitude beyond the typical PeLED active layer thickness) [219–221]. This is quite outstanding for multi-component materials that are fabricated by solution-processing techniques [222–224].

According to the Einstein relation $D = \frac{\mu k_b T}{q}$, D is controlled by the carrier mobility, μ . This is a material-dependent parameter which expresses the velocity of a carrier when pulled through the semiconductor by an electric field, and can be determined by a variety of methods, including PL quenching [219, 220], space-charge limited current, Hall coefficient and resistivity measurements, time-of-flight transients [221, 225], and field-effect-transistor mobility [226]. Non-contact methods based on short laser pulses, such as time-resolved microwave conductivity and optical pump-terahertz probe are exceedingly popular because they do not require any explicit modification of the thin film samples, and also relay direct information on the dynamics of the charge carriers, which will be discussed in section 2.3 [148, 227, 228].

The intrinsic mobility of a semiconductor can be understood within the simplified framework of Drude theory, which treats the constituent nuclei (or ions) as immobile within a ‘sea’ of unbound charge carriers. In this way, only the carrier properties have to be modelled as follows, $\mu = \frac{e\tau^*}{m_{e/h}}$, where τ^* is the average scattering time, and $m_{e/h}$ is the effective mass of the electron or hole. Although there is a considerable spread in the reported values, the majority of measurements give values below $100 \text{ cm}^2 \text{ V}^{-1} \text{ s}^{-1}$ for the epitomic bulk polycrystalline MHPs [222]. Given that $m_{e/h}$ in these systems is $\sim 0.1 m_e$, it follows that τ^* must be tens of fs. This rapid scattering, and the anticorrelation between μ and temperature suggest that the intrinsic carrier mobility of MHPs is limited by phonons rather than by defects; other polar semiconductors behave in this same regard [229]. The $T^{-1.5}$ dependence observed

in many MHPs circumstantially points towards scattering by acoustic or non-polar optical phonons [228, 230], at odds with the results of the temperature-dependent PL linewidth studies and the wider Fröhlich mechanism for carrier–LO phonon scattering, for which $\mu \propto T^{-0.5}$ is to be expected. This discrepancy has been attributed to a number of peculiarities, including lattice anharmonicity and a temperature-dependence of the dielectric properties [222].

Other factors that exacerbate the scattering of charge carriers and introduce variations in mobility include impurities, defects, grain boundaries, and energetic disorder [222]. Hence, even for a given stoichiometry of MHP composition, the reported charge carrier mobility values can be quite different due to various processing conditions which affect material crystallinity and average domain sizes. The anisotropic nature of 2D MHPs brings another degree of complexity to their charge transport properties. While the in-plane mobilities of these materials are comparable to their bulk counterparts, the off-plane mobilities are substantially hindered by the ligand interlayers and dielectric confinement [231].

As a final remark on charge transport, we note that electrical charge can also be carried by mobile ions in MHPs. The ionicity and softness of the ABX_3 lattice lends itself to the spontaneous dissociation of the A, B and X ions; particularly in the latter case of halide dissociation where activation energies below 0.6 eV have been reported [232, 233]. The charged species produced by illumination, thermal or electrical stress can diffuse through the MHP solid (usually via grain boundaries) [234] and contribute significantly to the total electrical conductivity of the materials. For example, direct-current galvanostatic polarisation and alternating-current impedance measurements indicate that the ionic conductivity can exceed the electronic conductivity in iodide-based MHPs [235–237]. This accumulation of ionic charge is proposed to be the main culprit for hysteresis in MHP photovoltaics [238–240], and is also attributed to the long-term operational instability of MHP optoelectronic devices. One can also posit issues for balanced charge injection in PeLEDs, which are outlined later in this review. Mixed-halide systems are especially vulnerable to changes in their optical and electrical behaviour from halide migration, since phase segregation can result in additional cascades for the aforementioned energy and charge transport processes [241]. Examples where these cascades have been deliberately engineered in PeLEDs also feature in the device section of this review.

2.3. Radiative and non-radiative decay mechanisms in MHPs

In an optimal LED, the electrically-injected excited states recombine to produce photons (light) rather than phonons (heat in the lattice). With this in mind, the following parts of the review survey the basic mechanisms of radiative and non-radiative e–h recombination in semiconductors, as well as their relevance to different MHP materials. We will then emphasise some of the unique luminescent properties of MHPs with a view on their application to PeLEDs.

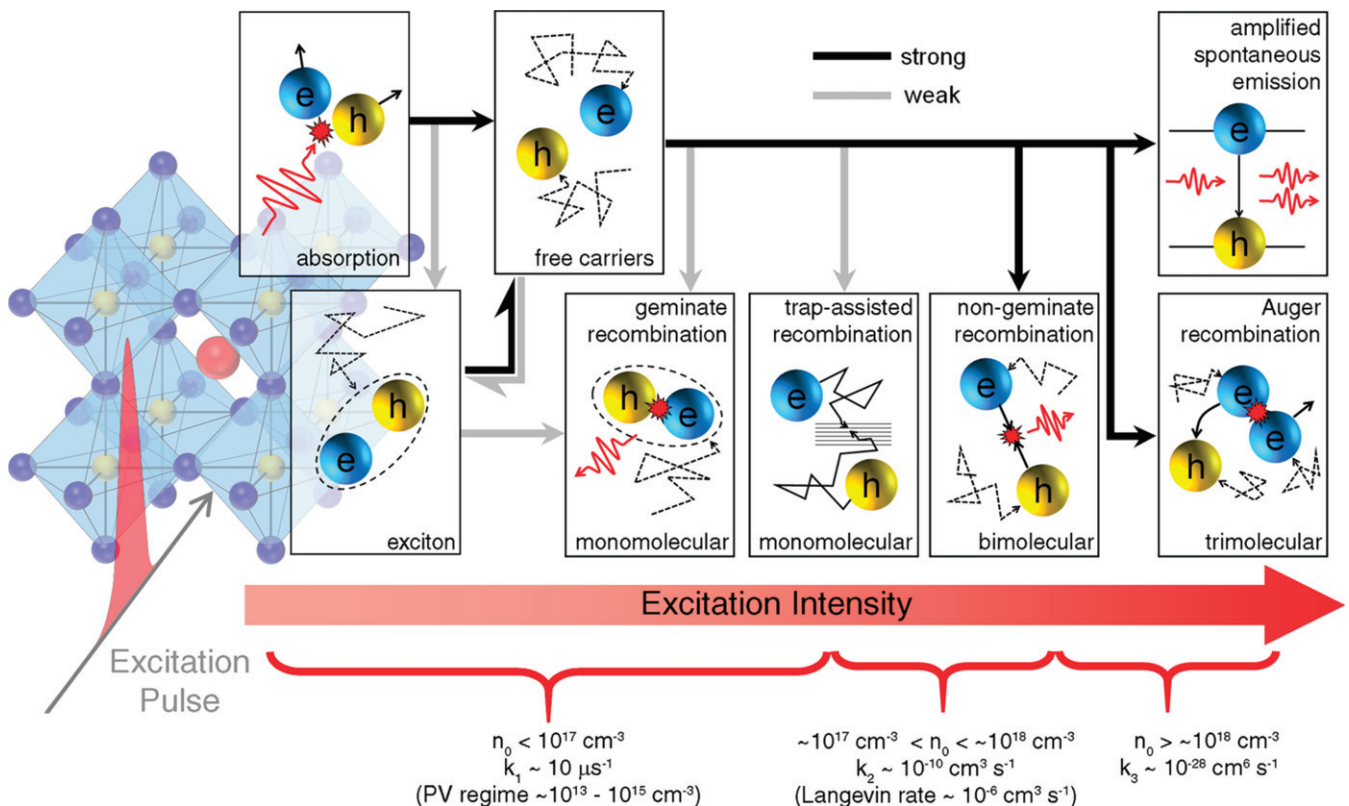


Figure 13. Mechanisms for e–h recombination in MHPs following pulsed photoexcitation. Reprinted with permission from [243]. Copyright (2016) American Chemical Society.

2.3.1. e–h recombination. The excited state dynamics, and particularly recombination kinetics of MHPs ultimately determine the emission properties of PeLEDs, and have been thoroughly studied over the past decade using a variety of time-resolved spectroscopies. Generally speaking, the kinetics obtained from these measurements can be fit to the following global equation: $-\frac{\delta N(t)}{\delta t} = k_1 N + k_2 N^2 + k_3 N^3$, where N is the charge carrier density, and k_1 , k_2 and k_3 are mono-, bi- and tri-molecular rate constants [164, 242]. For MHPs where the exciton binding energy is high ($E_b \gg k_B T$, such as NCs and single-layered MHPs), the overall recombination kinetics (and PL intensity, as shown above in figure 9(e)) tend to be first-order with respect to N , with the dominant $k_1 N$ term corresponding to the direct annihilation of the e–h pairs; known as geminate recombination. Significant deviations from this linear behaviour only occur when exciton–exciton interactions start to play a role. In the other scenario where E_b is low, (comparable to room temperature, as in most polycrystalline bulk samples), the recombination kinetics are somewhat more complicated because they are interrelated with the motion of individual free charges, as depicted in figure 13 [243].

For these non-excitonic MHPs, the $k_1 N$ term is also significant for small excitation densities (up to 10^{16} cm^{-3}), but is non-radiative in nature, and therefore attributed to trap-assisted (Shockley–Read–Hall) recombination of the free carriers, whereby an electron (or hole) recombines with its partner in a defect state. The lifetime of this process is remarkably long ($\sim 10^{-5} \text{ s}$) in spite of the relative

abundance of trap states ($\sim 10^{15}–10^{17} \text{ cm}^{-3}$) when compared with other highly luminescent semiconductors such as GaAs (trap density $\sim 10^{13}–10^{15} \text{ cm}^{-3}$) [244]. Non-radiative recombination is also prevalent at extreme excitation conditions due to Auger recombination, where electrons and holes recombine and non-radiatively donate their energy to other charge carriers. This three-particle (and hence trimolecular) process is only relevant at $N \gg 10^{15} \text{ cm}^{-3}$, and therefore has more important implications for lasers than LEDs, owing to its competition with stimulated emission. The strongest spontaneous emission is obtained at intermediate excitation densities ($10^{16}–10^{17} \text{ cm}^{-3}$), where all the traps are filled but Auger processes are negligible. The fact that both the recombination kinetics and PL intensity (also in figure 9(e)) have a quadratic dependence on N in this regime indicates that radiative recombination from these materials is a non-geminate and bimolecular process, depending on the population of both electrons and holes. The determined values of k_2 ($\sim 10^{-10} \text{ cm}^{-3} \text{ s}^{-1}$) are several orders of magnitude above the rate constants predicted by Langevin theory, as portrayed by the exceptionally low ratio of k_2 to the charge carrier mobility ($\sim 10 \text{ cm}^2 \text{ V}^{-1} \text{ s}^{-1}$) [227]. This manifests itself in the long carrier diffusion lengths, as discussed in the previous section. Unlike k_1 , the values of k_2 are intrinsic for a given MHP composition. Maximizing the luminescence efficiency of PeLEDs therefore involves (i) the amelioration of trap-assisted recombination; (ii) attaining excitation densities that are conducive to bimolecular recombination by, for example, spatially confining the carriers; and (iii),

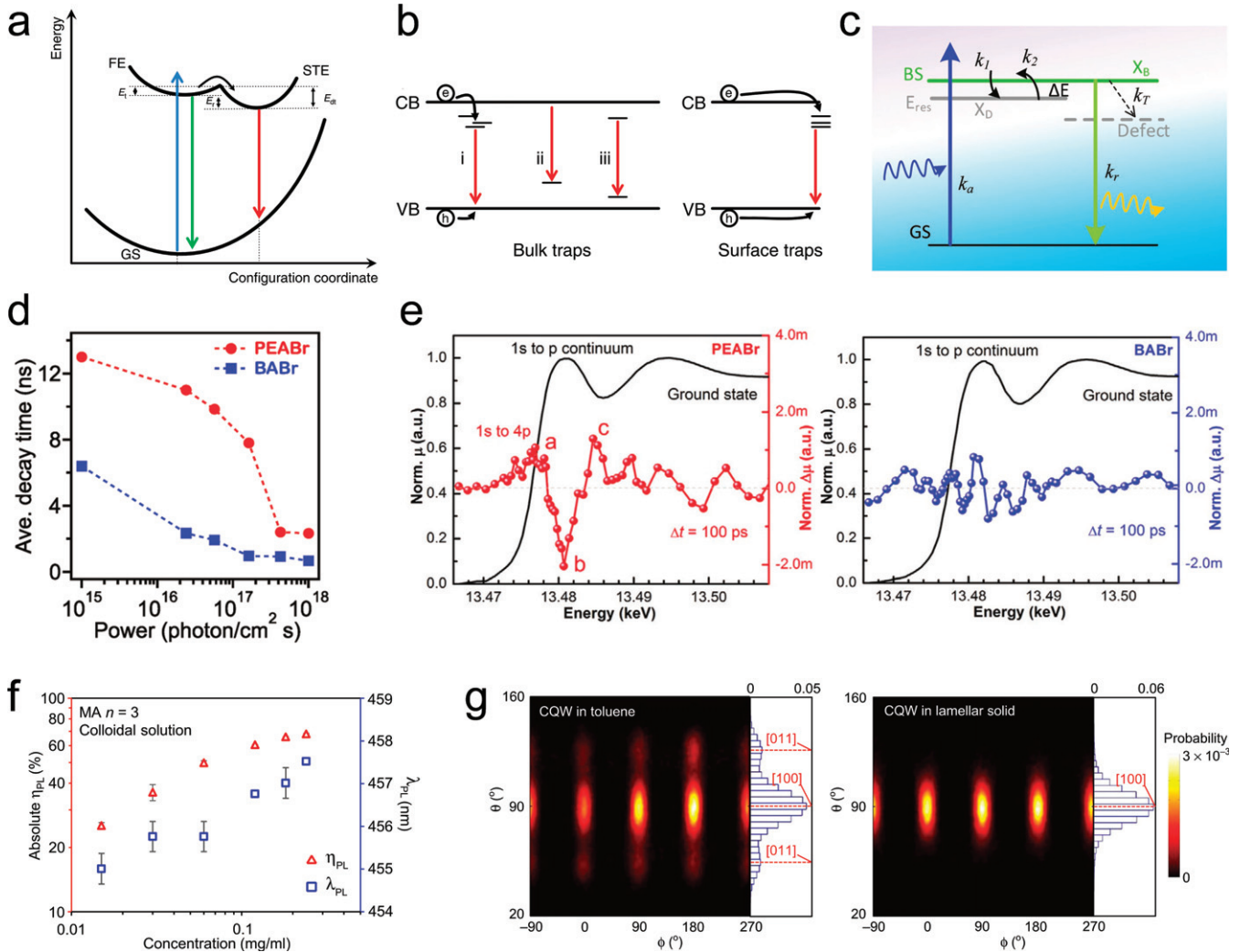


Figure 14. Schematic diagrams of emission from STE (a) and through trap states (b). (c) Schematic of energy relaxation and radiative recombination of a simplified model. GS: ground state, BS: bright excited state, E_{res} : energy reservoir, X_B : bright exciton, and X_D : dark exciton. (d) Average PL decay times of PEA- and BA-based samples as a function of the incident laser power. (e) The ground state x-ray absorption spectra versus energy and the change in x-ray absorption after 100 ps delay for PEA- and BA-based films. (f) Absolute PLQY values and emission wavelength peaks as a function of CQW concentration. (g) Orientational distribution contour maps of surface MA cations in toluene solution and lamellar solid state. (a), (b) Reprinted by permission from Springer Nature Customer Service Centre GmbH: Nature Communications [250] © 2020. (c) [251] John Wiley & Sons. © 2019 WILEY-VCH Verlag GmbH & Co. KGaA, Weinheim. (d), (e) Reproduced from [252]. CC BY 4.0. (f), (g) Reproduced from [261]. CC BY 4.0.

along this same vein, encouraging excitonic recombination by enhancing the exciton binding energy. These approaches will be elaborated in section 3 of this review.

2.4. Tailoring the PL properties of perovskites

The rich photochemistry of MHP materials discussed above offers many opportunities for controlling and engineering their electroluminescent properties through the material composition, molecular and electronic structure, density of states and dimensionality.

Historically, the most important material factor imposing upon the lighting properties of semiconductors are lattice defects. Generally, defects that are weakly coupled to the lattice result in only small shifts between the ground and excited state potential energy surfaces, which lends itself to a broad emission spectrum (for example in ZnO) [245, 246].

Alternatively, defects that strongly couple to lattice distortions can produce more substantial shifts between the ground and excited state energy surfaces that suppress luminescence by inducing non-radiative (multi-phonon) transitions, culminating in an intrinsic and narrow emission spectrum of the semiconductor [247]. For MHP materials, narrow emission spectra with FWHM less than 20 nm are generally observed, which suggests that the latter of the above scenario is most relevant. Interestingly, some reports show that a broad emission spectrum can be achieved by forming self-trapped excitons (STE, as shown in figure 14(a)) in 3D and 2D MHPs, yielding intrinsic white light emission [248, 249]. However, a recent report on $n = 1$ 2D perovskites of PEA_2PbI_4 and $\text{FPEA}_2\text{PbI}_4$ shows that the broad emission spectrum can also result from

the in-gap trap states, as shown in figure 14(b), providing the first evidence for radiative trap-assisted recombination in the perovskite family [250].

In addition to the interband phenomena above, the luminescence properties of semiconductors are also influenced by the intraband density of states, as well as optically inactive (dark) states residing close to the band edges. The latter states have been posited to act as a transient energy reservoir in some MHPs, for example in the 2D MHP BA_2PbI_4 , where the internal PLQY ($\sim 70\%$) and time-resolved PLQY ($\sim 17\%$) are highly incongruent [251]. This is explained by figure 14(c), which shows that optically-generated bright excitons rapidly relax to the lower dark states rather than non-radiatively recombining through a defect state, leading to a sharp decay of the initial TRPL signal. Nevertheless, the small energy gap between the bright and dark states allows the thermally-activated excitons to radiatively recombine and give a high PLQY. The exact nature of the dark states is still unclear, but they are likely to be spin-forbidden triplet states in 2D BA_2PbI_4 perovskite, as discussed previously for other MHP materials [152, 156].

Organic spacers and ligands, particularly in low-dimensional systems, offer an additional means of controlling the emissive properties of materials. The organic spacers butylamine (BA) and phenylethylamine (PEA), which consist of an alkyl chain and a benzyl ring, respectively, have been systematically studied with regards to the PL properties of RP-phase 2D MHPs [252]. In figure 14(d), it can be seen that the TRPL decay is twice as slow in $\text{PEA}_2\text{MA}_2\text{Pb}_3\text{Br}_{10}$ than in $\text{BA}_2\text{MA}_2\text{Pb}_3\text{Br}_{10}$ for a wide range of given excitation powers (ranging from 10^{15} to 10^{18} photon $\text{cm}^{-2} \text{s}^{-1}$). The PLQY value of the latter film is also 7.4 times lower, pointing towards a stronger non-radiative decay channel. To investigate this behaviour on the atomistic level, time-resolved x-ray absorption spectroscopy (TR-XAS) was used to measure the electronic structure dynamics after photoexcitation. Figure 14(e) shows the intense x-ray absorption edge peak around 13.48 keV, corresponding to the $1s$ to p continuum transition of Br. For the PEA-based material, the transient signal persists beyond 100 ps, pointing towards relatively long-lived photogenerated holes localized on the Br atoms. By contrast, these holes have already recombined in the BA-based analogue. The origins of this behaviour could be related to steric, delocalisation or carrier–phonon coupling effects caused by the organic spacers, and while not yet conclusively understood, clearly demonstrate the importance of these spacers towards charge recombination.

Finally, it is essential to note the role of charge and energy transport management in optimising the luminescence properties of disordered polycrystalline materials. For instance, MHP NCs usually exhibit very high PLQYs in the solution state (over 70%), but upon aggregation (and forming crystalline solids such as in thin films), a huge loss of PLQY is observed, which is widely known as the quantum yield quenching effect [97, 253–256]. This undesirable effect can be attributed to efficient exciton diffusion through FRET towards quenching sites within the size-inhomogeneous quantum wells [257]. Two types of quenching site are commonly recognized:

defect-mediated mid-gap states due to the dangling bonds on the nanomaterial surface, or charged particles produced through many-body Auger processes [258, 259]. Surprisingly, in the case of $(\text{C}_8\text{H}_{17}\text{NH}_3)_2[\text{MAPbBr}_3]_n\text{PbBr}_4$ CQWs, Jagielski *et al* reported that the PLQY values in lamellar solids were higher than those in solution states except for the $n = 1$ sample, which exhibited aggregation-induced emission (AIE) behaviour [260, 261]. The AIE effect was corroborated by an increase of the PLQY with increasing concentration of the colloidal solution (figure 14(f)). Classical molecular dynamics simulations were then conducted to investigate the orientational distribution of surface MA cations in the $n = 3$ sample. Figure 14(g) illustrates that surface MA cations of CQWs dispersed in toluene orient within the surface plane, particularly along two preferable orientations of $\langle 100 \rangle$ and $\langle 011 \rangle$. While in a lamellar solid-state, the motion of surface MA cations are more restricted within the surface plane and only along the $\langle 100 \rangle$ direction, making the adjacent surface ligands interpenetrate with each other and interact with the surface MA cations. The restriction of the molecular orientation relieves the bandgap variation induced by different orientational configurations, and consequently triggers the AIE phenomena. This unique phenomenon of avoiding self-quenching upon aggregation merits further study as it is expected to enable high-performance PeLEDs.

3. Device engineering of PeLEDs

3.1. PeLED device structures and fabrication techniques of perovskite films

As with the antecedent OLEDs and quantum dot LEDs (QLEDs), PeLEDs are typically thin-film devices that adopt one of two general structures: conventional and inverted. These terms generally refer to ‘n-i-p structure’ and ‘p-i-n structure’ in the perovskite optoelectronic field, respectively, and are represented alongside energy diagrams [91, 262] in figure 15. As shown in figure 15(a), for a conventional structure, the transparent conductive oxide layer (in this case indium tin oxide (ITO)) sits above the glass substrate to work as a cathode that injects electrons into the CBM/LUMO of the electron transport layer (ETL), and then to the CBM of the perovskite emitter. At the same time, holes are injected from the highly-reflective metal anode to the VBM/HOMO of the hole transport layer (HTL), and then to the VBM of the perovskite emitter. The injected electrons and holes may then undergo radiative recombination (bimolecular for free carriers, monomolecular for excitons). For an efficient device, the ETL should have a deep VBM/HOMO to effectively block the injected holes, and the HTL should have a shallow CBM/LUMO to effectively block the injected electrons, thus confining the injected electrons and holes to the perovskite emitter. For an inverted structure, shown in figure 15(b), the electron/holes are injected in opposite directions from that above. Here, the ITO layer works as an anode to inject holes into the VBM/HOMO of the HTL and then into the VBM of perovskite emitter. At the same time, electrons are injected from the metal cathode to the CBM/LUMO of the ETL, and then into the CBM

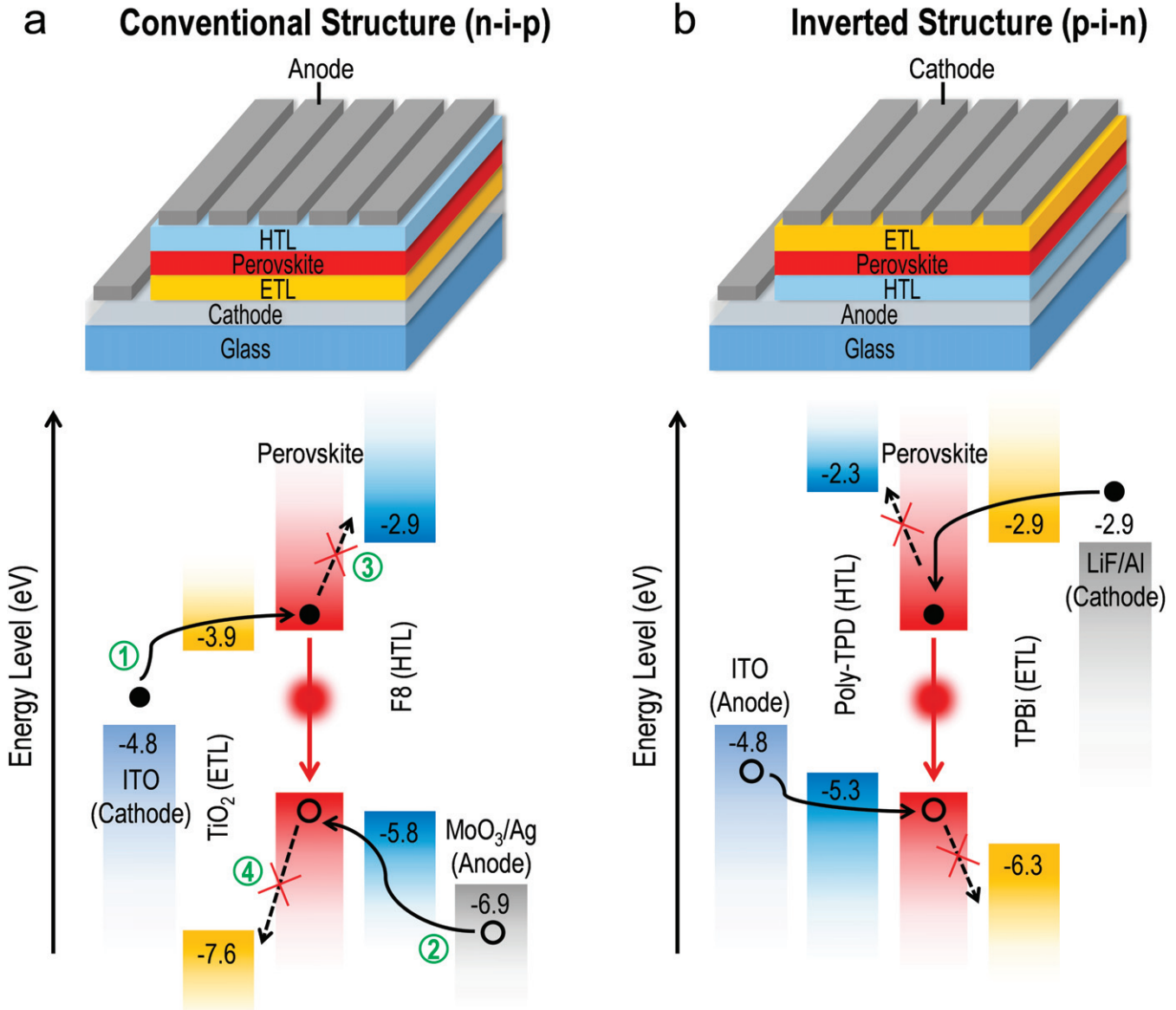


Figure 15. Conventional (n-i-p) structure (a) and inverted (p-i-n) structure (b) of PeLEDs. The respective energy diagrams of two representative systems are also shown. The green numbers indicate the roles of the different layers: (1) electron injection; (2) hole injection; (3) electron blocking and (4) hole blocking.

of the perovskite emitter. Similarly, the ETL (HTL) should have deep VBM/HOMO (shallow CBM/LUMO) to effectively block the injected holes (electrons) so that electrons and holes can efficiently radiatively recombine within the perovskite emitter.

Due to the excellent processability of perovskite materials in both solution and solid phases, numerous techniques have been adopted to fabricate perovskite films. Here we discuss spin coating, blade coating, inkjet printing, and thermal evaporation. Spin coating is by far the most popular for PeLED fabrication because of its high reproducibility and compatibility with the anti-solvent dripping process [263]. In spin coating, the solvent of the precursor solution rapidly evaporates and immediately nucleates the perovskite crystals. Because different circumferential speeds are generated

along the radial direction of the sample during spin coating, the perovskite crystal growth generally varies in the centre and edge of the sample and can result in non-uniform films [264]. The slower solvent evaporation in techniques such as blade coating is therefore desirable for large area samples, and considerable efforts are underway to understand and control the growth of perovskite crystals under these conditions. To the best of our knowledge, only one report to date has successfully demonstrated PeLEDs based on blade coating [265]. The nucleation-and-growth issue can be circumvented through inkjet printing while using perovskite QDs/NCs as inks, making it more useful for fabricating patterned films and high-resolution displays, but the microscopic morphology can sometimes disrupt the formation of a smooth, continuous film and lead to ‘coffee ring’ aberrations [266]. Although

the aforementioned solution-processing techniques are powerful, they are limited by the requirement for HTL/ETL substrates with suitable hydrophilic–hydrophobic characteristics. Thermal evaporation nullifies the substrate effect by directly evaporating the perovskite precursors onto the HTL/ETL substrate, extending the choice of charge transport materials. The composition, dimension, and uniformity of active films can also be modulated by varying the precursors, co-evaporation process, substrate heating, etc, as can be seen in modern commercial OLED fabrication [267–270].

3.2. EQEs of PeLEDs

EQE is defined as the ratio of the number of photons that escape the device to the number of charges injected into the device. Obviously, it is an efficiency parameter related to the optical and electrical properties of a PeLED. The following four aspects must be addressed to maximize the EQE of a PeLED: (i) do electrons and holes reach the perovskite emitter simultaneously to avoid their recombination in other layers (requires excellent e–h balance)? (ii) Does every injected electron and hole form an e–h pair/exciton in the perovskite emitter (requires no parasitic losses of electrons and holes)? (iii) Does every e–h pair/exciton experience radiative recombination to emit a photon (requires high EL quantum yield)? (iv) Does every photon successfully escape the device and propagate to the far field (requires excellent light out-coupling)? Accordingly, we can use the following equation to describe the EQE of a PeLED:

$$\text{EQE} = B_{\text{e-h}} \times L_{\text{e-h}} \times \text{ELQY} \times \text{LEE}$$

where $B_{\text{e-h}}$ represents the balance between injected electrons and holes in a perovskite emitter, which can be modulated by interfacial engineering in the PeLED. $L_{\text{e-h}}$ represents the parasitic loss of electrons and holes in a PeLED, such as leakage current and traps in ETL and HTL layers, which corresponds to the overall PeLED quality. ELQY represents the EL quantum yield of e–h pair/excitons, which is generally assumed to be equal to the PLQY value of perovskite thin film in the PeLED field. On this point, it is important to state several factors which distinguish the ELQY and PLQY values: [271] (i) a constant 1:1 e–h ratio is generated in the light-driven PL process, while a potential charge imbalance occurs in the electrically-driven EL process; (ii) in electrical injection, charge carriers tend to transport through perovskite components with lower energy states (i.e. the parts with lower electrical resistances), while in photoexcitation, all perovskite components can be excited simultaneously (this difference is highly pronounced in quasi-2D perovskites); (iii) other material-related factors, such as the final ratio of singlet and triplet excitons under electrical injection and photoexcitation, because the photon emission from triplet states to the ground state is normally forbidden. Lastly, LEE represents the light extraction efficiency of photons generated in the device, which relates to the refractive index of each layer and geometry of the PeLED. In the best-case scenario, all four parameters (i.e. $B_{\text{e-h}}$, $L_{\text{e-h}}$, ELQY, and LEE) have unity values and therefore the EQE of the PeLED is 100%.

3.3. Development history of PeLEDs

PeLEDs originated in the 1990s, and we summarise the important developments in the EL properties of perovskite layers from 1992 to 2014 in figure 16. In 1992, Hong *et al* provided the first demonstration of EL emission from a $(\text{C}_6\text{H}_5\text{C}_2\text{H}_4\text{NH}_3)_2(\text{CH}_3\text{NH}_3)\text{Pb}_2\text{I}_7$ perovskite at 77 K [272]. However, the birth of PeLED is often attributed to Era *et al* in 1994, who, for the first time, used a $(\text{C}_6\text{H}_5\text{C}_2\text{H}_4\text{NH}_3)_2\text{PbI}_4$ perovskite as a green-emitting layer in a thin-film LED structure which exhibited a high luminance of $10\,000\text{ cd m}^{-2}$ at 77 K [273]. This report also indicated the use of organic hole/electron buffer layers to confine the injected charge carriers within the emissive perovskite layer. In 1996, Hattori *et al* modulated the organic ligands of 2D perovskites to form $(\text{C}_6\text{H}_9\text{C}_2\text{H}_4\text{NH}_3)_2\text{PbI}_4$ and $(\text{C}_6\text{H}_5\text{C}_4\text{H}_8\text{NH}_3)_2\text{PbI}_4$, which obtained a much higher PLQY than that of previously reported $(\text{C}_6\text{H}_5\text{C}_2\text{H}_4\text{NH}_3)_2\text{PbI}_4$ perovskites. Based on these emissive layers, the best device obtained a high EQE of 2.8% at 110 K, showcasing ligand modulation as another important strategy for improving device performance [274]. Although these reports represent significant milestones in engineering the EL of perovskite materials, none of the devices above presented emission at room temperature; an issue that remained unsolved for almost two decades [275, 276]. The two main reasons for this were that, firstly, high-quality perovskite films and PeLED fabrication techniques were still undeveloped at that time, and secondly, the PeLED studies mainly focussed on $n = 1$ or 2 perovskites as the emissive layers, which suffered from severe thermal quenching of excitons in the perovskite films at room temperature [170, 277]. Compared with the prosperous development of OLEDs and QLEDs, the inferior device efficiencies at room temperature and the nearly stagnant development of the PeLED field attracted little interest from the research community between 1994 to 2013. However, in this period of time, several attempts were made to realize room-temperature-emissive PeLEDs. For instance, in 1999, to avoid the thermal quenching of exciton in BX_6 sheets at room temperature, Chondroudis *et al* designed a 2D perovskite of $(\text{H}_3\text{NC}_2\text{H}_4\text{C}_{16}\text{H}_8\text{S}_4\text{C}_2\text{H}_4\text{NH}_3)\text{PbCl}_4$, which generated light from the small-bandgap organic ligands rather than the large-bandgap BX_6 sheets, and the resulting PeLED yielded an efficiency of 0.1 lm W^{-1} at room-temperature [278]. Later, in 2011, Koutselas *et al* demonstrated the first room-temperature-emissive PeLEDs with naked-eye EL from the BX_6 sheets, based on the 2D perovskites of $(\text{CH}_3(\text{CH}_2)_7\text{CH} = \text{CH}(\text{CH}_2)_8\text{NH}_3)_2\text{PbX}_4$ ($X = \text{I}, \text{Cl}, \text{Br}$). The simple device structure of ITO/perovskite/Ga–In provided solid evidence that all the EL came from the perovskite layer. However, no device properties such as EQE and luminance were reported with this research [279]. In 2014, Schmidt *et al* successfully synthesised $\text{CH}_3\text{NH}_3\text{PbBr}_3$ QDs and demonstrated the first perovskite QLED with room-temperature emission and reported luminance of $\sim 0.45\text{ cd m}^{-2}$, but the EQE was also not shown [62]. A few months later, Tan *et al* published a comprehensive study on room-temperature PeLEDs based on a

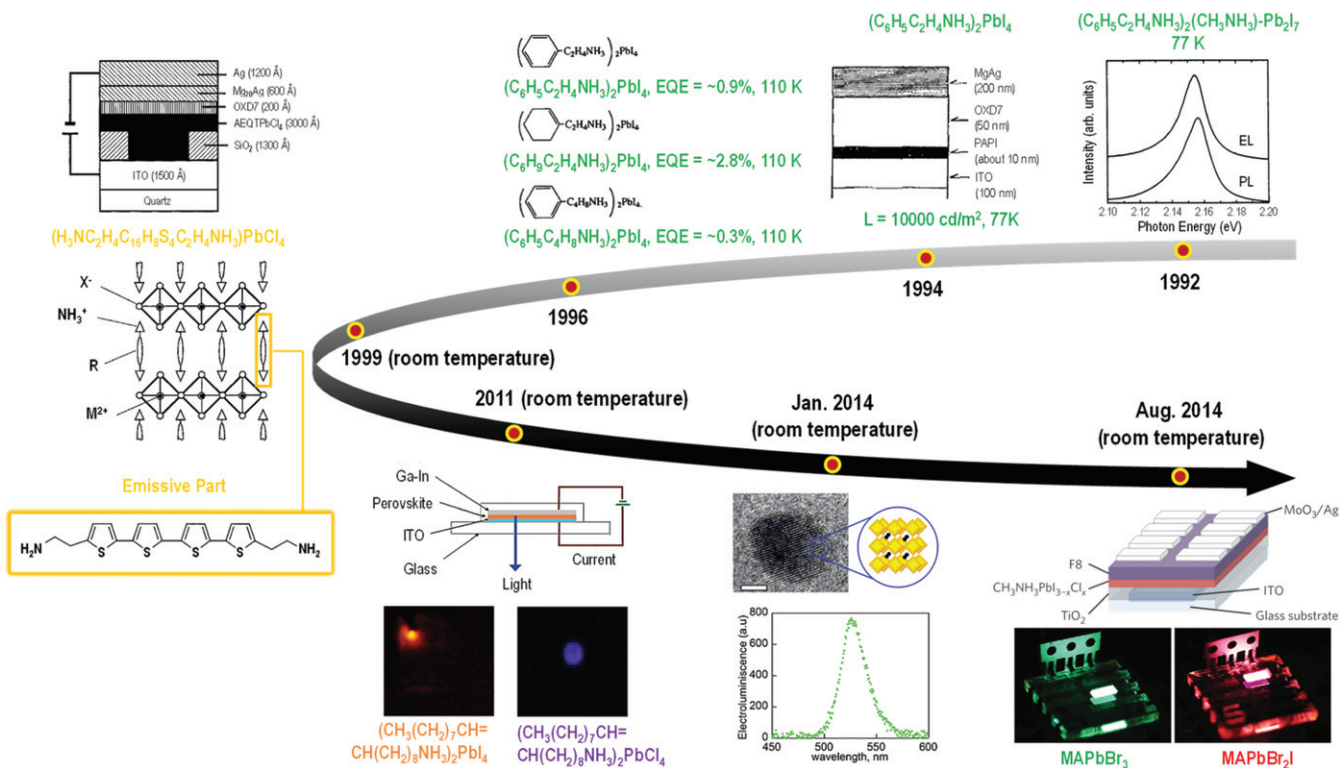


Figure 16. Important developments in the EL properties of perovskite layers from 1992 to 2014. Reprinted from [272], Copyright (1992), with permission from Elsevier. Reprinted from [273], with the permission of AIP Publishing. Reprinted from [274], Copyright (1996), with permission from Elsevier. Reprinted with permission from [278]. Copyright (1999) American Chemical Society. Reprinted with permission from [279]. Copyright (2011) American Chemical Society. Reprinted with permission from [62]. Copyright (2014) American Chemical Society. Reprinted by permission from Springer Nature Customer Service Centre GmbH: *Nature Nanotechnology* [91] © 2014.

ITO/poly(3, 4-ethylenedioxythiophene):poly(styrene sulfonate) (PEDOT:PSS)/perovskite/poly(9,9'-dioctylfluorene) (F8)/Ca/Ag device structure. The infrared-emitting devices presented a decent EQE of 0.76% and radiance of $13.2 \text{ sr}^{-1} \text{ m}^{-2}$, respectively, while the green- and red-emitting devices presented EQEs of 0.1% and 0.018%, with luminance values of 364 and 16.2 cd m^{-2} , respectively [91]. This research was especially encouraging to the field as it showed the great potential of perovskite materials for LED applications. Since 2014, the development of PeLED has continued to skyrocket.

Since 2014, many important concepts and strategies inspired from the OLED, QLED, and perovskite photovoltaic fields were used for the advancement of PeLEDs. This is summarised in the PeLED performance chart in figure 17.

In 2015, Wang *et al* modified the ZnO/perovskite interface by inserting a thin polyethylenimine layer, which provided a hydrophilic surface for perovskite growth and a low work-function cathode for Ohmic contact [280]. Decent EQEs of 3.5% and 0.8% were achieved in their near-infrared and green PeLEDs, respectively, signalling the importance of interfacial engineering for PeLEDs. Later, the first demonstration of perovskite QLEDs with multiple colours from orange to blue was presented by Song *et al*, bolstering the prospect of zero-dimensional perovskites for LEDs [281]. Along this vein, Cho *et al* subsequently used smaller perovskite crystals to enhance the excitonic nature of the materials and yield a high-performance green PeLED (EQE = 8.53%) [40].

In 2016, quasi-2D perovskites combining the advantages of 2D and 3D perovskites took centre stage in the literature. Yuan *et al* demonstrated an energy funnel concept for quasi-2D PeLEDs based on the transfer of charge carriers from small-*n* 2D perovskite grains to large-*n* 2D perovskite grains to improve the overall radiative properties of quasi-2D perovskite films, resulting in an efficient near-infrared PeLED with 8.8% EQE [282]. Later, Wang *et al* found a similar funnel process in a quasi-2D MQW with a vertical distribution of various dimensional perovskites. A high EQE of 11.7% was successfully achieved in their best near-infrared PeLED [283].

In 2017, the performances of near-infrared, red, green, and blue PeLEDs based on the aforementioned strategies were enhanced even further [33, 284–286], and substantial progress of PeLEDs with various colours followed in subsequent years.

In 2018, Lin *et al* demonstrated a quasi-core/shell structure of 3D CsPbBr₃/MABr crystals where MABr efficiently passivated the surface traps of the CsPbBr₃ crystals to promote the EQE of the green PeLEDs beyond 20%, underlining the importance of trap passivation for perovskite crystals [287]. Light-extraction was another figure of merit showcased in this year; Cao *et al* found that a self-light-extraction effect was produced through the formation of submicrometre-scale perovskite crystals, which promoted the EQE of near-infrared PeLED to over 20% [288]. For red PeLEDs, perovskite QDs played an important role in achieving high-performance devices. Lu *et al*

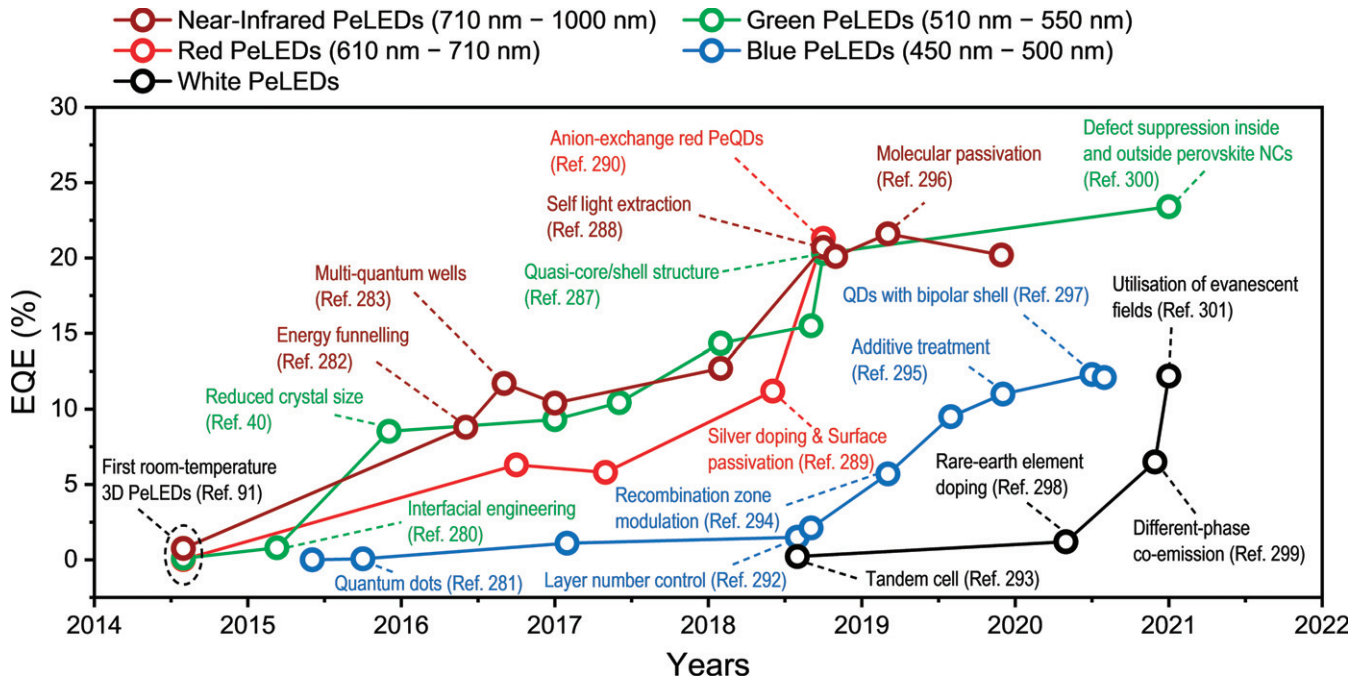


Figure 17. PeLED efficiency chart (without out-coupling lens), highlighting important concepts and strategies.

reported a doping effect arising from diffusion from the silver electrode in a top-illuminated device. This passivated the CsPbI_3 surface and promoted the PeLED EQE to 11.2% [289]. Chiba *et al* pushed the EQE of red PeLEDs above 20% by employing an anion-exchange strategy with perovskite QDs [290]. At this stage, the performance of blue PeLEDs severely lagged behind, although continuous efforts had been made to develop these devices [281, 285, 291]. Xing *et al* demonstrated a concept using two different organic ligands in quasi-2D perovskites to modulate the dominant layer number and associated emission properties, however, a relatively low EQE of 1.5% was recorded from the device [292]. After thorough investigations of white-light PL from perovskite thin films [248, 249, 254], Mao *et al* demonstrated the first white all-perovskite LEDs composed of red and blue-emitting perovskites inside a tandem structure, however the 0.22% EQE still left a lot to be desired [293].

By 2019, near-infrared, red, and green PeLEDs began to converge with their theoretical performance limits, and great efforts to develop blue PeLEDs were still underway. Li *et al* discovered that for a vertical non-uniform distribution of quasi-2D perovskite crystals in a thin film, the majority of perovskite crystals tended to disperse on the top. By modulating the e-h recombination zone position in the active layer they achieved a breakthrough for blue PeLEDs with the champion EQE of 5.7% [294]. Wang *et al* were able to further improve the PLQY of blue perovskite films by introducing a wide-bandgap YCl_3 additive, which accumulated at grain boundaries to confine charge carriers to the perovskite crystals, leading to better radiative recombination and a more efficient blue PeLED (EQE of 11%) [295]. Additives also played a role in the development of highly-efficient near-infrared PeLEDs with record EQE of 21.6%. Here, Xu *et al* rationally designed

a set of oxygen-containing small molecules to modulate the hydrogen bonding between the passivating functional moieties and the organic cation in the perovskite [296].

In 2020, a further step was made for blue and white PeLEDs. Dong *et al* successfully synthesized blue perovskite QDs with a bipolar shell consisting of an inner shell made from anions and an outer shell comprised of cations and polar solvent molecules. This improved the carrier mobility and reduced trap density of perovskite QDs, which contributed to the best blue PeLED to date (EQE = 12.3%) [297]. In addition, a single-component white PeLED was successfully demonstrated via the doping of rare-earth element Sm^{3+} in CsPbCl_3 nanoparticles. An EQE of 1.2% and luminance of 938 cd m^{-2} have been reported for this device [298]. Later on, further development of single-layer white PeLEDs was achieved via broadband emission from a perovskite/non-perovskite heterophase, which contributed to an EQE of 6.5% and peak luminance of 12 200 cd m^{-2} [299].

In early 2021, two key breakthroughs have come to the fore of the PeLED field: (i) the most efficient PeLED to date (with 23.4% EQE) based on green-emitting perovskite QDs with their inner and surface traps passivated through guanidinium doping and a halide vacancy healing agent [300]; (ii) the most efficient white PeLED to date (with 12.2% EQE) by extracting trapped optical modes through near-field optical coupling between the blue and red perovskite layers in the device [301].

The concepts and strategies summarised in figure 17 and reported in [33, 40, 91, 120, 121, 254, 280–307] have made a great contribution to the step-by-step development of PeLEDs. Below, we further categorise them according to their improvements to specific EQE parameters: B_{e-h} , L_{e-h} , ELQY (or PLQY in general) and LEE.

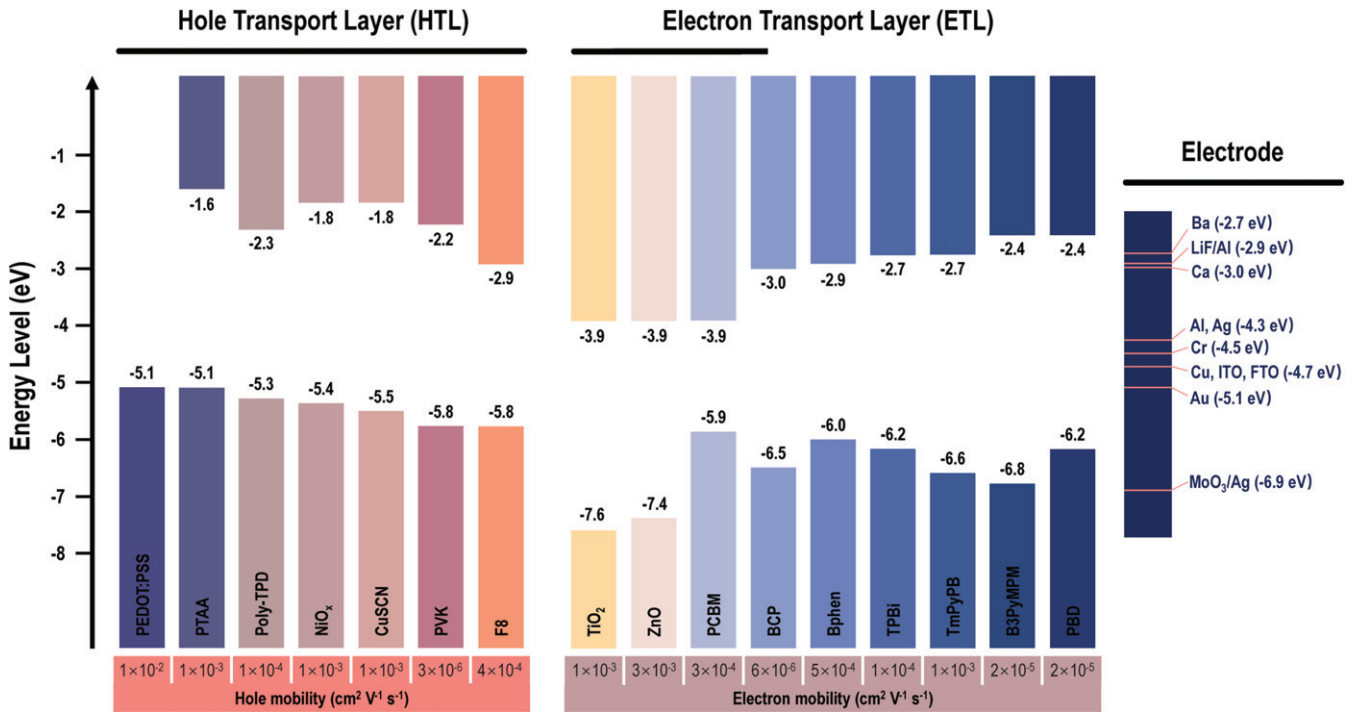


Figure 18. Summary of energy levels and electron/hole mobilities of widely-used ETLs and HTLs for PeLEDs.

3.4. B_{e-h} improvement

3.4.1. Interfacial engineering. As mentioned in the ‘charge transport’ part in section 2.2, various methods are deployed for electron/hole mobility measurements. When using the same measurement method, the electron and hole mobilities of perovskites tend to be highly similar [219, 220, 308], which can be attributed to the comparable m_e and m_h [90, 309]. Therefore, perovskites can be considered as bipolar (intrinsic) semiconductors with balanced electron and hole transport. In this case, the e–h balance in a PeLED mainly depends on the ease with which electrons and holes are injected from the electrodes into the perovskite layer, and how fast these charges can travel in the ETL and HTL, respectively. By modulating the energy levels and charge transport properties of the ETL and HTL, it is possible to make electrons and holes reach the perovskite layer simultaneously to achieve a perfect e–h balance for an efficient PeLED. The energy levels and electron/hole mobilities of commonly-used ETLs and HTLs in PeLEDs are summarised in figure 18, where values are taken from [91, 262, 306, 310–326].

For a PeLED with an inverted structure, ITO, 1, 3, 5-tris(1-phenyl-1H-benzimidazol-2-yl)benzene (TPBi), and LiF/Al serve as a benchmark anode, ETL and cathode respectively. The tiny discrepancy between the work function of LiF/Al (-2.9 eV) and LUMO of TPBi (-2.7 eV) means there is almost no energy barrier for electron injection from the cathode into the relatively low CBM of perovskite materials (around -3.0 eV to -4.5 eV , as shown in figure 6(a)). However, on the anode side, the large energy difference between the work function of ITO (-4.7 eV) and the VBM of perovskites (around -5.5 eV to -7.0 eV , as shown in figure 6(a)) results in a sizeable hole injection barrier. Considering the

decent electron mobility of TPBi, an e–h imbalance can be expected for this representative inverted device. As illustrated in figure 19(a), electrons can be readily injected into the perovskite layer, and will even severely accumulate at the HTL/perovskite interface because of the fast injection and the decent electron blocking property of the HTL, resulting in a recombination zone close to the HTL/perovskite interface. However, there are two energy barriers for hole injection: one is the barrier between the ITO and HTL (which is marked as φ_1) and another is the barrier between HTL and perovskite (which is marked as φ_2). φ_1 and φ_2 cause a hole accumulation at the ITO/HTL and HTL/perovskite interfaces, respectively. Additionally, if the HTL possesses poor hole mobility, a large portion of holes are detained in the HTL and prevent rapid hole injection to the perovskite layer. In this case, the accumulation of electrons and holes at the HTL/perovskite interface causes their recombination and hence a charge carrier loss for radiative recombination in the perovskite, resulting in an inferior EQE for the PeLED.

For PeLEDs in an inverted structure, there are several strategies to improve the hole injection to reach a better e–h balance (and the strategies for a conventional structure can be deduced accordingly).

(i) Introducing an HTL with a deeper HOMO level. As illustrated in figure 19(b), a deeper-HOMO HTL results in an increased φ_1 and a reduced φ_2 . It should be noted that compared with the recombination between the holes at the ITO/HTL interface and electrons at the HTL/perovskite interface, the recombination between the holes and electrons at the HTL/perovskite interface contributes much more to the EQE loss. Therefore, although the increased φ_1 exacerbates the accumulation of holes at the ITO/HTL interface, the reduced

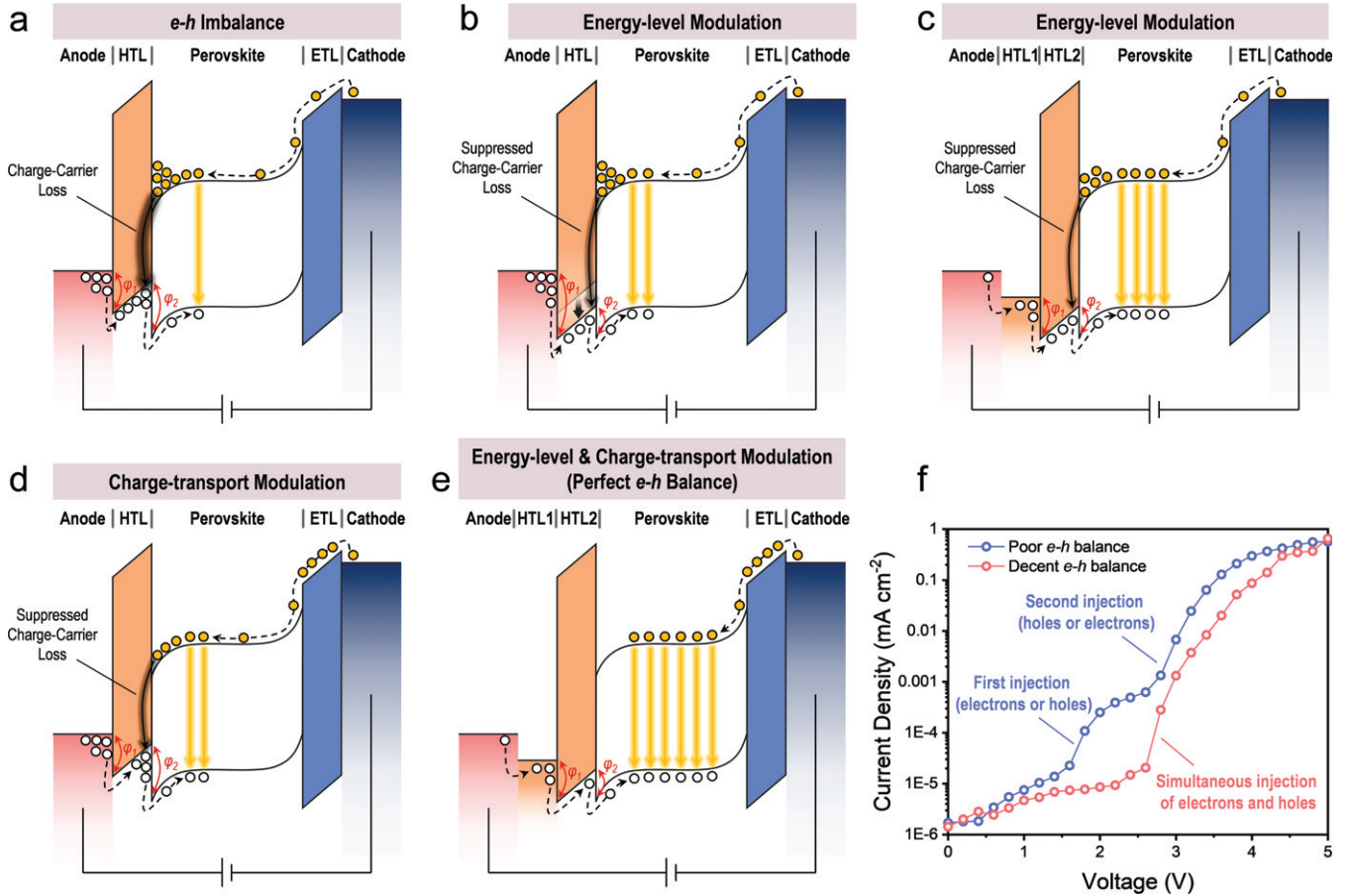


Figure 19. Strategies for achieving e-h balance in PeLED. (a) An energy diagram of a working PeLED in the case of e-h imbalance. (b) Downshifting the HOMO of the HTL to reduce the φ_2 barrier. (c) A cascade-type HTL to improve the hole injection. (d) Charge-transport modulation of HTL and ETL. (e) An energy diagram of a working PeLED under perfect e-h balance. (f) I – V curves of PeLEDs with poor and decent e-h balances.

φ_2 is more important for the EQE improvement because better injection at the HTL/perovskite interface will reduce hole accumulation at this interface and hence suppress the charge carrier loss. This rationalises the use of deeper-HOMO materials as HTLs in higher-performing PeLEDs [292, 327–329]. Therefore, selection of the HTL with a suitable HOMO level is essential for PeLED fabrication. Many useful strategies can be adopted to modulate the energy level of HTLs, such as doping [330–332], additive treatment [92, 333–335], and surface treatment with dipole molecules [336–338].

(ii) Introducing a multi-layer HTL with cascade-type energy levels. As mentioned above, when using a deep-HOMO material as the HTL, the relatively large φ_1 still causes a severe hole accumulation at the ITO/HTL interface. Although some possible processes like Auger-assisted energy up-conversion may support the charge injection [339–342], introducing another HTL with a moderate energy level to form a cascade-type energy level alignment (as the bi-layer HTL1/HTL2 shown in figure 19(c)) can be a more straightforward method to reduce φ_1 , improve hole injection, and suppress charge carrier loss. Here, HTL1 is generally a material with a high hole mobility to form a quasi-Ohmic contact with ITO, such as PEDOT:PSS ($\sim 1 \times 10^{-2} \text{ cm}^2 \text{ V}^{-1} \text{ s}^{-1}$) and NiO_x ($\sim 1 \times 10^{-3} \text{ cm}^2 \text{ V}^{-1} \text{ s}^{-1}$); meanwhile, HTL2 typically has

a deeper HOMO level, such as poly(9-vinylcarbazole) (PVK, -5.8 eV) and poly(4-butylphenyl-diphenylamine) (poly-TPD, -5.3 eV), and these cascade-type HTLs always contribute to higher-performance PeLEDs [281, 290, 306, 311, 328, 343, 344].

(iii) Charge-transport modulation. When faster electron injection occurs in a PeLED, it follows that the e-h injection can be balanced by slowing down electron transport in the ETL and/or accelerating hole transport in the HTL, thus equalizing the time taken for electrons and holes to reach the perovskite layer [312]. As illustrated in figure 19(d), slower electron transport can reduce electron accumulation at the HTL/perovskite interface, and faster hole transport facilitates hole injection from the HTL to the perovskite; both resulting in a suppressed charge carrier loss. The charge transport properties of either the HTL and ETL can be modulated by simple film-thickness control [294, 345], doping for higher charge mobility [344, 346, 347], or additive-/bilayer-treatment for lower charge mobility [312, 348, 349].

By implementing the aforementioned strategies, perfect e-h balance can be achieved without any charge carrier loss at the interface, as shown in figure 19(e). In this case, the $B_{\text{e-h}}$ factor can ideally reach unity. The experimental current density–voltage curves of PeLEDs in figure 19(f) show that

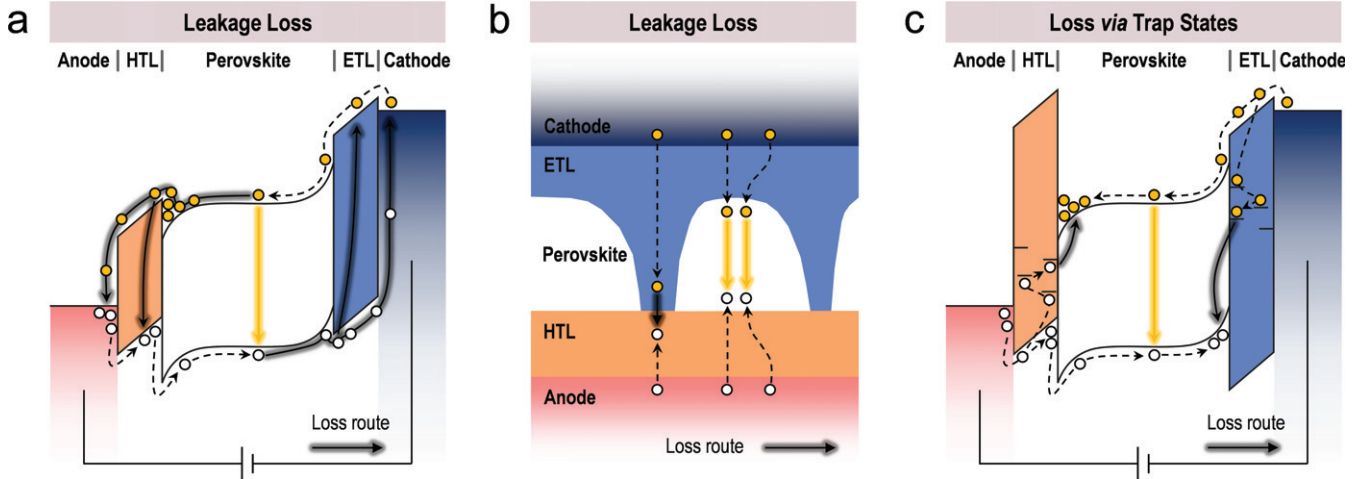


Figure 20. Parasitic losses of electrons and holes in a PeLED. (a) Leakage loss of charge carriers for the inefficient electron- and hole-blocking properties of HTL and ETL layer, respectively. (b) Leakage loss of charge carriers for a low-coverage perovskite film. (c) Loss of charge carriers via trap states in the HTL and ETL layers.

for devices with extremely poor e–h balance, as the applied voltage increases, the device current density experiences two significant jumps, which can be attributed to electron and hole injection into the perovskite layer, respectively (obviously at different applied voltages). This phenomenon can be also found in other types of LEDs with extremely poor e–h balance [350, 351]. For devices with relatively decent e–h balance, only one jump in the current density is observed, indicating simultaneous electron and hole injection to the perovskite layer at a given applied voltage.

3.5. L_{e-h} improvement

3.5.1. Modification of interfacial materials and perovskite film morphology. In a non-ideal PeLED, electrons and holes may recombine outside the perovskite layer. This constitutes a parasitic loss of the injected charge carriers available for emission from the perovskite, which is harmful to the performance of PeLEDs. Typically, there are three types of parasitic losses in a PeLED:

(i) Leakage loss of charge carriers due to the inefficient blocking properties of HTL and ETL layers. As illustrated in figure 20(a), in a PeLED with inverted structure, if the LUMO/CBM of HTL is too deep and the HOMO/VBM of ETL is too shallow, injected electrons (holes) cannot efficiently recombine in perovskite layer and instead recombine with the holes (electrons) in the HTL (ETL) or electrodes, resulting in a loss of charge carriers and a rise of the leakage current in the PeLED [352, 353]. This effect is worsened when the PeLED is under e–h imbalance. Therefore, it is important to select a shallow-LUMO/CBM HTL and a deep-HOMO/VBM ETL (to provide effective electron and hole blocking, respectively) for the target perovskite emitter, to confine the injected electrons and holes to the perovskite layer and hence suppress the leakage loss [314, 325, 348, 352]. The introduction of an insulating blocking layer for electrons and holes is generally used in device optimization [327, 353, 354].

(ii) Leakage loss of charge carriers for the low coverage of the perovskite film. Generally, solution-processed crystalline perovskite films are less homogenous than organic films. The morphology of the former systems is highly sensitive to film formation kinetics, including the nucleation and growth of perovskite crystals [355–358]. Improper control of the film formation kinetics probably leads to a perovskite film with pinholes, and after the deposition of ETL, these pinholes can result in direct contact of HTL and ETL, as shown in figure 20(b). In this case, the injected electrons and holes are able to directly recombine rather than injecting into perovskite crystals, which causes a charge carrier loss and a raised leakage current in the PeLED [285, 359]. Many strategies can assist the formation of a full-coverage perovskite film, such as additive treatment (e.g. polymer and small molecule additives) [285, 359–362] and process engineering (e.g. anti-solvent dripping and vacuum-assisted film formation) [263, 363–366]. Some reports show that the pinholes in perovskite films have no negative impact on the leakage current and device performance with specially designed PeLED structures that block direct contact of the HTL and ETL [288, 354, 367].

(iii) Loss of charge carriers via trap states in the HTL and ETL layers. As illustrated in figure 20(c), when the electrons (holes) inject into the ETL (HTL) layer, they can also be trapped by the relatively deep trap states in the ETL and HTL. Detrapping of these carriers is unlikely before further injection to the perovskite layer can commence. Therefore, they will probably recombine with holes (electrons) inside the ETL/perovskite (HTL/perovskite) interface, resulting in a charge carrier loss. Elimination of the trap states in HTLs and ETLs might involve trap passivation by small molecules [336, 368], UV-ozone treatment [369], doping [332], and modified film formation [370].

In summary, it is necessary to suppress the parasitic loss of charge carriers for an efficient PeLED. This should be achieved by improving the charge blocking capability and passivating trap states of interfacial materials, as well as by forming a

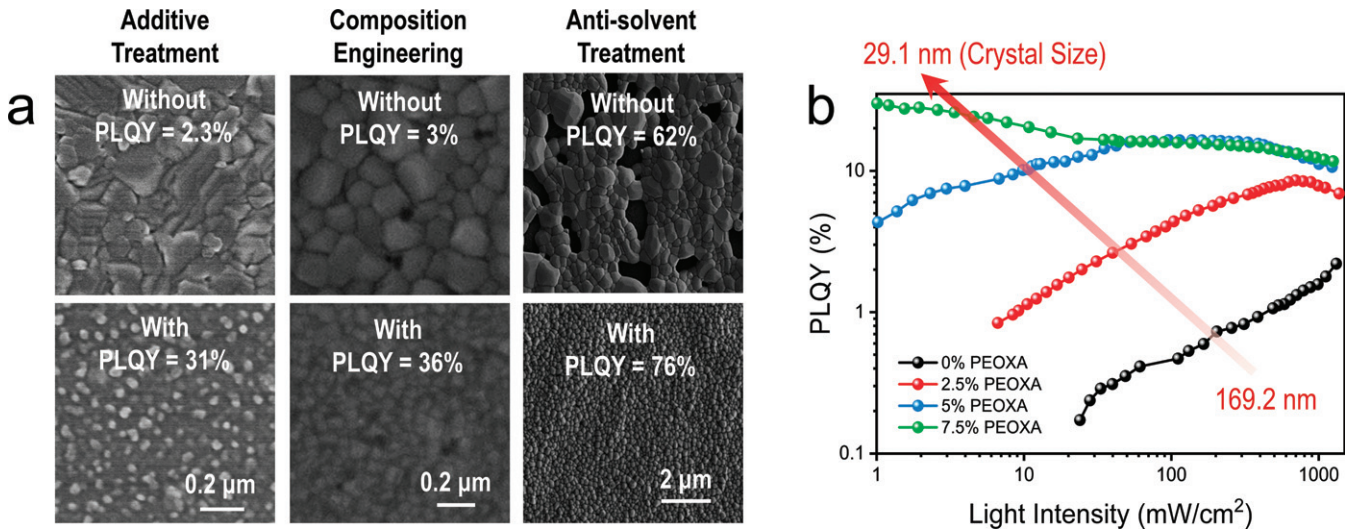


Figure 21. Relationship between crystal size and PLQY in 3D perovskites. (a) Crystal-size modulations in 3D perovskite films based on strategies of additive treatment, composition engineering, and anti-solvent treatment. The reduced crystal sizes of perovskite crystals result in enhanced PLQYs of perovskite films. (b) PLQY versus light intensity characterization for MAPbI_3 films with different crystal sizes and under with concentrations of poly(2-ethyl-2-oxazoline) (PEOXA). (a) From [40]. Reprinted with permission from AAAS. [262] John Wiley & Sons. © 2018 WILEY-VCH Verlag GmbH & Co. KGaA, Weinheim. Reprinted from [364], Copyright (2020), with permission from Elsevier. (b) [262] John Wiley & Sons. © 2018 WILEY-VCH Verlag GmbH & Co. KGaA, Weinheim.

full-coverage perovskite film to ideally reach an L_{e-h} value of 1.

3.6. ELQY (PLQY) improvement

Although there is a potential inconsistency between ELQY and PLQY, the PLQY of perovskite emitter is generally considered an acceptable way to gauge the ELQY in a corresponding PeLED, especially considering the difficulty of measuring ELQY in devices. Generally, a high-PLQY perovskite film corresponds to the high ELQY of a PeLED. We summarise the main strategies for PLQY improvement in perovskite films below.

3.6.1. Reducing the crystal size of 3D perovskites. As mentioned in section 2, excitons are easily separated into free charges in a non-excitonic 3D perovskite at room temperature. In such a system, slow bimolecular radiative recombination in the low charge carrier density region occurs and is harmful to the emission [371]. Therefore, it is important to reduce the crystal sizes of 3D perovskites to restrict the free electrons and holes to a limited space, thus increasing the odds of recombination and enhancing the radiative decay rate [262]. Several strategies have been adopted to reduce the crystal sizes of 3D perovskites for PeLED applications, such as additive treatment (including polymer [262, 360–362, 372–375] and small molecule additives [33, 359, 376, 377]), composition engineering (in perovskite films [40, 286, 378, 379] and solvents [380, 381]) and process engineering (including anti-solvent treatment [41, 263, 343, 363, 364] and laser-control crystal growth [382]). After reducing the crystal sizes to tens of nanometres, 3D perovskites start to show excitonic nature, and the PLQYs of perovskite films dramatically climb, as shown in figure 21(a), which also benefits a higher-performance PeLED. In addition,

figure 21(b) shows that the peak PLQY shifts to the lower light intensity region upon the reduction of crystal size, which can be attributed to the aforementioned faster radiative decay rate in smaller perovskite crystals [262].

3.6.2. Utilising the nanostructures of quasi-2D perovskites. 3D perovskites can successfully generate light at room temperature, suggesting mild thermal quenching of excitons (although this still affects the PLQY of 3D perovskites, as shown in figure 22(a)). However, the relatively high trap densities ($\sim 10^{16} \text{ cm}^{-3}$) and the slow radiative decay rate at low charge carrier densities restrict their LED performance [383–386]. As shown in figures 22(a) and (b), the PLQY of 3D perovskites increases sharply with charge carrier density until $\sim 10^{17} \text{ cm}^{-3}$, then begins to decrease at higher densities approaching 10^{18} cm^{-3} . This can be explained by the transition of the dominant decay process from monomolecular recombination (non-radiative in 3D perovskite), to bimolecular recombination (radiative), and finally Auger recombination (non-radiative) with increasing charge carrier density [262, 371]. Figure 22(c) echoes that when the charge carrier density is below 10^{16} cm^{-3} , non-radiative monomolecular recombination dominates the total recombination, causing a relatively low PLQY of 3D perovskite. However, the decay rate of radiative bimolecular recombination raises quickly and starts to dominate the total recombination when the charge carrier density increases from 10^{16} cm^{-3} to 10^{17} cm^{-3} . When the charge carrier density increases to over 10^{17} cm^{-3} , the non-radiative Auger recombination starts to become obvious and hence causes a decrease of PLQY [262, 371].

Although the PLQY of 3D perovskites is high at a charge carrier density around 10^{17} cm^{-3} , the general working charge carrier density of a PeLED device is typically below 10^{16} cm^{-3} [387], where the PLQY of 3D perovskite is relatively poor.

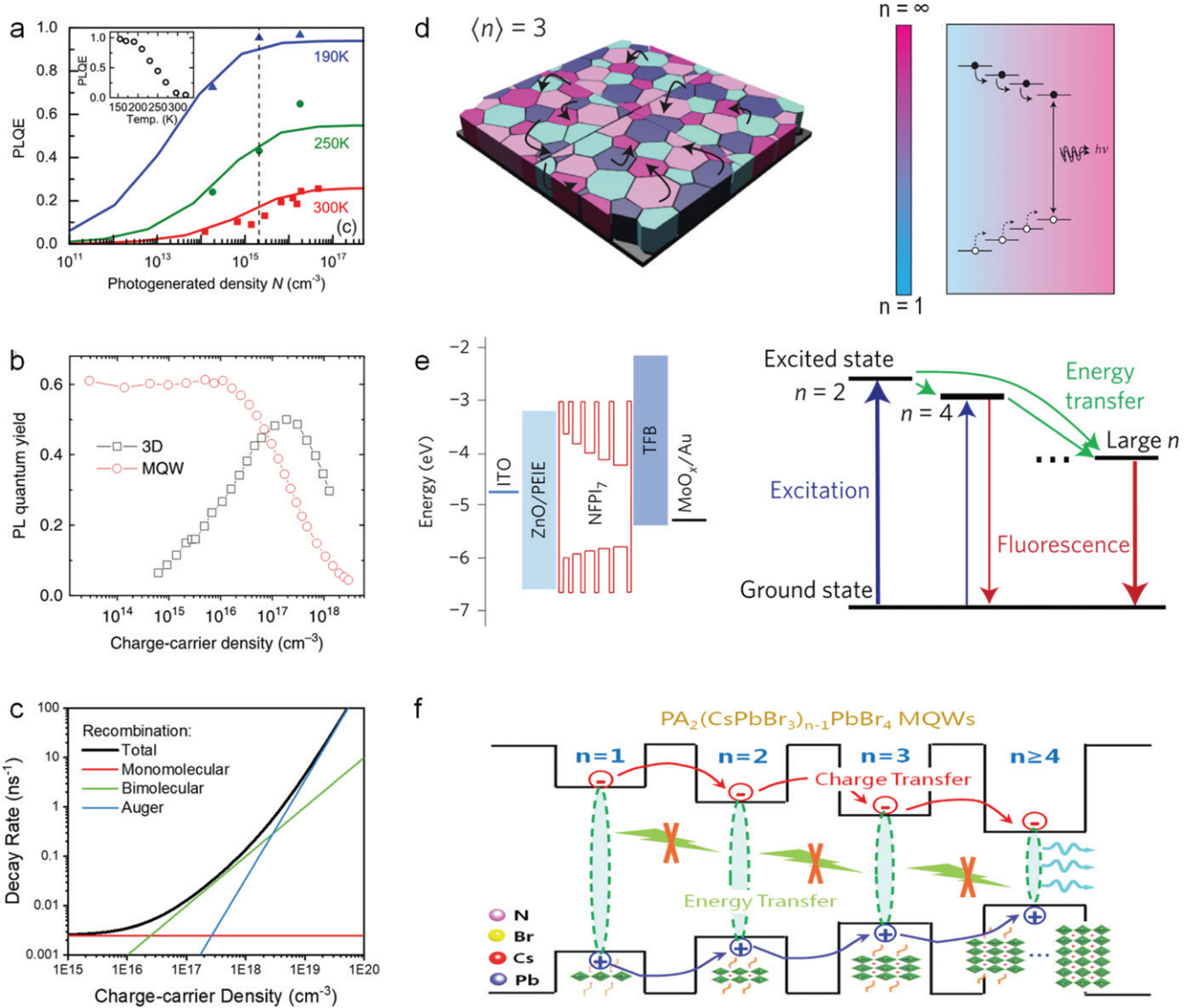


Figure 22. PLQY and proposed charge/energy transfer mechanism in quasi-2D perovskites. (a) Charge carrier-density-dependent PLQY of 3D $\text{MAPbI}_{3-x}\text{Cl}_x$ film at various temperatures. Inset: PLQY as a function of temperature through the range in which the perovskite crystal remains in the tetragonal phase (155–320 K) under the quasi-steady-state photogenerated density of $\sim 2 \times 10^{15} \text{ cm}^{-3}$. (b) PLQY of 3D and quasi-2D (marked as MQW here) perovskite films under various charge carrier densities. (c) The decay rate of a 3D perovskite film under various charge carrier densities. (d) The charge transfer (so-called energy funneling effect) between different perovskite grains. (e) Energy transfer cascade in an MQW. (f) Charge transfer cascade in an MQW. (a) Reprinted figure with permission from [385], Copyright (2014) by the American Physical Society. (b) Reprinted by permission from Springer Nature Customer Service Centre GmbH: Nature Communications [371] © 2017. (c) [262] John Wiley & Sons. © 2018 WILEY-VCH Verlag GmbH & Co. KGaA, Weinheim. (d) Reprinted by permission from Springer Nature Customer Service Centre GmbH: Nature Nanotechnology [282] © 2016. (e) Reprinted by permission from Springer Nature Customer Service Centre GmbH: Nature. Nature Photonics [283] © 2016. (f) Reprinted from [388], Copyright (2018), with permission from Elsevier.

However, the quasi-2D perovskites with unique nanostructures can efficiently solve this issue. According to the previous discussion, quasi-2D perovskites are a 3D/2D hybrid structure that contain multiple perovskite components with different bandgaps. Photoexcited electrons and holes in 2D perovskites with smaller n values (larger bandgaps) will eventually transfer to the 3D component (or the largest- n 2D component). Three possible transfer mechanisms have been reported in the literature: (i) charge transfer between different perovskite grains (the so-called energy funneling effect), as shown in figure 22(d); [282] (ii) energy transfer in the MQW, as shown

in figure 22(e); [283] (iii) charge transfer in the MQW, as shown in figure 22(f) [388]. These three processes all occur on the picosecond time scale, dramatically enhancing the local charge carrier density in the 3D components [282, 283]. Therefore, in quasi-2D perovskites, in the case that the overall charge carrier density matches with that in a working PeLED ($< 10^{16} \text{ cm}^{-3}$), the local charge carrier density of its 3D component should be even higher (probably $> 10^{16} \text{ cm}^{-3}$) following the above transfer events, leading to high PLQY from quasi-2D perovskite films with relatively low overall charge carrier density, as shown in figure 22(b). It is worth noting that

although electrical injection differs from photoexcitation, charge carriers still tend to accumulate in the 3D components under electrical injection due to the relatively low electrical resistance of the 3D component. Therefore, PeLEDs based on quasi-2D perovskites can attain high PLQY in a relatively low charge carrier density region ($<10^{16} \text{ cm}^{-3}$), matching the general needs of a PeLED device. The mixed-dimensional aspect is also important in that excitons in pure 2D perovskites (especially those with small n values) undergo severe thermal quenching, and their PeLEDs generally suffer poor efficiencies at room temperature [170, 277].

3.6.3. Reducing trap states of perovskite crystals. As discussed in section 2.4, trap-assisted recombination is a typical non-radiative loss pathway for PeLEDs with narrow-FWHM spectra. The relatively high trap densities in 3D perovskites ($\sim 10^{16} \text{ cm}^{-3}$) make trap-assisted recombination the main reason for PLQY loss at PeLED operating conditions ($<10^{16} \text{ cm}^{-3}$). In other words, injected charge carriers can be easily trapped and non-radiatively recombine within the relative abundance of trap states in 3D perovskites. The suppression of trap states and trap-assisted recombination in perovskite crystals is therefore critical for achieving highly emissive PeLEDs. Theoretical calculations in figure 23(a) show that if the monomolecular recombination decay rate constant (k_1 , which is dominated by trap-assisted recombination in 3D perovskites) can be reduced from 10^6 s^{-1} to 10^3 s^{-1} , which represents a dramatic reduction of trap density, the calculated PLQY (i.e. radiative efficiency) reaches a high value when the charge carrier density resides in the 10^{14} to 10^{17} cm^{-3} region (as expected for working PeLEDs) [389]. This is echoed by figure 23(b), which shows that the total recombination rate is only dominated by non-radiative monomolecular recombination (or trap-assisted recombination) at the charge carrier densities below 10^{13} cm^{-3} , while the radiative bimolecular recombination dominates the total recombination at the charge carrier density region between 10^{14} to 10^{17} cm^{-3} [262].

Interestingly, trap states of perovskite crystals are principally located at their surface rather than within the bulk, which underscores the importance of surface engineering for improving the lighting properties of perovskites, as shown in figure 23(c) [164, 287, 384, 390]. Generally, surface modulation by organic ligands is an efficient strategy to passivate the surface traps of 3D perovskite crystals [38, 285, 391], and internal PLQYs exceeding 90% can be achieved under careful surface treatment [392]. The organic ligands also allow 2D perovskites to obtain a lower trap density of around 10^{15} cm^{-3} [383, 393, 394], which is another reason for the high PLQY of quasi-2D perovskites at charge carrier densities below 10^{16} cm^{-3} . For perovskite NCs, which already possess desirable excitonic behaviour and fast radiative decay rates, surface passivation plays an even more important role in PLQY improvement on account of their large surface area-to-volume ratios. Many strategies have been proposed to passivate the surface traps of perovskite NCs, such as modulating surface stoichiometry of perovskite NCs [395], doping [396], post-treatment [397], ligand modulation [398], etc. Blending per-

ovskite crystals with a polymer containing special functional groups (e.g. S, O, N) to form Lewis-base and Lewis-acid interaction with perovskite can also effectively reduce surface traps [360, 361, 372].

3.7. LEE improvement

When photons propagate from a higher-refractive-index material to a lower-refractive-index material with an incident angle larger than the critical angle, total internal reflection occurs at their interface. In an LED device, light is typically generated by an emissive layer with a refractive index much larger than air, causing a severe total internal reflection within the device and hence prohibiting the escape of the light. Therefore, light trapping is a huge issue in LED devices and can result in remarkable losses to the EQE. This issue is severe in PeLEDs because of the high refractive indices of perovskite materials (typically larger than 2.0, as summarised in figure 24(a)) [157, 216, 399–405], causing over 75% of the emitted photons to be trapped in the device [404, 406, 407]. Interestingly, the overall refractive indices of quasi-2D perovskites are smaller than that of 3D perovskites, which can be attributed to the presence of the organic components with small refractive indices [407]. The smaller refractive indices of quasi-2D perovskites also facilitates a better PeLED performance.

Emitted photons give rise to numerous optical modes within a PeLED, including parasitic absorption loss, surface plasmon polariton mode (SPP mode), waveguide mode, substrate mode, and out-coupled mode, as shown in figure 24(b). Parasitic absorption is the loss of photons that are absorbed by each functional layer. SPP mode is the loss of photons that trigger longitudinal oscillation of electrons at the metal/dielectric interface. Waveguide mode results from the photons that are trapped within the multi-layer ITO/HTL/perovskite/ETL structure. Substrate mode results from the photons that are trapped within the thick glass substrate [407, 408]. All of these optical modes lead to a loss of photons in a PeLED, and only the out-coupled mode contributes to the far-field propagation of photons. The LEE describes the ratio between the out-coupled mode and the total optical modes in a PeLED.

3.7.1. Optical parameter control in PeLEDs. The management of different optical modes necessitates systematic engineering, as every optical parameter change in PeLEDs can make an impact on all the optical modes. We summarise the key factors below:

(i) Refractive index and thickness of functional materials in PeLEDs. As the transparent conductive oxide (i.e. ITO) and reflective metal electrode are generally fixed in device fabrication, the refractive indices and thicknesses of the HTL, perovskite emitter and ETL are more convenient to modify. As shown in figure 25(a), when the refractive index of the perovskite is relatively small (1.75), all the optical modes are almost independent of the perovskite layer thickness, which facilitates device fabrication reproducibility. However, when the refractive index of the perovskite is relatively high (2.5), the out-coupled mode becomes highly thickness-dependent, such that a nanometer-scale thickness change of the perovskite film can make a substantial difference to LEE, which might

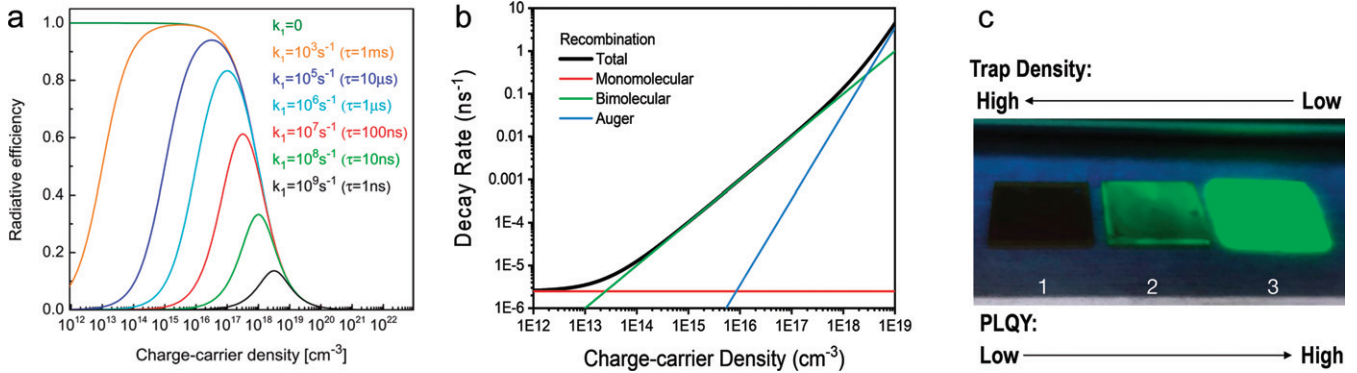


Figure 23. PLQY improvement by the trap state reduction in perovskites. (a) Calculated PLQY (i.e. radiative efficiency) assuming various monomolecular decay rate constants (k_1) in 3D perovskite, where monomolecular recombination is dominated by trap-assisted recombination. (b) The decay rate of 3D perovskite film with small k_1 value ($2.5 \times 10^3 \text{ s}^{-1}$) at various charge carrier densities. (c) Photographs of perovskite films with different trap densities and PLQYs under ultraviolet light. (a) Reprinted with permission from [389]. Copyright (2015) American Chemical Society. (b) [262] John Wiley & Sons. © 2018 WILEY-VCH Verlag GmbH & Co. KGaA, Weinheim. (c) Reprinted by permission from Springer Nature Customer Service Centre GmbH: Nature [287] © 2018.

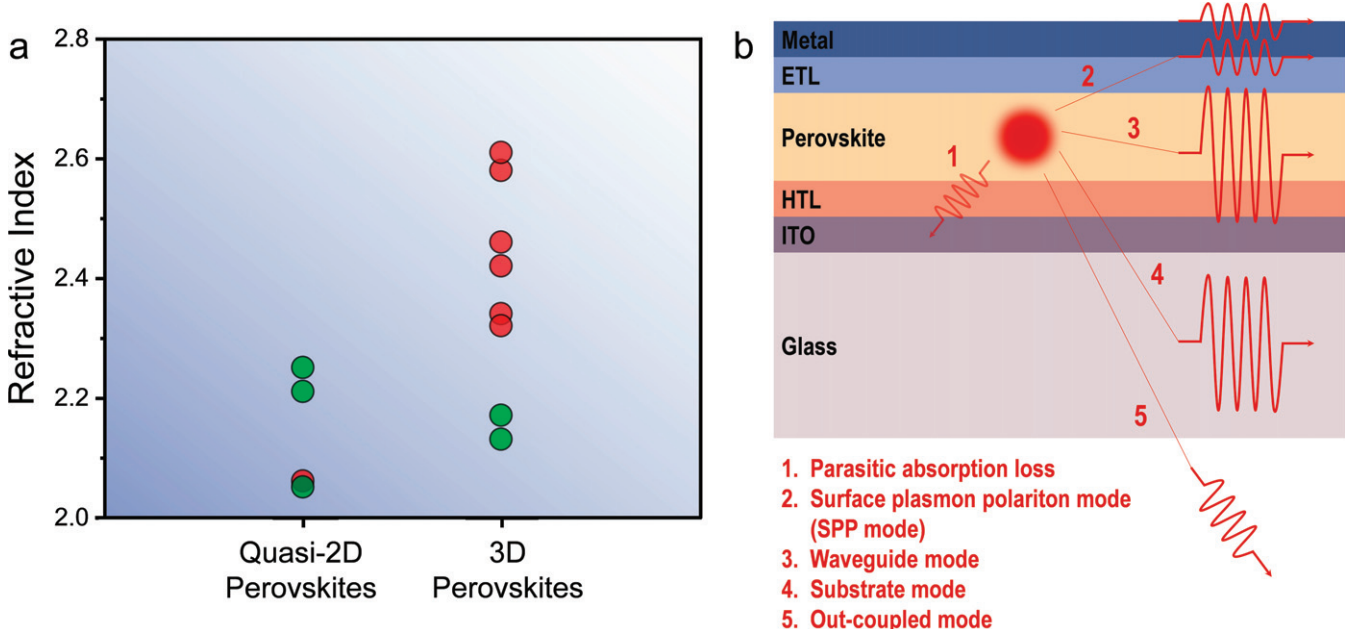


Figure 24. (a) Refractive indices of quasi-2D and 3D perovskites at their peak emission wavelengths (green and red dots represent the emission colour). (b) Different optical modes of light propagation within a PeLED.

be one of the reasons behind poor reproducibility of solution-processed PeLEDs. The refractive indices and thicknesses of the HTL and ETL also significantly impact LEE. According to figure 25(b), in an inverted device structure, reducing the refractive index of the ETL (to limit the photon propagation to the metal electrode side) and increasing the refractive index of the HTL (to enhance the photon propagation to the ITO side) are effective ways for achieving superior device performance. However, these general rules only work for the green and blue PeLEDs; a HTL and ETL with low refractive indices are both needed for efficient red PeLEDs [407]. According to figure 25(c), in an inverted structure, the LEE is more sensitive to the ETL thickness than the HTL thickness. Modulating the LEE through ETL thickness should therefore be

considered, alongside the electronic property changes in the aforementioned discussion.

(ii) Emission wavelength and orientation. Besides the potential parasitic absorption within the device for different photon energies, different emission wavelengths could also cause a change to the cavity formed inside the PeLED, which makes a huge difference to the out-coupled mode [407]. As shown in figure 26(a), in a fixed device structure, the changes of emission wavelength from red to green to blue dramatically reduce the LEE from 21.9% to 12.6% to 9.4%. This result suggests that, in terms of light extraction, no universal PeLED device structure works efficiently for all emission wavelengths, and the optical parameters of all the functional layers need

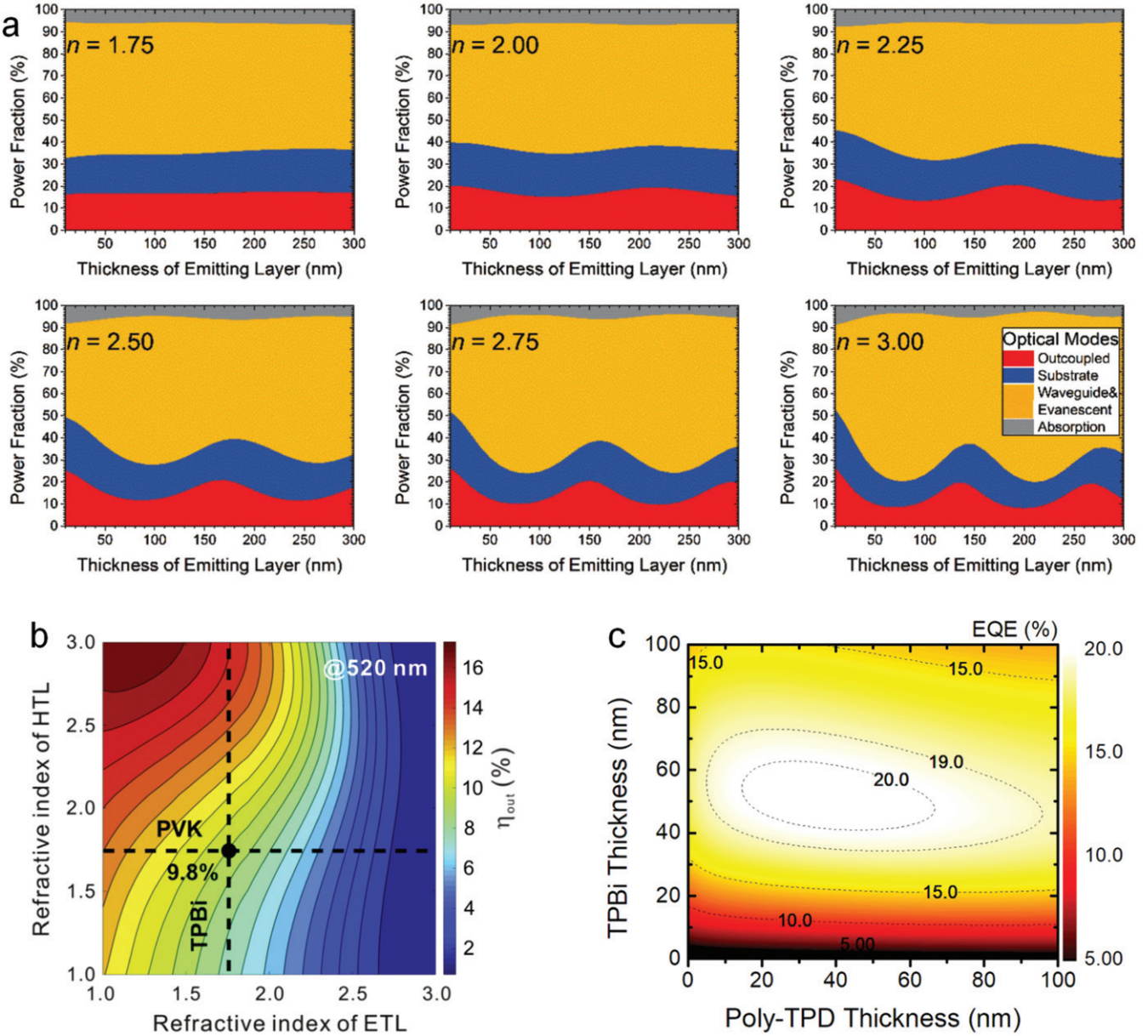


Figure 25. Impact of refractive indices and thicknesses of perovskite layer, HTL, and ETL on LEE. (a) Power distribution of different optical modes of PeLEDs with various refractive indices and thicknesses of the perovskite emitter. (b) Dependence of the simulated LEE (the same as η_{out} here) on the refractive indices of ETL and HTL for PeLEDs emitting at 520 nm. The circle symbols indicate the predicted LEE of PeLED based on TPBi ETL and PVK HTL. (c) Contour plot of the maximum achievable LEE (the same as EQE here) of the PeLED as a function of the thicknesses of poly-TPD (HTL) and TPBi (ETL). (a) [404] John Wiley & Sons. © 2018 WILEY-VCH Verlag GmbH & Co. KGaA, Weinheim. (b) Reprinted from [407], Copyright (2018), with permission from Elsevier. (c) Reprinted by permission from Springer Nature Customer Service Centre GmbH: Nano Covergence [402] © 2019.

to be optimized for each particular emission wavelength. Furthermore, in OLEDs, reports show that device performance is sensitive to the orientation of the emission dipole [409, 410]. In the perovskite family, 3D perovskites and perovskite NCs/QDs are typically isotropic materials and hence cause no inclined dipole orientation of the ultimately emitted photons. To the best of our knowledge, no experimental study of dipole orientation in 2D or quasi-2D perovskite has been reported to date, however, we expect that their anisotropic nature probably causes a distinct dipole orientation of emitted photons. On this token, the preferential growth of 2D or quasi-2D per-

ovskites in the film may possibly incline the dipole orientation of the emitted photons. The results of a theoretical simulation in figure 26(b) confirm that if emitted photons have a horizontal dipole orientation parallel to the device surface, a high LEE can be achieved in the device. On the other hand, if the dipole orientation turns perpendicular to the device surface, the LEE can drop to an ultra-low level.

3.7.2. Light extraction structure. Generally, light trapping is severe in all kinds of thin-film LEDs and the introduction of extra light extraction structures can greatly improve the LEE.

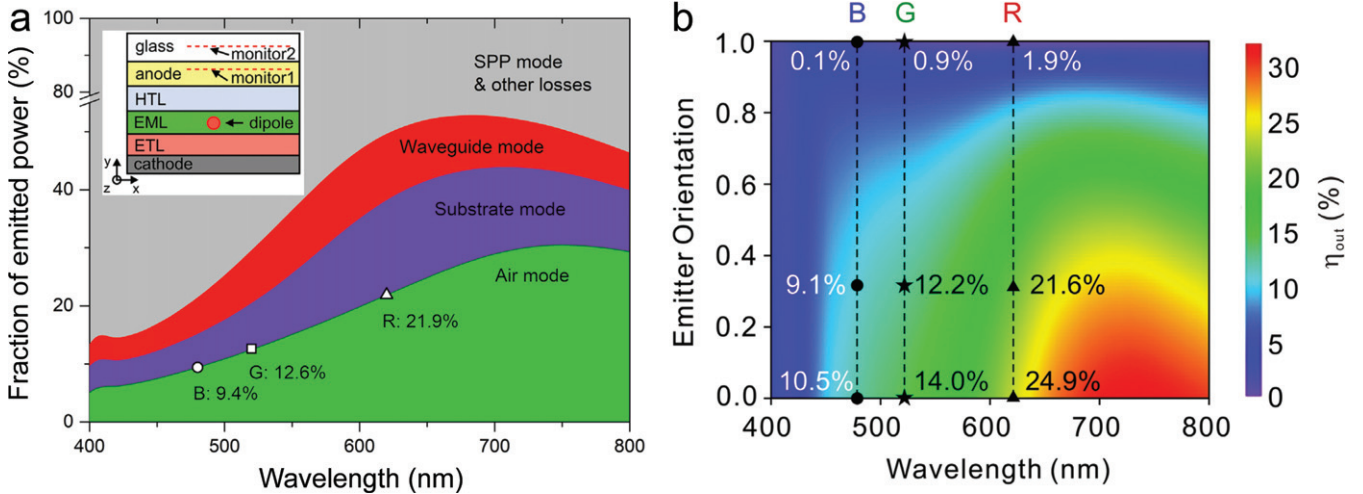


Figure 26. Impact of emission wavelength and orientation on LEE. (a) Power distribution of different optical modes of PeLEDs with different emission wavelengths. The theoretical maximums of red (620 nm, circle), green (520 nm, star), and blue (480 nm, triangle) emitted power into the air are marked, respectively. The inset shows the schematic illustration of the device structure and simulation setup. (b) Calculated LEE (marked as η_{out} here) of planar PeLEDs with different dipole orientations and emitting wavelengths. The value of 0 indicates the horizontal orientation of the emitter dipole relative to the device surface. The dashed lines mark the changes of the emission at 480 nm (blue), 520 nm (green), and 620 nm (red), respectively. (a), (b) Reprinted from [407], Copyright (2018), with permission from Elsevier.

Several different light extraction studies have been reported in the PeLED field, and are summarised below:

(i) Breaking down the ultra-flat interface in a thin film PeLED. In a thin film PeLED, all the interfaces are ideally ultra-flat, which theoretically leads to a permanent trap of photons in waveguide and substrate modes. An efficient way to solve this issue is to introduce one (or more) textured interfaces within the device. As shown in figure 27(a), a patterned ZnO layer was introduced into the PeLED by a transfer printing technique, which also induced the formation of patterned PEDOT:PSS and perovskite layers. This textured surface encourages leakage of the lateral-propagating waveguide mode to the glass substrate, suppressing the waveguide mode but partly strengthening the substrate mode. Therefore, an out-coupling lens was still needed to further convert the substrate mode to an out-coupled mode for an even better PeLED with EQE of 28.2% [411]. Instead of introducing an out-coupling lens outside the device, integrating a photonic crystal is also an effective way to extract light. As shown in figure 27(b), a similar patterned device structure was used to suppress the waveguide mode. Moreover, a NW photonic crystal composed of anodic alumina membrane and TiO₂ was introduced between the ITO and glass substrate to convert more waveguided modes to leaky modes (scattering resonance), which further enhanced the LEE to a high value of 73.6% [412]. Besides the introduction of a patterned interface, the formation of isolated large perovskite crystal grains (with submicrometre scale for efficient light scattering, as shown in figure 27(c)) and the formation of a perovskite nanophotonic wire array (with leaky mode behaviour, as shown in figure 27(d)) are also promising methods for improved light extraction [288, 413].

(ii) Introducing nanoparticles within the injection layer. Reports show that the incorporation of metal nanoparticles in the injection layer (such as Au and Ag nanoparticles, as

shown in figure 27(e)) can contribute to the EQE improvement. Several effects can be induced by these metal nanoparticles, such as light scattering effects for waveguide mode suppression [414], the far-field plasmonic effect on a mirror-type substrate for light transmission enhancement [415], and the near-field plasmonic effect for radiative decay rate acceleration of perovskite emitters [416].

(iii) Utilising the near-field optics to extract the trapped optical modes within PeLEDs. In PeLEDs, when photons propagate to the metal electrode and are in the internal total reflection condition, an evanescent wave is generated and its energy penetrates to the adjacent layer in the near field, as shown in figure 27(f), which becomes an opportunity to utilise the evanescent wave and hence suppress the waveguide mode. In addition, the evanescent wave can also induce the SPP mode; its energy also penetrates to the adjacent layer in the near field and hence can be utilised [301].

Figure 27(g) illustrates the use of the near-field evanescent wave and SPP to improve the light extraction and achieve the state-of-the-art white light [301]. For a semi-transparent blue PeLED, a red perovskite layer is deposited above the ultra-thin metal electrode and within the penetration depth of the evanescent wave and SPP. Three near-field effects occur: photon tunnelling, evanescent wave absorption, and SPP absorption. Photon tunnelling from the blue PeLED to the red perovskite layer allows blue photons under the total internal reflection condition to overwhelm the optical barrier imposed by the high refractive index of the red perovskite layer; the evanescent wave and SPP absorption occur due to the high absorption coefficient of the red perovskite layer for the blue photons. Consequently, this device design provides three channels for the trapped blue photons to escape from the emissive layer and hence suppress the waveguide and SPP modes simultaneously. Moreover, by combining the blue and down-converted red photons, highly

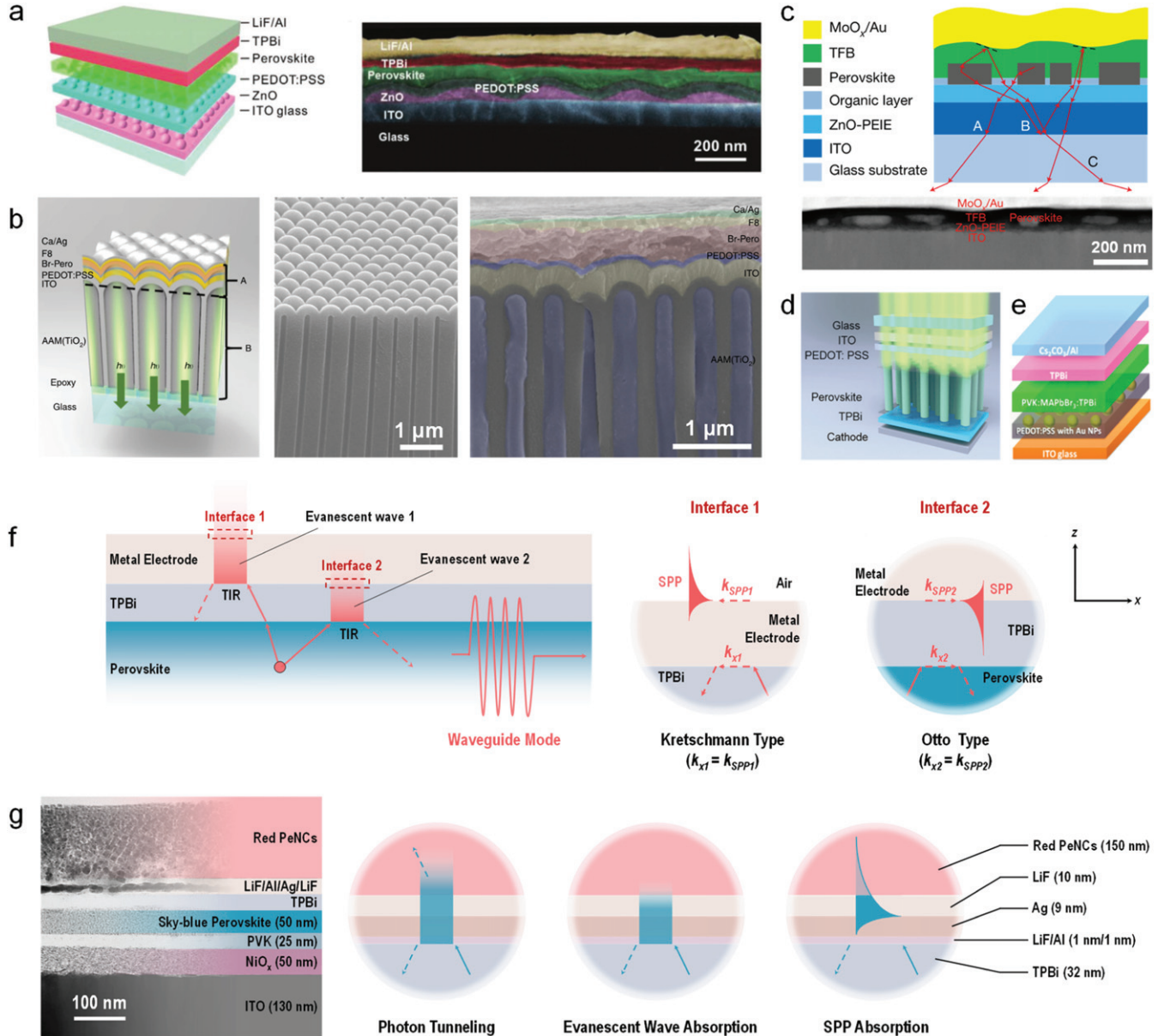


Figure 27. Light extraction structures in PeLEDs. (a) Schematic diagram and cross-section scanning electron microscopy (SEM) image of patterned CsPbBr_3 PeLED. (b) Schematic diagram of device structure (left), SEM image of the light extraction structure (middle), cross-sectional SEM image of PeLED (right). (c) Schematic diagram of a device structure that can extract light with submicrometre perovskite crystals (top); scanning transmission electron micrograph of the cross-section of a PeLED (bottom). (d) Schematic diagram of PeLED with perovskite nanophotonic wire array. (e) Schematic diagram of PeLED with the incorporation of Au nanoparticles in the PEDOT:PSS layer. (f) Schematic diagram of two types of SPPs (Kretschmann and Otto types) induced by evanescent waves 1 and 2, respectively. (g) Cross-section image of a white PeLED and a schematic diagram showing the three different optical effects presented in the metal electrode side of such a device. (a) [411] John Wiley & Sons. © 2019 WILEY-VCH Verlag GmbH & Co. KGaA, Weinheim. (b) Reproduced from [412]. CC BY 4.0. (c) Reprinted by permission from Springer Nature Customer Service Centre GmbH: Nature [288] © 2018. (d) Reprinted with permission from [413]. Copyright (2020) American Chemical Society. (e) Reprinted with permission from [416]. Copyright (2017) American Chemical Society. (f), (g) Reprinted from [301], Copyright (2020), with permission from Elsevier.

efficient white PeLEDs with EQE exceeding 12% have been successfully demonstrated [301].

3.7.3. Contribution of photon recycling. As mentioned in section 2.2, because of the minuscule Stokes shift in perovskite materials, the emission spectra of perovskites strongly overlap with their absorption edges, which leads to a photon recycling process that facilitates a better LEE in the device [216]. As shown in figure 28(a), in a device without pho-

ton recycling, only photons within the out-coupled cone can escape the device, while the remaining photons are permanently trapped in the device as waveguide modes, according to the previous discussion. However, in a device with photon recycling, as shown in figure 28(b), the waveguide mode can be re-absorbed by the perovskite and then re-emitted as photons. Because of the random emission direction, the re-emitted photon within the out-coupled cone can escape the device again. If the efficiency of photon recycling is high,

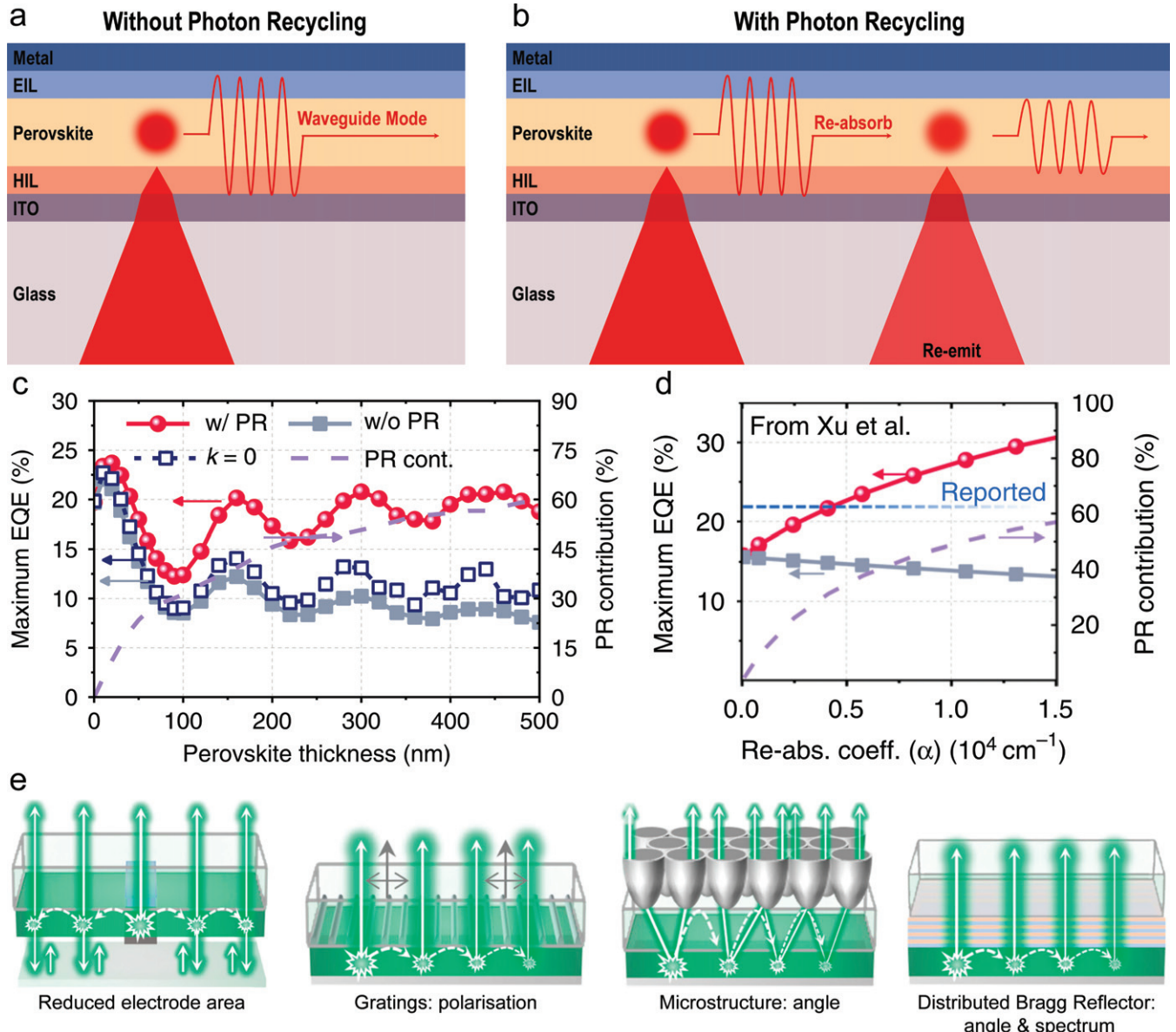


Figure 28. Photon recycling in PeLEDs. Schematic diagram of PeLEDs working without (a) or with (b) photon recycling. (c) Calculated EQEs with photon recycling (closed red circles), without photon recycling (closed grey squares) and without re-absorption (open navy squares), as well as relative photon recycling contribution (violet dashed lines) for an ideal PeLED (IQE = 100%) with various perovskite thicknesses and (d) for the PeLED structure reported by Xu *et al* with 100% IQE. (e) Approaches to maximize the benefit of photon recycling. (c)–(e) Reprinted by permission from Springer Nature Customer Service Centre GmbH: Nature Communications [216] © 2020.

this process can gradually convert a portion of photons in the waveguide mode to the out-coupled mode, improving the overall LEE in the device. Therefore, in the ideal case that internal quantum efficiency of the perovskite reaches 100%, improving the re-absorption of photons by increasing the thickness and re-absorption coefficient of the perovskite layer can strengthen the photon recycling process and facilitate a better LEE for PeLEDs [216].

As shown in figure 28(c), for devices without photon recycling, the EQE of the PeLEDs gradually decreases with increased perovskite thickness because the maximum EQE without re-absorption (open navy squares) finally converges to the ray-optical limit of $1/2n_r^2$ (n_r represents refractive index) after the weakening of the optical cavity effect. A

further loss emerges when considering re-absorption (closed grey squares). However, in the device with photon recycling, these re-absorbed photons contribute a lot to the overall EQE, and this contribution gradually increases with the film thickness. A similar result is observed when increasing the re-absorption coefficient value, as shown in figure 28(d). In this case, Cho *et al* concluded that photon recycling might contribute more than 70% to the overall emission [216]. As well as maximizing the benefit of photon recycling, several device designs have been proposed to further improve the properties of PeLED, such as reduced electrode area (to suppress the SPP mode), introducing a grating (to align the photon polarisation), introducing microstructures (to confine the emission angle) and introducing a distributed Bragg reflector (to

narrow both the emission angle and spectrum), as shown in figure 28(e). As discussed in section 2.2, other effects of photon recycling related to PeLEDs include a redshift of the emission spectrum, improvement of charge transport [417] and increase of the intrinsic recombination constant in the PeLED [242].

4. Conclusions and future outlook

In this work, we assimilate key concepts relevant to the development of PeLEDs spanning the perspectives of materials, photophysics and device-engineering research. The conspectus below summarises the most salient points from each, and our standpoint on the current position of the field.

In the ‘materials’ section, we introduce the MHP family as a unique class of optoelectronic materials with highly configurable properties. In these systems, the most substantive tuning effects are achieved by compositional engineering. In particular, the B- and X-site ions govern the energetics of the CB and VB, and thus the modulation of these ions can be used to widely tune the emission colour of MHPs from the violet (~ 400 nm) to near-infrared (~ 1000 nm), covering the main lighting demands in our daily life. Meanwhile, modulation of the A-site cation indirectly affects the bandgap of perovskite by changing the volume of the ABX_3 lattice or introducing a distortion, thereby facilitating a fine tuning of the emission colour. Organic ligands provide an additional ‘dimensional’ engineering handle to produce 3D, 2D/quasi-2D, and 0D perovskites with distinct optical and electronic properties. The organic ligands in the 2D/quasi-2D perovskite derivatives and 0D perovskite QDs/NCs can also be rationally designed to provide better packing, energy confinement, size control and trap passivation etc. Taken together, these approaches have already yielded a large variety of perovskite emitters that have been incorporated into colourful PeLEDs.

In the ‘photophysics’ section, we comprehensively discuss excited states in MHPs (their general characteristics, energy/charge transport processes, radiative and non-radiative decay mechanisms and PL properties) as the basis for engineering the collective lighting properties of PeLEDs. One of the most extraordinary facets of MHPs is the ability to control the exciton binding energy (and thus the balance between free carriers and excitons) through the aforementioned material composition and dimensionality (i.e. quantum and dielectric confinement). Nanomaterials are particularly facile in this regard, and also enable the natural formation of energy/charge-transfer cascades between MHP grains of different dimensions to produce high colour purity of emission and minimal non-radiative recombination. In both bulk and low-dimensional systems, this energy transport can extend over considerable length scales owing to the intense emission and reabsorption of photons (photon recycling). Relative to other solution-processable semiconductors, MHPs also exhibit quite high intrinsic carrier mobilities (indicative of band-type transport), low electronic disorder and slow cooling/non-radiative recombination of carriers. These factors have been attributed to the formation of large polarons that are engendered by carrier-phonon coupling in the soft, polar MHP lattice. We also

highlight how other factors such as Rashba splitting, STE, dark states and AIE may also have a role to play in the unusual PL properties of MHPs.

In the ‘device engineering’ section, we examine the strategies that have significantly contributed to the development of PeLEDs, and discuss their specific role in improving the EQE parameters of PeLEDs, i.e. electron–hole balance ($B_{\text{e–h}}$), charge carrier loss ($L_{\text{e–h}}$), electroluminescence quantum yield (ELQY) and light extraction efficiency (LEE). We illustrate how $B_{\text{e–h}}$, $L_{\text{e–h}}$ and LEE pertain to the quality of the overall device; $B_{\text{e–h}}$ and $L_{\text{e–h}}$ are especially dependent on the properties of the HTL/ETL, while LEE can be improved by careful consideration of the optical parameters of each layer as well as special light-extracting structures. Meanwhile, the ELQY pertains to the perovskite active layer, wherein the main challenges involve realising efficient emission at device-operating conditions (i.e. charge carrier densities $< 10^{16} \text{ cm}^{-3}$). To this end, we touch upon approaches to control the domain size, the use of nanostructures and the amelioration of trap states in MHP crystals. Theoretically, $B_{\text{e–h}}$, $L_{\text{e–h}}$, LEE and ELQY can all achieve unity to give PeLEDs with 100% EQE.

Although the concepts above have been used to drive meteoric progress in perovskite lighting, several issues need to be tackled before the ultimate commercialisation of PeLEDs. Here we broach the key challenges which we feel should constitute mainstream PeLED research in the foreseeable future:

(i) Blue (particularly deep-blue) PeLEDs. According to figure 17, the EQEs of near-infrared, red, and green PeLEDs have already exceeded 20%, but the performance of blue PeLEDs still severely lag behind. The slow development of blue PeLEDs can be attributed to several factors, such as the large carrier injection barrier in the device, insufficient carrier blocking capabilities of HTL/ETL, and relatively low PLQY of blue perovskite emitters. These problems are particularly concerning for deep-blue PeLEDs due to the large bandgaps of the underlying perovskites, which means that existing HTLs (e.g. poly-TPD and PVK) and ETLs (e.g. TPBi and 1, 3, 5-tri[(3-pyridyl)-phen-3-yl]benzene) cannot completely fulfil the carrier injection and blocking demands of the devices. To this end, novel charge transport layers with suitable energy levels should be developed with blue emitters in mind. In addition, non-radiative decay channels in the large-bandgap materials should be clearly studied to devise approaches for improving the PLQY.

(ii) White PeLEDs. Figure 17 also conveys the infancy of white PeLED research. We expect this direction will gradually attract more attention once the aforementioned challenges in blue PeLEDs are solved. The high colour purity of MHPs mean that three-colour white PeLEDs have great potential to be used as a backlighting source in liquid crystal displays and in a wavelength-division-multiplexing ‘Li-Fi’ technique, however, a triple-junction tandem cell and a three-pixel white PeLED have not been demonstrated yet. Furthermore, the small FWHM of conventional perovskite emitters is problematic for obtaining a high colour rendering index. To address this issue, broad-spectrum emitters based on other materials (e.g. organics) may be incorporated into the devices. Alternatively,

broad-spectrum perovskite emitters utilising STE or trap-state emission may provide the answer.

(iii) Novel light out-coupling strategies. The high EQEs (>20%) of near-infrared, red and green PeLEDs suggests that B_{e-h} , L_{e-h} and ELQY are approaching unity in the optimal cases, and therefore, the low LEE is the main bottleneck in overall device performance. Among the optical modes trapped within PeLEDs: the parasitic absorption loss is unavoidable; the substrate mode can be commercially solved by forming an optical lens on the substrate side during the epoxy encapsulation process; the waveguide mode might be addressed if the incorporation of textured interfaces or photonic crystals into device fabrication can be made less complicated and expensive; the SPP mode (particularly in monochromatic devices) is the most difficult to address because of its short lifetime and near-field nature, and conventional approaches like forming photonic arrays through photolithography are not fully compatible with soft perovskite materials. Therefore, novel light out-coupling strategies need to be developed for PeLEDs, particularly for the waveguide and SPP modes.

(iv) The degradation mechanism and lifetime of PeLEDs. The short device lifetimes of PeLEDs at this stage dramatically reduces their practicality, and must be tackled before their future commercialisation. The complications in stability can be broken down into photons (associated with light-soaking stability), phonons (associated with heating stability) and electrons (associated with electric-field stability), and as such, there are many possible avenues open to the degradation of PeLEDs. Unveiling these degradation processes in different perovskite emitters and device architectures is tantamount to the success of PeLEDs. At this stage, it is well accepted that ion migration in perovskites (especially under light soaking and electrical stress) is one of the main issues causing device degradation [418, 419]. The ionic nature of perovskites distinguishes them from other emitters like organic materials and inorganic III–V materials, but serves as a double-edged sword. On the one hand, it enables the solution processability of MHPs and allows their rapid crystallisation even at room temperature due to the low formation energy [420]. On the other hand, the ionic MHPs are very susceptible to external physical or chemical disturbances such as heat, moisture, oxygen, electrical fields and UV light [421]. It is generally accepted that the grain-boundaries serve as the main channel for ion migration, and can exacerbate the process through the accumulation of defects and degraded interfaces [422]. Ion migration is a dynamic and complicated process entailing the formation of different defects, interfacial charge and ion accumulation, degradation of interlayers, and corrosion of electrodes [423]. With these insights in mind, more systematic studies should be pursued to fully grasp the fundamental ionic nature of MHPs and address the ion migration issue.

Although many obstacles remain in the PeLED field at this stage, we still believe this technology has great potential for next-generation lighting. We hope this review will help scien-

tists to better understand and approach these challenges in the near future.

Acknowledgments

This study was financially supported by the Guangdong Major Project of Basic and Applied Basic Research (No. 2019B030302007), the National Natural Science Foundation of China (Nos. 51903086 and 62075065) and the China Postdoctoral Science Foundation (Nos. 2019M650197 and 2020T130204), and the European Research Council (ERC) under the European Union's Horizon 2020 research and innovation programme (Grant Agreement No. 639750). TRH is an EPSRC Doctoral Prize Fellow. AAB is a Royal Society University Research Fellow.

Data availability statement

No new data were created or analysed in this study.

ORCID iDs

Ziming Chen  <https://orcid.org/0000-0001-5008-3498>
 Thomas R Hopper  <https://orcid.org/0000-0001-5084-1914>
 Artem A Bakulin  <https://orcid.org/0000-0002-3998-2000>
 Hin-Lap Yip  <https://orcid.org/0000-0002-5750-9751>

References

- [1] Rose G 1840 *J. Prakt. Chem.* **19** 459–68
- [2] Breternitz J and Schorr S 2018 *Adv. Energy Mater.* **8** 1802366
- [3] Akkerman Q A and Manna L 2020 *ACS Energy Lett.* **5** 604–10
- [4] Goldschmidt V M 1926 *Naturwissenschaften* **14** 477–85
- [5] Mitchell R H, Welch M D and Chakhmouradian A R 2017 *Mineral. Mag.* **81** 411–61
- [6] Kim K and Siegel D J 2019 *J. Mater. Chem. A* **7** 3216–27
- [7] Mitzi D B 2001 *J. Chem. Soc., Dalton Trans.* **1** 1–12
- [8] Correa-Baena J P, Saliba M, Buonassisi T, Grätzel M, Abate A, Tress W and Hagfeldt A 2017 *Science* **358** 739–44
- [9] Glazer A M 1972 *Acta Crystallogr. B* **28** 3384–92
- [10] Shannon R D 1976 *Acta Crystallogr. A* **32** 751–67
- [11] Kieslich G, Sun S and Cheetham A K 2014 *Chem. Sci.* **5** 4712–5
- [12] Li C, Soh K C K and Wu P 2004 *J. Alloys Compd.* **372** 40–8
- [13] Li C, Lu X, Ding W, Feng L, Gao Y and Guo Z 2008 *Acta Crystallogr. B* **64** 702–7
- [14] Sun Q and Yin W J 2017 *J. Am. Chem. Soc.* **139** 14905–8
- [15] Bartel C J, Sutton C, Goldsmith B R, Ouyang R, Musgrave C B, Ghiringhelli L M and Scheffler M 2019 *Sci. Adv.* **5** eaav0693
- [16] Saidaminov M I, Mohammed O F and Bakr O M 2017 *ACS Energy Lett.* **2** 889–96
- [17] Zhu T, Khalsa G, Havas D M, Gibbs A S, Zhang W, Halasyamani P S, Benedek N A and Hayward M A 2018 *Chem. Mater.* **30** 8915–24
- [18] Cheng L, Jiang T, Cao Y, Yi C, Wang N, Huang W and Wang J 2019 *Adv. Mater.* **32** 1904163
- [19] Stoumpos C C, Cao D H, Clark D J, Young J, Rondinelli J M, Jang J I, Hupp J T and Kanatzidis M G 2016 *Chem. Mater.* **28** 2852–67
- [20] Ahmad S, Fu P, Yu S, Yang Q, Liu X, Wang X, Wang X, Guo X and Li C 2019 *Joule* **3** 794–806
- [21] Saparov B and Mitzi D B 2016 *Chem. Rev.* **116** 4558–96

- [22] Mao L, Stoumpos C C and Kanatzidis M G 2019 *J. Am. Chem. Soc.* **141** 1171–90
- [23] Ruddlesden S N and Popper P 1957 *Acta Crystallogr.* **10** 538–9
- [24] Ruddlesden S N and Popper P 1958 *Acta Crystallogr.* **11** 54–5
- [25] Beznosikov B V and Aleksandrov K S 2000 *Crystallogr. Rep.* **45** 792–8
- [26] Mao L, Ke W, Pedesseau L, Wu Y, Katan C, Even J, Wasielewski M R, Stoumpos C C and Kanatzidis M G 2018 *J. Am. Chem. Soc.* **140** 3775–83
- [27] Mao L, Guo P, Kepenekian M, Hadar I, Katan C, Even J, Schaller R D, Stoumpos C C and Kanatzidis M G 2018 *J. Am. Chem. Soc.* **140** 13078–88
- [28] Smith M D, Watson B L, Dauskardt R H and Karunadasa H I 2017 *Chem. Mater.* **29** 7083–7
- [29] Takano Y, Takayanagi S, Ogawa S, Yamada T and Mori N 1997 *Solid State Commun.* **103** 215–7
- [30] Aurivillius B 1949 *Ark. Kemi* **1** 463–80
- [31] Soe C M M et al 2017 *J. Am. Chem. Soc.* **139** 16297–309
- [32] Nazarenko O, Kotyrba M R, Wołrle M, Cuervo-Reyes E, Yakunin S and Kovalenko M V 2017 *Inorg. Chem.* **56** 11552–64
- [33] Xiao Z, Kerner R A, Zhao L, Tran N L, Lee K M, Koh T W, Scholes G D and Rand B P 2017 *Nat. Photon.* **11** 108–15
- [34] Quintero-Bermudez R, Gold-Parker A, Proppe A H, Munir R, Yang Z, Kelley S O, Amassian A, Toney M F and Sargent E H 2018 *Nat. Mater.* **17** 900–7
- [35] Chen A Z, Shiu M, Ma J H, Alpert M R, Zhang D, Foley B J, Smilgies D M, Lee S H and Choi J J 2018 *Nat. Commun.* **9** 1336
- [36] Gao L, Zhang F, Xiao C, Chen X, Larson B W, Berry J J and Zhu K 2019 *Adv. Funct. Mater.* **29** 1901652
- [37] Lei L et al 2020 *Adv. Mater.* **32** 1906571
- [38] Chen Z, Liu M, Li Z, Shi T, Yang Y, Yip H-L and Cao Y 2018 *iScience* **9** 337–46
- [39] Wang J et al 2020 *Nat. Commun.* **11** 582
- [40] Cho H et al 2015 *Science* **350** 1222
- [41] Park M H et al 2017 *Nano Energy* **42** 157–65
- [42] Lee H D et al 2019 *Adv. Funct. Mater.* **29** 1901225
- [43] Zhou M, Fei C, Sarmiento J S and Wang H 2019 *Sol. RRL* **3** 1800359
- [44] Tsai H et al 2016 *Nature* **536** 312–6
- [45] Zhang X et al 2018 *Adv. Mater.* **30** 1707166
- [46] Liu N et al 2020 *ACS Appl. Mater. Interfaces* **12** 3127–33
- [47] Ling Y, Yuan Z, Tian Y, Wang X, Wang J C, Xin Y, Hanson K, Ma B and Gao H 2016 *Adv. Mater.* **28** 305–11
- [48] Tyagi P, Arveson S M and Tisdale W A 2015 *J. Phys. Chem. Lett.* **6** 1911–6
- [49] Sichert J A et al 2015 *Nano Lett.* **15** 6521–7
- [50] Akkerman Q A et al 2016 *J. Am. Chem. Soc.* **138** 1010–6
- [51] Wu Y et al 2018 *ACS Energy Lett.* **3** 2030–7
- [52] Zhang C, Wan Q, Wang B, Zheng W, Liu M, Zhang Q, Kong L and Li L 2019 *J. Phys. Chem. C* **123** 26161–9
- [53] Peng S et al 2020 *ACS Appl. Mater. Interfaces* **12** 31863–74
- [54] Peng S et al 2020 *Angew. Chem., Int. Ed.* **59** 22156–62
- [55] Murray C B, Norris D J and Bawendi M G 1993 *J. Am. Chem. Soc.* **115** 8706–15
- [56] Ekimov A I and Efros Al LOnushchenko A A 1985 *Solid State Commun.* **56** 921
- [57] Brus L E 1983 *J. Chem. Phys.* **79** 5566–71
- [58] Brus L E 1986 *J. Chem. Phys.* **90** 2555–60
- [59] Brus L E 1984 *J. Chem. Phys.* **80** 4403–9
- [60] Weidman M C, Goodman A J and Tisdale W A 2017 *Chem. Mater.* **29** 5019–30
- [61] Bekenstein Y, Koscher B A, Eaton S W, Yang P and Alivisatos A P 2015 *J. Am. Chem. Soc.* **137** 16008–11
- [62] Schmidt L C, Pertegas A, Gonzalez-Carrero S, Malinkiewicz O, Agouram S, Espallargas G M, Bolink H J, Galian R E and Perez-Prieto J 2014 *J. Am. Chem. Soc.* **136** 850–3
- [63] Li X, Wu Y, Zhang S, Cai B, Gu Y, Song J and Zeng H 2016 *Adv. Funct. Mater.* **26** 2435–45
- [64] Zhu H et al 2015 *Nat. Mater.* **14** 636–42
- [65] Wong A B, Lai M, Eaton S W, Yu Y, Lin E, Dou L, Fu A and Yang P 2015 *Nano Lett.* **15** 5519–24
- [66] Xing J, Liu X F, Zhang Q, Ha S T, Yuan Y W, Shen C, Sun T C and Xiong Q 2015 *Nano Lett.* **15** 4571–7
- [67] Protesescu L, Yakunin S, Bodnarchuk M I, Krieg F, Caputo R, Hendon C H, Yang R X, Walsh A and Kovalenko M V 2015 *Nano Lett.* **15** 3692–6
- [68] Pan Q et al 2017 *J. Mater. Chem. C* **5** 10947–54
- [69] Tong Y et al 2016 *Angew. Chem., Int. Ed.* **55** 13887–92
- [70] Zhu Z Y, Yang Q Q, Gao L F, Zhang L, Shi A Y, Sun C L, Wang Q and Zhang H L 2017 *J. Phys. Chem. Lett.* **8** 1610–4
- [71] Waleed A, Tavakoli M M, Gu L, Hussain S, Zhang D, Poddar S, Wang Z, Zhang R and Fan Z 2017 *Nano Lett.* **17** 4951–7
- [72] Chen M et al 2017 *Adv. Funct. Mater.* **27** 1701121
- [73] Almeida G, Infante I and Manna L 2019 *Science* **364** 833–4
- [74] Dutta A, Behera R K, Pal P, Baitalik S and Pradhan N 2019 *Angew. Chem., Int. Ed.* **131** 5608–12
- [75] Yang D, Li X and Zeng H 2018 *Adv. Mater. Interfaces* **5** 1701662
- [76] Uratani H and Yamashita K 2017 *J. Phys. Chem. Lett.* **8** 742–6
- [77] Li J et al 2017 *Adv. Mater.* **29** 1603885
- [78] Krieg F et al 2018 *ACS Energy Lett.* **3** 641–6
- [79] Ai B, Liu C, Wang J, Xie J, Han J and Zhao X 2016 *J. Am. Ceram. Soc.* **99** 2875–7
- [80] Jang J et al 2020 *Adv. Mater.* **33** 2005255
- [81] Gu L et al 2016 *Adv. Mater.* **28** 9713–21
- [82] Deng H et al 2015 *Nanoscale* **7** 4163
- [83] Zhang D, Eaton S W, Yu Y, Dou L and Yang P 2015 *J. Am. Chem. Soc.* **137** 9230–3
- [84] Bi C, Hu J, Yao Z, Lu Y, Binks D, Sui M and Tian J 2020 *Adv. Funct. Mater.* **30** 2005990
- [85] Walsh A 2015 *J. Phys. Chem. C* **119** 5575–760
- [86] Umari P, Mosconi E and De Angelis F 2014 *Sci. Rep.* **4** 4467
- [87] Tao S, Schmidt I, Brocks G, Jiang J, Tranca I, Meerholz K and Olthof S 2019 *Nat. Commun.* **10** 2560
- [88] Li W, Wang Z, Deschler F, Gao S, Friend R H and Cheetham A K 2017 *Nat. Rev. Mater.* **2** 16099
- [89] Liu G et al 2018 *Proc. Natl Acad. Sci. USA* **115** 8076–81
- [90] Yin W J, Shi T and Yan Y 2014 *Adv. Mater.* **26** 4653–8
- [91] Tan Z K et al 2014 *Nat. Nanotechnol.* **9** 687–92
- [92] Kim Y H, Cho H, Heo J H, Kim T S, Myoung N, Lee C L, Im S H and Lee T W 2015 *Adv. Mater.* **27** 1248–54
- [93] Weidman M C, Seitz M, Stranks S D and Tisdale W A 2016 *ACS Nano* **10** 7830–9
- [94] Tan Y et al 2018 *ACS Appl. Mater. Interfaces* **10** 3784–92
- [95] Li G et al 2016 *Adv. Mater.* **28** 3528–34
- [96] Xing J et al 2016 *ACS Nano* **10** 6623–30
- [97] Jin X, Zhang X, Fang H, Deng W, Xu X, Jie J and Zhang X 2018 *Adv. Funct. Mater.* **28** 1705189
- [98] Levchuk I et al 2017 *Nano Lett.* **17** 2765–70
- [99] deQuilettes D W et al 2016 *Nat. Commun.* **7** 11683
- [100] Knight A J and Herz L M 2020 *Energy Environ. Sci.* **13** 2024–46
- [101] Saliba M et al 2016 *Science* **354** 206–9
- [102] Shi Y et al 2018 *ACS Appl. Mater. Interfaces* **10** 9849–57
- [103] Abdi-Jalebi M et al 2018 *Nature* **555** 497–501
- [104] Qiao L, Fang W H, Long R and Prezhdo O V 2020 *Angew. Chem., Int. Ed.* **59** 4684–90
- [105] Yang J N et al 2020 *J. Am. Chem. Soc.* **142** 2956–67
- [106] Yong Z J et al 2018 *J. Am. Chem. Soc.* **140** 9942–51
- [107] Saidaminov M I et al 2018 *Nat. Energy* **3** 648–54
- [108] Bi C, Wang S, Li Q, Kershaw S V, Tian J and Rogach A L 2019 *J. Phys. Chem. Lett.* **10** 943–52
- [109] Xiang W et al 2019 *Nat. Commun.* **10** 4686

- [110] Shen X *et al* 2019 *Nano Lett.* **19** 1552–59
- [111] Liu M, Zhong G, Yin Y, Miao J, Li K, Wang C, Xu X, Shen C and Meng H 2017 *Adv. Sci.* **4** 1700335
- [112] Yin J, Ahmed G H, Bakr O M, Bredas J L and Mohammed O F 2019 *ACS Energy Lett.* **4** 789–95
- [113] Zhang X *et al* 2019 *J. Phys. Chem. Lett.* **10** 1750–56
- [114] Pan G *et al* 2017 *Nano Lett.* **17** 8005–11
- [115] Hoffman J M *et al* 2019 *J. Am. Chem. Soc.* **141** 10661–76
- [116] Wygant B R, Ye A Z, Dolocan A, Vu Q, Abbot D M and Mullins C B 2019 *J. Am. Chem. Soc.* **141** 18170–81
- [117] Tsai H *et al* 2018 *Nat. Commun.* **9** 2130
- [118] Ashari-Astani N, Jahanbakhshi F, Mladenovic M, Alanazi A Q M, Ahmadabadi I, Ejtehadi M R, Dar M I, Grätzel M and Rothlisberger U 2019 *J. Phys. Chem. Lett.* **10** 3543–49
- [119] Zhou G, Xu Y and Xia Z 2020 *ACS Appl. Mater. Interfaces* **12** 27386–93
- [120] Yang X *et al* 2018 *Nat. Commun.* **9** 570
- [121] Ban M *et al* 2018 *Nat. Commun.* **9** 3892
- [122] He Z *et al* 2019 *ACS Photon.* **6** 587–94
- [123] Zhang S *et al* 2017 *Adv. Mater.* **29** 1606600
- [124] Chang J, Zhang S, Wang N, Sun Y, Wei Y, Li R, Yi C, Wang J and Huang W 2018 *J. Phys. Chem. Lett.* **9** 881–86
- [125] Shang Y, Liao Y, Wei Q, Wang Z, Xiang B, Ke Y, Liu W and Ning Z 2019 *Sci. Adv.* **5** eaaw8072
- [126] He T *et al* 2020 *Nat. Commun.* **11** 1672
- [127] Tanaka K, Sano F, Takahashi T, Kondo T, Ito R and Ema K 2002 *Solid State Commun.* **122** 249–52
- [128] Mitzi D B, Chondroudis K and Kagan C R 1999 *Inorg. Chem.* **38** 6246–56
- [129] Zhu X H, Mercier N, Frère P, Blanchard P, Roncali J, Allain M, Pasquier C and Riou A 2003 *Inorg. Chem.* **42** 5330–39
- [130] Yu M *et al* 2018 *Adv. Opt. Mater.* **7** 1801575
- [131] Gao Y *et al* 2019 *Nat. Chem.* **11** 1151–57
- [132] Kim Y H *et al* 2017 *ACS Nano* **11** 6586–93
- [133] Kumar S, Jagielski J, Marcato T, Solari S F and Shih C J 2019 *J. Phys. Chem. Lett.* **10** 7560–67
- [134] Li G, Huang J, Li Y, Tang J and Jiang Y 2019 *Nano Res.* **12** 109–14
- [135] Kim Y H, Lee G H, Kim Y T, Wolf C, Yun H J, Kwon W, Park C G and Lee T W 2017 *Nano Energy* **38** 51–58
- [136] Aharon S, Wierzbowska M and Etgar L 2018 *ACS Energy Lett.* **3** 1387–93
- [137] Motta C, El-Mellouhi F, Kais S, Tabet N, Alharbi F and Sanvitto S 2015 *Nat. Commun.* **6** 7026
- [138] Zheng F, Takenaka H, Wang F, Koocher N Z and Rappe A M 2015 *J. Phys. Chem. Lett.* **6** 31–37
- [139] Giorgi G, Fujisawa J, Segawa H and Yamashita K 2013 *J. Phys. Chem. Lett.* **4** 4213–16
- [140] Wolf S D, Holovsky J, Moon S, Löper P, Niesen B, Ledinsky M, Haug F, Yum J and Ballif C 2014 *J. Phys. Chem. Lett.* **5** 1035–39
- [141] Zheng F, Tan L Z, Liu S and Rappe A M 2015 *Nano Lett.* **15** 7794–7800
- [142] Kepenekian M, Robles R, Katan C, Sapori D, Pedesseau L and Even J 2015 *ACS Nano* **9** 11557–67
- [143] Isarov M, Tan L Z, Bodnarchuk M I, Kovalenko M V, Rappe A M and Lifshitz E 2017 *Nano Lett.* **17** 5020–26
- [144] Niesner D *et al* 2018 *Proc. Natl Acad. Sci. USA* **115** 9509–14
- [145] Niesner D, Wilhelm M, Levchuk I, Osvet A, Shrestha S, Batentschuk M, Brabec C and Fauster T 2016 *Phys. Rev. Lett.* **117** 126401
- [146] Hutter E M, Gélvez-Rueda M C, Osherov A, Bulović V, Grozema F C, Stranks S D and Savenije T J 2017 *Nat. Mater.* **16** 115–20
- [147] Wang T, Daiber B, Frost J M, Mann S A, Garnett E C, Walsh A and Ehrler B 2017 *Energy Environ. Sci.* **10** 509–15
- [148] Milot R L, Eperon G E, Snaith H J, Johnston M B and Herz L M 2015 *Adv. Funct. Mater.* **25** 6218–27
- [149] Davies C L *et al* 2018 *Nat. Commun.* **9** 293
- [150] Richter J M, Chen K, Sadhanala A, Butkus J, Rivett J P H, Friend R H, Monserrat B, Hodgkiss J M and Deschler F 2018 *Adv. Mater.* **30** 1803379
- [151] Zhai Y, Baniya S, Zhang C, Li J, Haney P, Sheng C, Ehrenfreund E and Vardeny Z V 2017 *Sci. Adv.* **3** e1700704
- [152] Becker M A *et al* 2018 *Nature* **553** 189–93
- [153] Tamarat P, Bodnarchuk M I, Trebbia J, Erni R, Kovalenko M V, Even J and Lounis B 2019 *Nat. Mater.* **18** 717–24
- [154] Utzat H *et al* 2019 *Science* **363** 1068–72
- [155] Steele J A *et al* 2019 *ACS Energy Lett.* **4** 2205–12
- [156] Younts R, Duan H S, Gautam B, Saparov B, Liu J, Mongin C, Castellano F N, Mitzi D B and Gundogdu K 2017 *Adv. Mater.* **29** 1604278
- [157] Qin C *et al* 2020 *Nat. Photon.* **14** 70–75
- [158] Era M, Maeda K and Tsutsui T 1998 *Chem. Phys. Lett.* **296** 417–20
- [159] Goto T, Makino H, Yao T, Chia C H, Makino T, Segawa Y, Mousdis G A and Papavassiliou G C 2006 *Phys. Rev. B* **73** 115206
- [160] Fujiwara K, Zhang S, Takahashi S, Ni L, Rao A and Yamashita K 2020 *ACS Photonics* **7** 845–52
- [161] Chen X, Lu H, Yang Y and Beard M C 2018 *J. Phys. Chem. Lett.* **9** 2595–603
- [162] Toyozawa Y 2003 *Optical Processes in Solids* (Cambridge: Cambridge University Press) pp 113–48 <https://doi.org/10.1017/CBO9780511615085>
- [163] Adjokatse S, Fang H H and Loi M A 2017 *Mater. Today* **20** 413–24
- [164] Herz L M 2016 *Annu. Rev. Phys. Chem.* **67** 65–89
- [165] D’Innocenzo V, Grancini G, Alcocer M J P, Kandada A R S, Stranks S D, Lee M M, Lanzani G, Snaith H J and Petrozza A 2014 *Nat. Commun.* **5** 3586
- [166] Grancini G *et al* 2015 *Nat. Photon.* **9** 695–701
- [167] Herz L M 2018 *J. Phys. Chem. Lett.* **9** 6853–63
- [168] Yamada Y, Nakamura T, Endo M, Wakamiya A and Kanemitsu Y 2014 *J. Am. Chem. Soc.* **136** 11610–13
- [169] Marongiu D, Saba M, Quochi F, Mura A and Bongiovanni G 2019 *J. Mater. Chem. C* **7** 12006–12018
- [170] Hong X, Ishihara T and Nurmiikko A V 1992 *Phys. Rev. B* **45** 6961–64
- [171] Fujita T, Sato Y, Kuitani T and Ishihara T 1998 *Phys. Rev. B* **57** 12428–34
- [172] Ishihara T, Takahashi J and Goto T 1989 *Solid State Commun.* **69** 933–36
- [173] Tanaka K, Takahashi T, Kondo T, Umeda K, Ema K, Umebayashi T, Asai K, Uchida K and Miura N 2005 *Japan. J. Appl. Phys.* **44** 5923–32
- [174] He X F 1991 *Phys. Rev. B* **43** 2063–69
- [175] Mathieu H, Lefebvre P and Christol P 1992 *Phys. Rev. B* **46** 4092–4101
- [176] Gangadharan D T and Ma D 2019 *Energy Environ. Sci.* **12** 2860–89
- [177] Mauck C M and Tisdale W A 2019 *Trends Chem.* **1** 380–93
- [178] Chernikov A, Berkelbach T C, Hill H M, Rigos A, Li Y, Aslan O B, Reichman D R, Hybertsen M S and Heinz T F 2014 *Phys. Rev. Lett.* **113** 076802
- [179] Achstein A W, Schliwa A, Prudnikau A, Hardzei M, Artemyev M V, Thomsen C and Woggon U 2012 *Nano Lett.* **12** 3151–57
- [180] Kataoka T, Kondo T, Ito R, Sasaki S, Uchida K and Miura N 1993 *Physica B* **184** 132–36
- [181] Straus D B and Kagan C R 2018 *J. Phys. Chem. Lett.* **9** 1434–47
- [182] Wright A D, Verdi C, Milot R L, Eperon G E, Pérez-Osorio M A, Snaith H J, Giustino F, Johnston M B and Herz L M 2016 *Nat. Commun.* **7** 11755

- [183] Kabakova I V, Azuri I, Chen Z, Nayak P K, Snaith H J, Kronik L, Paterson C, Bakulin A A and Egger D A 2018 *J. Mater. Chem. C* **6** 3861–68
- [184] Gold-Parker A, Gehring P M, Skelton J M, Smith I C, Parshall D, Frost J M, Karunadasa H I, Walsh A and Toney M F 2018 *Proc. Natl Acad. Sci. USA* **115** 11905–10
- [185] Fu M, Tamarat P, Trebbia J, Bodnarchuk M I, Kovalenko M V, Even J and Lounis B 2018 *Nat. Commun.* **9** 3318
- [186] Ni L, Huynh U, Cheminal A, Thomas T H, Shivanna R, Hinrichsen T F, Ahmad S, Sadhanala A and Rao A 2017 *ACS Nano* **11** 10834–43
- [187] Poncé S, Schlipf M and Giustino F 2019 *ACS Energy Lett.* **4** 456–63
- [188] Li M, Fu J, Xu Q and Sum T C 2019 *Adv. Mater.* **31** 1802486
- [189] Quarti C, Grancini G, Mosconi E, Bruno P, Ball J M, Lee M M, Snaith H J, Petrozza A and Angelis F D 2014 *J. Phys. Chem. Lett.* **5** 279–84
- [190] Sendner M *et al* 2016 *Mater. Horiz.* **3** 613–20
- [191] Yaffe O *et al* 2017 *Phys. Rev. Lett.* **118** 136001
- [192] Baikie T, Barrow N S, Fang Y, Keenan P J, Slater P R, Piltz R O, Gutmann M, Mhaisalkara S G and White T J 2015 *J. Mater. Chem. A* **3** 9298–9307
- [193] Wu X *et al* 2017 *Sci. Adv.* **3** e1602388
- [194] Gallop N P, Selig O, Giubertoni G, Bakker H J, Rezus Y L A, Frost J M, Jansen T L C, Lovrincic R and Bakulin A A 2018 *J. Phys. Chem. Lett.* **9** 5987–97
- [195] Grechko M, Bretschneider S A, Vietze L, Kim H and Bonn M 2018 *Angew. Chem., Int. Ed.* **57** 13657–61
- [196] Guo P *et al* 2019 *Nat. Commun.* **10** 482
- [197] Zhu H, Trinh M T, Wang J, Fu Y, Joshi P P, Miyata K, Jin S and Zhu X 2017 *Adv. Mater.* **29** 1603072
- [198] Frost J M 2017 *Phys. Rev. B* **96** 195202
- [199] Miyata K, Meggiolaro D, Trinh M T, Joshi P P, Mosconi E, Jones S C, Angelis F D and Zhu X 2017 *Sci. Adv.* **3** e1701217
- [200] Bischak C G, Hetherington C L, Wu H, Aloni S, Ogletree D F, Limmer D T and Ginsberg N S 2017 *Nano Lett.* **17** 1028–33
- [201] Munson K T, Kennehan E R, Doucette G S and Asbury J B 2018 *Chem* **4** 2826–43
- [202] Zhu X and Podzorov V 2015 *J. Phys. Chem. Lett.* **6** 4758–61
- [203] Zhu H, Miyata K, Fu Y, Wang J, Joshi P P, Niesner D, Williams K W, Jin S and Zhu X 2016 *Science* **353** 1409–13
- [204] Frost J M, Whalley L D and Walsh A 2017 *ACS Energy Lett.* **2** 2647–52
- [205] Hopper T R, Gorodetsky A, Frost J M, Müller C, Lovrincic R and Bakulin A A 2018 *ACS Energy Lett.* **3** 2199–2205
- [206] Förster T 1948 *Ann. Phys.* **437** 55–75
- [207] Penzo E *et al* 2020 *ACS Nano* **14** 6999–7007
- [208] Singldinger A, Gramlich M, Gruber C, Lampe C and Urban A S 2020 *ACS Energy Lett.* **5** 1380–85
- [209] Proppe A H *et al* 2019 *J. Phys. Chem. Lett.* **10** 419–26
- [210] Dexter D L 1953 *J. Chem. Phys.* **21** 836–50
- [211] Reineke S, Thomschke M, Lüssem B and Leo K 2013 *Rev. Mod. Phys.* **85** 1245–93
- [212] Ettenberg M and Kressel H 1976 *J. Appl. Phys.* **47** 1538–44
- [213] Wenger B, Nayak P K, Wen X, Kesava S V, Noel N K and Snaith H J 2017 *Nat. Commun.* **8** 590
- [214] Gan Z, Wen X, Chen W, Zhou C, Yang S, Cao G, Ghiggino K P, Zhang H and Jia B 2019 *Adv. Energy Mater.* **9** 1900185
- [215] Fang Y, Wei H, Dong Q and Huang J 2017 *Nat. Commun.* **8** 14417
- [216] Cho C, Zhao B, Tainter G D, Lee J-Y, Friend R H, Di D, Deschler F and Greenham N C 2020 *Nat. Commun.* **11** 611
- [217] Pazos-Outón L M *et al* 2016 *Science* **351** 1430–33
- [218] Crothers T W, Milot R L, Patel J B, Parrott E S, Schlipf J, Muller-Buschbaum P, Johnston M B and Herz L M 2017 *Nano Lett.* **17** 5782–89
- [219] Xing G, Mathews N, Sun S, Lim S S, Lam Y M, Grätzel M, Mhaisalkar S and Sum T C 2013 *Science* **342** 344–47
- [220] Stranks S D, Eperon G E, Grancini G, Menelaou C, Alcocer M J P, Leijtens T, Herz L M, Petrozza A and Snaith H J 2013 *Science* **342** 341–44
- [221] Dong Q, Fang Y, Shao Y, Mulligan P, Qiu J, Cao L and Huang J 2015 *Science* **347** 967–70
- [222] Herz L M 2017 *ACS Energy Lett.* **2** 1539–48
- [223] Tessler N, Preezant Y, Rappaport N and Roichman Y 2009 *Adv. Mater.* **21** 2741–61
- [224] Ginsberg N S and Tisdale W A 2020 *Annu. Rev. Phys. Chem.* **71** 1–30
- [225] Shi D *et al* 2015 *Science* **347** 519–22
- [226] Kagan C R, Mitzi D B and Dimitrakopoulos C D 1999 *Science* **286** 945–47
- [227] Wehrenfennig C, Eperon G E, Johnston M B, Snaith H J and Herz L M 2014 *Adv. Mater.* **26** 1584–89
- [228] Karakus M, Jensen S A, D’Angelo F, Turchinovich D, Bonn M and Canovas E 2015 *J. Phys. Chem. Lett.* **6** 4991–96
- [229] Stillman G E, Wolfe C M and Dimmock J O 1970 *J. Phys. Chem. Solids* **31** 1199–1204
- [230] Savenije T J *et al* 2014 *J. Phys. Chem. Lett.* **5** 2189–94
- [231] Zibouche N and Islam M S 2020 *ACS Appl. Mater. Interfaces* **12** 15328–37
- [232] Mizusaki J, Arai K and Fueki K 1983 *Solid State Ionics* **11** 203–11
- [233] Eames C, Frost J M, Barnes P R F, O’Regan B C, Walsh A and Islam M S 2015 *Nat. Commun.* **6** 7497
- [234] Shao Y *et al* 2016 *Energy Environ. Sci.* **9** 1752–59
- [235] Yang T-Y, Gregori G, Pellet N, Grätzel M and Maier J 2015 *Angew. Chem., Int. Ed.* **54** 7905–10
- [236] Senocrate A, Moudrakovski I, Kim G Y, Yang T-Y, Gregori G, Grätzel M and Maier J 2017 *Angew. Chem., Int. Ed.* **56** 7755–59
- [237] Kim G Y, Senocrate A, Yang T-Y, Gregori G, Grätzel M and Maier J 2018 *Nat. Mater.* **17** 445–49
- [238] Kim H-S, Jang I-H, Ahn N, Choi M, Guerrero A, Bisquert J and Park N-G 2015 *J. Phys. Chem. Lett.* **6** 4633–39
- [239] Meloni S *et al* 2016 *Nat. Commun.* **7** 10334
- [240] Li C, Tscheuschner S, Paulus F, Hopkinson P E, Kießling J, Köhler A, Vaynzof Y and Huettner S 2016 *Adv. Mater.* **28** 2446–54
- [241] Knight A J, Patel J B, Snaith H J, Johnston M B and Herz L M 2020 *Adv. Energy Mater.* **10** 1903488
- [242] Richter J M *et al* 2016 *Nat. Commun.* **7** 13941
- [243] Sum T C, Mathews N, Xing G, Lim S S, Chong W K, Giovanni D and Dewi H A 2016 *Acc. Chem. Res.* **49** 294–302
- [244] Johnson S R, Ding D, Wang J, Yu S and Zhang Y 2007 *J. Vac. Sci. Technol. B* **25** 1077–82
- [245] Cohn A W, Kittilstved K R and Gamelin D R 2012 *J. Am. Chem. Soc.* **134** 7937–43
- [246] Spanhel L and Anderson M A 1991 *J. Am. Chem. Soc.* **113** 2826–33
- [247] Park J S, Kim S, Xie Z and Walsh A 2018 *Nat. Rev. Mater.* **3** 194–210
- [248] Luo J *et al* 2018 *Nature* **563** 541–45
- [249] Dohner E R, Jaffe A, Bradshaw L R and Karunadasa H I 2014 *J. Am. Chem. Soc.* **136** 13154–57
- [250] Kahmann S, Tekelenburg E K, Duim H, Kamminga M E and Loi M A 2020 *Nat. Commun.* **11** 2344
- [251] Gan Z *et al* 2019 *Adv. Opt. Mater.* **7** 1900971
- [252] Tsai H, Liu C, Kinigstein E, Li M, Tretiak S, Cotlet M, Ma X, Zhang X and Nie W 2020 *Adv. Sci.* **7** 1903202
- [253] Choi J W, Woo H C, Huang X, Jung W-G, Kim B-J, Jeon S-W, Yim S-Y, Lee J-S and Lee C-L 2018 *Nanoscale* **10** 13356–67
- [254] Hou S, Gangishetty M K, Quan Q and Congreve D N 2018 *Joule* **2** 1–13
- [255] Kagan C R, Murray C B, Nirmal M and Bawendi M G 1996 *Phys. Rev. Lett.* **76** 1517–20

- [256] Shirasaki Y, Supran G J, Bawendi M G and Bulović V 2013 *Nat. Photon.* **7** 13–23
- [257] Kagan C R, Murray C B and Bawendi M G 1996 *Phys. Rev. B* **54** 8633–43
- [258] Kagan C R, Lifshitz E, Sargent E H and Talapin D V 2016 *Science* **353** aac5523
- [259] Klimov V I, Mikhailovsky A A, McBranch D W, Leatherdale C A and Bawendi M G 2000 *Science* **287** 1011–13
- [260] Mei J, Leung N L C, Kwok R T K, Lam J W Y and Tang B Z 2015 *Chem. Rev.* **115** 11718–940
- [261] Jagielski J et al 2017 *Sci. Adv.* **3** eaaoq0208
- [262] Chen Z et al 2018 *Adv. Mater.* **30** 1801370
- [263] Liang J, Zhang Y, Guo X, Gan Z, Lin J, Fana Y and Liu X 2016 *RSC Adv.* **6** 71070–75
- [264] Kojima A, Ikegami M, Teshima K and Miyasaka T 2012 *Chem. Lett.* **41** 397–99
- [265] Chu S, Chen W, Fang Z, Xiao X, Liu Y, Chen J, Huang J and Xiao Z 2021 *Nat. Commun.* **12** 147
- [266] Li D et al 2020 *Adv. Mater. Technol.* **5** 2000099
- [267] Fu Y, Zhang Q, Zhang D, Tang Y, Shu L, Zhu Y and Fan Z 2020 *Adv. Funct. Mater.* **30** 2002913
- [268] Xie S, Osherov A and Bulović V 2020 *APL Mater.* **8** 051113
- [269] Du P et al 2019 *ACS Appl. Mater. Interfaces* **11** 47083–90
- [270] Han B, Shan Q, Zhang F, Song J and Zeng H 2020 *J. Semicond.* **41** 052205
- [271] Stranks S D, Hoye R L Z, Di D, Friend R H and Deschler F 2018 *Adv. Mater.* **31** 1803336
- [272] Hong X, Ishihara T and Nurmikko A V 1992 *Solid State Commun.* **84** 657–61
- [273] Era M, Morimoto S, Tsutsui T and Saito S 1994 *Appl. Phys. Lett.* **65** 676–78
- [274] Hattori T, Taira T, Era M, Tsutsui T and Saito S 1996 *Chem. Phys. Lett.* **254** 103–108
- [275] Cöllea M, Brutting W, Schwoerer M, Yahirō M and Tsutsui T 2001 Organic light-emitting materials and devices IV *Proc. SPIE* vol 4105 pp 328–37 <https://doi.org/10.1117/12.416912>
- [276] Matsushima T, Fujita K and Tsutsui T 2005 *Japan. J. Appl. Phys.* **44** 1457–61
- [277] Ishihara T, Hong X, Ding J and Nurmikko A V 1992 *Surf. Sci.* **267** 323–26
- [278] Chondroudis M and Mitzi D 1999 *Chem. Mater.* **11** 3028–30
- [279] Koutselas I, Bampoulis P, Maratou E, Evangelinou T, Pagona G and Papavassiliou G C 2011 *J. Phys. Chem. C* **115** 8475–83
- [280] Wang J et al 2015 *Adv. Mater.* **27** 2311–16
- [281] Song J, Li J, Li X, Xu L, Dong Y and Zeng H 2015 *Adv. Mater.* **27** 7162–67
- [282] Yuan M et al 2016 *Nat. Nanotechnol.* **11** 872–77
- [283] Wang N et al 2016 *Nat. Photon.* **10** 699–704
- [284] Qasim K et al 2017 *Adv. Funct. Mater.* **27** 1606874
- [285] Chen Z et al 2017 *Adv. Mater.* **29** 1603157
- [286] Zhang L et al 2017 *Nat. Commun.* **8** 15640
- [287] Lin K et al 2018 *Nature* **562** 245–48
- [288] Cao Y et al 2018 *Nature* **562** 249–53
- [289] Lu M et al 2018 *ACS Energy Lett.* **3** 1571–77
- [290] Chiba T, Hayashi Y, Ebe H, Hoshi K, Sato J, Sato S, Pu Y-J, Ohisa S and Kido J 2018 *Nat. Photon.* **12** 681–87
- [291] Kumawat N K, Dey A, Kumar A, Gopinathan S P, Narasimhan K L and Kabra D 2015 *ACS Appl. Mater. Interfaces* **7** 13119–24
- [292] Xing J et al 2018 *Nat. Commun.* **9** 3541
- [293] Mao J, Lin H, Ye F, Qin M, Burkhardtmeier J M, Zhang H, Lu X, Wong K S and Choy W C H 2018 *ACS Nano* **12** 10486–92
- [294] Li Z, Chen Z, Yang Y, Xue Q, Yip H-L and Cao Y 2019 *Nat. Commun.* **10** 1027
- [295] Wang Q et al 2019 *Nat. Commun.* **10** 5633
- [296] Xu W et al 2019 *Nat. Photon.* **13** 418–24
- [297] Dong Y et al 2020 *Nat. Nanotechnol.* **15** 668–74
- [298] Sun R et al 2020 *ACS Energy Lett.* **5** 2131–39
- [299] Chen J et al 2020 *Nat. Photon.* **15** 1–7
- [300] Kim Y-H et al 2021 *Nat. Photon.* **15** 148–55
- [301] Chen Z et al 2021 *Joule* **5** 456–66
- [302] Zhang X et al 2016 *J. Phys. Chem. Lett.* **7** 4602–10
- [303] Zou W et al 2018 *Nat. Commun.* **9** 608
- [304] Zhao B et al 2018 *Nat. Photon.* **12** 783–89
- [305] Zhao X and Tan Z-K 2020 *Nat. Photon.* **4** 215–18
- [306] Liu Y et al 2019 *Nat. Photon.* **13** 760–64
- [307] Chu Z et al 2020 *Nat. Commun.* **11** 4165
- [308] Brenner T M, Egger D A, Rappe A M, Kronik L, Hodes G and Cahen D 2015 *J. Phys. Chem. Lett.* **6** 4754–57
- [309] Sheng R, Ho-Baillie A, Huang S, Chen S, Wen X, Hao X and Green M A 2015 *J. Phys. Chem. C* **119** 3545–49
- [310] Rutledge S A and Helmy A S 2013 *J. Appl. Phys.* **114** 133708
- [311] Zhang X, Lin H, Huang H, Reckmeier C, Zhang Y, Choy W C H and Rogach A L 2016 *Nano Lett.* **16** 1415–20
- [312] Fakharuddin A et al 2019 *Adv. Funct. Mater.* **29** 1904101
- [313] Hoye R L Z et al 2015 *Adv. Mater.* **27** 1414–19
- [314] Pan J, Chen J, Huang Q, Khan Q, Liu X, Tao Z, Zhang Z, Lei W and Nathan A 2016 *ACS Photonics* **3** 215–22
- [315] Dai X, Zhang Z, Jin Y, Niu Y, Cao H, Liang X, Chen L, Wang J and Peng X 2014 *Nature* **515** 96–99
- [316] Malinkiewicz O, Yella A, Lee Y H, Espallargas G M, Graetzel M, Nazeeruddin M K and Bolink H J 2014 *Nat. Photon.* **8** 128–32
- [317] Kim H, Lim K-G and Lee T-W 2016 *Energy Environ. Sci.* **9** 12–30
- [318] Abrusci A, Stranks S D, Docampo P, Yip H-L, Jen A K-Y and Snaith H J 2013 *Nano Lett.* **13** 3124–28
- [319] Hong W-L, Huang Y-C, Chang C-Y, Zhang Z-C, Tsai H-R, Chang N-Y and Chao Y-C 2016 *Adv. Mater.* **28** 8029–36
- [320] Redecker M, Bradley D D C, Inbasekaran M and Woo E P 1998 *Appl. Phys. Lett.* **73** 1565–67
- [321] Perumal A et al 2014 *Adv. Mater.* **27** 93–100
- [322] Ling Y et al 2016 *Adv. Mater.* **28** 8983–89
- [323] Hu Z, Chen D, Yang P, Yang L, Qin L, Huang Y and Zhao X 2018 *Appl. Surf. Sci.* **441** 258–64
- [324] Arora N, Dar M I, Hinderhofer A, Pellet N, Schreiber F, Zakeeruddin S M and Grätzel M 2017 *Science* **358** 768–71
- [325] Wang R et al 2020 *J. Lumin.* **219** 116915
- [326] Yokoyama D, Sasabe H, Furukawa Y, Adachi C and Kido J 2011 *Adv. Funct. Mater.* **21** 1375–82
- [327] Mai C et al 2020 *Adv. Opt. Mater.* **8** 1902177
- [328] Guan Z et al 2020 *ACS Appl. Mater. Interfaces* **12** 9440–47
- [329] Ren Z, Xiao X, Ma R, Lin H, Wang K, Sun X W and Choy W C H 2019 *Adv. Funct. Mater.* **29** 1905339
- [330] Chen W et al 2018 *Adv. Energy Mater.* **8** 1703519
- [331] Jiang Y, Jiang L, Yeung F S Y, Xu P, Chen S, Kwok H-S and Li G 2019 *ACS Appl. Mater. Interfaces* **11** 11119–24
- [332] Sun Y, Jiang Y, Peng H, Wei J, Zhang S and Chen S 2017 *Nanoscale* **9** 8962–69
- [333] Peng X-F, Wu X-Y, Ji X-X, Ren J, Wang Q, Li G-Q and Yang X-H 2017 *J. Phys. Chem. Lett.* **8** 4691–97
- [334] Kim Y-H, Wolf C, Cho H, Jeong S-H and Lee T-W 2016 *Adv. Mater.* **28** 734–41
- [335] Kim D B et al 2016 *J. Mater. Chem. C* **4** 8161–65
- [336] Wang Q, Chueh C-C, Zhao T, Cheng J, Eslamian M, Choy W C H and Jen A K Y 2017 *ChemSusChem* **10** 3794–803
- [337] Lin J et al 2019 *Adv. Funct. Mater.* **30** 1907265
- [338] Liu M, Chen Z, Chen Z, Yip H-L and Cao Y 2019 *Mater. Chem. Front.* **3** 496–504
- [339] Yuan S, Liu Q-W, Tian Q-S, Jin Y, Wang Z-K and Liao L-S 2020 *Adv. Funct. Mater.* **30** 1909222
- [340] Meng L, Yao E P, Hong Z, Chen H, Sun P, Yang Z, Li G and Yang Y 2017 *Adv. Mater.* **29** 1603826

- [341] Yang Y, Zheng Y, Cao W, Titov A, Hyvonen J, Manders J R, Xue J, Holloway P H and Qian L 2015 *Nat. Photon.* **9** 259–66
- [342] Qian L, Zheng Y, Xue J and Holloway P H 2011 *Nat. Photon.* **5** 543–48
- [343] Meng F, Zhang C, Chen D, Zhu W, Yip H-L and Su S-J 2017 *J. Mater. Chem. C* **5** 6169–75
- [344] Cao F, Wang H, Shen P, Li X, Zheng Y, Shang Y, Zhang J, Ning Z and Yang X 2017 *Adv. Funct. Mater.* **27** 1704278
- [345] Lu J *et al* 2020 *Adv. Sci.* **7** 2000069
- [346] Lin X, Wu X, Zheng J, Rui H, Zhang Z, Hua Y and Yin S 2019 *IEEE Electron Device Lett.* **40** 1479–82
- [347] Liu M, Luan W, Huang Y and Zhang S 2020 *IOP Conf. Ser.: Mater. Sci. Eng.* **729** 012098
- [348] Liu B, Wang L, Gu H, Sun H and Demir H V 2018 *Adv. Opt. Mater.* **6** 1800220
- [349] Zhou B, Wang Z, Geng S, Li Y, Wang K, Cao K, Wen Y and Chen R 2020 *Phys. Status Solidi RRL* **14** 2000083
- [350] Malinsky J E *et al* 1999 *Adv. Mater.* **11** 227–31
- [351] Ho P K H, Kim J-S, Burroughes J H, Becker H, Li S F Y, Brown T M, Cacialli F and Friend R H 2000 *Nature* **404** 481–84
- [352] Lee B R *et al* 2018 *ACS Nano* **12** 5826–33
- [353] Li Z, Cao K, Li J, Du X, Tang Y and Yu B 2020 *Org. Electron.* **81** 105675
- [354] Shi Y *et al* 2018 *Adv. Mater.* **30** 1800251
- [355] He M *et al* 2017 *Nat. Commun.* **8** 16045
- [356] Williams S T, Chueh C-C and Jen A K-Y 2015 *Small* **11** 3088–96
- [357] Moore D T, Sai H, Tan K W, Smilgies D M, Zhang W, Snaith H J, Wiesner U and Estroff L A 2015 *J. Am. Chem. Soc.* **137** 2350–58
- [358] Zhang W *et al* 2015 *Nat. Commun.* **6** 6142
- [359] Yu F-X, Zhang Y, Xiong Z-Y, Ma X-J, Chen P, Xiong Z-H and Gao C-H 2017 *Org. Electron.* **50** 480–84
- [360] Cai W, Chen Z, Chen D, Su S, Xu Q, Yip H-L and Cao Y 2019 *RSC Adv.* **9** 27684–91
- [361] Lin H, Zhu L, Huang H, Reckmeier C J, Liang C, Rogachb A L and Choy W C H 2016 *Nanoscale* **8** 19846–52
- [362] Giuri A *et al* 2018 *Sci. Rep.* **8** 15496
- [363] Yu J C, Kim D W, Kim D B, Jung E D, Lee K-S, Lee S, Nuzzo D D, Kim J-S and Song M H 2017 *Nanoscale* **9** 2088–94
- [364] Zeng F *et al* 2020 *J. Lumin.* **223** 117178
- [365] Liu M, Chen Z, Xue Q, Cheung S H, So S K, Yip H-L and Cao Y 2018 *J. Mater. Chem. A* **6** 16347–54
- [366] Xie F X, Zhang D, Su H, Ren X, Wong K S, Gratzel M and Choy W C H 2015 *ACS Nano* **9** 639–46
- [367] Wang H *et al* 2020 *Nat. Commun.* **11** 891
- [368] Wojciechowski K *et al* 2014 *ACS Nano* **8** 12701–09
- [369] Wang T, Ding D, Zheng H, Wang X, Wang J, Liu H and Shen W 2019 *Sol. RRL* **3** 1900045
- [370] Liu Z, Chang J, Lin Z, Zhou L, Yang Z, Chen D, Zhang C, Liu S and Hao Y 2018 *Adv. Energy Mater.* **8** 1703432
- [371] Xing G *et al* 2017 *Nat. Commun.* **8** 14558
- [372] Cai W *et al* 2018 *ACS Appl. Mater. Interfaces* **10** 42564–72
- [373] Li G, Tan Z-K, Di D, Lai M L, Jiang L, Lim J H-W, Friend R H and Greenham N C 2015 *Nano Lett.* **15** 2640–44
- [374] Li J, Bade S G R, Shan X and Yu Z 2015 *Adv. Mater.* **27** 5196–5202
- [375] Jeong B *et al* 2018 *Adv. Funct. Mater.* **28** 1706401
- [376] Chen L-C, Tseng Z-L, Lin D-W, Lin Y-S and Chen S-H 2018 *Nanomaterials* **8** 459
- [377] Lee S *et al* 2018 *ACS Nano* **12** 3417–23
- [378] Wang Z, Cheng T, Wang F, Dai S and Tan Z 2016 *Small* **12** 4412–20
- [379] Liu Z, He F, Guan W, Tang W, Gu X, Qi Z and Hou L 2020 *J. Lumin.* **222** 117120
- [380] Yu J C, Kim D B, Jung E D, Lee B R and Song M H 2016 *Nanoscale* **8** 7036–42
- [381] Jiao B, Zhu X, Wu W, Dong H, Xia B, Xi J, Lei T, Hou X and Wu Z 2016 *Nanoscale* **8** 11084–90
- [382] Kim S J, Byun J, Jeon T, Jin H M, Hong H R and Kim S O 2018 *ACS Appl. Mater. Interfaces* **10** 2490–95
- [383] Zhu X *et al* 2018 *Energy Environ. Sci.* **11** 3349–57
- [384] Xing G, Mathews N, Lim S S, Yantara N, Liu X, Sabba D, Grätzel M, Mhaisalkar S and Sum T C 2014 *Nat. Mater.* **13** 476–80
- [385] Stranks S D, Burlakov V M, Leijtens T, Ball J M, Goriely A and Snaith H J 2014 *Phys. Rev. Appl.* **2** 034007
- [386] Samiee M *et al* 2014 *Appl. Phys. Lett.* **105** 153502
- [387] Yan F *et al* 2018 *Nano Lett.* **18** 3157–64
- [388] Chen P, Meng Y, Ahmadi M, Peng Q, Gao C, Xu L, Shao M, Xiong Z and Hu B 2018 *Nano Energy* **50** 615–22
- [389] Johnston M B and Herz L M 2016 *Acc. Chem. Res.* **49** 146–54
- [390] deQuilettes D W, Vorpahl S M, Stranks S D, Nagaoka H, Eperon G E, Ziffer M E, Snaith H J and Ginger D S 2015 *Science* **348** 683–86
- [391] Wu T *et al* 2020 *Angew. Chem., Int. Ed.* **132** 4128–34
- [392] Braly I L, deQuilettes D W, Pazos-Outón L M, Burke S, Ziffer M E, Ginger D S and Hillhouse H W 2018 *Nat. Photon.* **12** 355–61
- [393] Zhang X *et al* 2017 *Energy Environ. Sci.* **10** 2095–2102
- [394] Liu G, Liu Z, Zeng F, Wang X, Li S and Xie X 2020 *Chem. Phys. Lett.* **743** 137186
- [395] Koscher B A, Swabeck J K, Bronstein N D and Alivisatos A P 2017 *J. Am. Chem. Soc.* **139** 6566–69
- [396] Yao J *et al* 2018 *J. Am. Chem. Soc.* **140** 3626–34
- [397] Bohn B J *et al* 2018 *Nano Lett.* **18** 5231–38
- [398] Song J, Fang T, Li J, Xu L, Zhang F, Han B, Shan Q and Zeng H 2018 *Adv. Mater.* **30** 1805409
- [399] Jeon S, Zhao L, Jung Y-J, Kim J W, Kim S-Y, Kang H, Jeong J-H, Rand B P and Lee J-H 2019 *Small* **15** 1900135
- [400] Loper P *et al* 2015 *J. Phys. Chem. Lett.* **6** 66–71
- [401] Xie Z, Sun S, Yan Y, Zhang L, Hou R, Tian F and Qin G G 2017 *J. Phys.: Condens. Matter.* **29** 245702
- [402] Jung Y-J, Cho S-Y, Jung J-W, Kim S-Y and Lee J-H 2019 *Nano Converg.* **6** 26
- [403] Jiang Y, Green M A, Sheng R and Ho-Baillie A 2015 *Data in Brief* **3** 201–208
- [404] Shi X-B, Liu Y, Yuan Z, Liu X-K, Miao Y, Wang J, Lenk S, Reineke S and Gao F 2018 *Adv. Opt. Mater.* **6** 1800667
- [405] Park M-H *et al* 2019 *Adv. Funct. Mater.* **29** 1902017
- [406] Zhao L, Lee K M, Roh K, Khan S U Z and Rand B P 2019 *Adv. Mater.* **31** 1805836
- [407] Meng S-S, Lia Y-Q and Tang J-X 2018 *Org. Electron.* **61** 351–58
- [408] Kim J-B, Lee J-H, Moon C-K, Kim S-Y and Kim J-J 2013 *Adv. Mater.* **25** 3571–77
- [409] Flämmich M, Frischeisen J, Setz D S, Michaelis D, Krummacher B C, Schmidt T D, Brüting W and Danz N 2011 *Org. Electron.* **12** 1663–68
- [410] Kim K-H and Kim J-J 2018 *Adv. Mater.* **30** 1705600
- [411] Shen Y, Cheng L-P, Li Y-Q, Li W, Chen J-D, Lee S-T and Tang J-X 2019 *Adv. Mater.* **31** 1901517
- [412] Zhang Q *et al* 2019 *Nat. Commun.* **10** 727
- [413] Zhang Q, Zhang D, Gu L, Tsui K-H, Poddar S, Fu Y, Shu L and Fan Z 2020 *ACS Nano* **14** 1577–85
- [414] Zhang Y, Sun H, Zhang S, Lia S, Wang X, Zhang X, Liu T and Guo Z 2019 *Opt. Mater.* **89** 563–67
- [415] Xu T, Li W, Wu X, Ahmadi M, Xu L and Chen P 2020 *J. Mater. Chem. C* **8** 6615–22
- [416] Chen P, Xiong Z, Wu X, Shao M, Meng Y, Xiong Z-H and Gao C 2017 *J. Phys. Chem. Lett.* **8** 3961–69

- [417] Motti S G, Crothers T, Yang R, Cao Y, Li R, Johnston M B, Wang J and Herz L M 2019 *Nano Lett.* **19** 3953–60
- [418] Mao W, Hall C R, Bernardi S, Cheng Y B, Widmer-Cooper A, Smith T A and Bach U 2021 *Nat. Mater.* **20** 55–61
- [419] Xiao Z *et al* 2017 *Nano Lett.* **17** 6863–69
- [420] Liu D, Yang C, Bates M and Lunt R R 2018 *iScience* **31** 272–79
- [421] Cho H, Kim Y H, Wolf C, Lee H D and Lee T W 2018 *Adv. Mater.* **30** 1704587
- [422] Miao Y *et al* 2019 *Nat. Commun.* **10** 3624
- [423] Yuan Y and Huang J 2016 *Acc. Chem. Res.* **49** 286–93